

The Magnetic Fields of the Solar Interior

A Dissertation
Presented to the Faculty of the Graduate School
of
Yale University
in Candidacy for the Degree of
Doctor of Philosophy

by
Charles S. Baldner

Dissertation Director: Prof. Sarbani Basu

December 2011

UMI Number: 3496827

All rights reserved

INFORMATION TO ALL USERS

The quality of this reproduction is dependent upon the quality of the copy submitted.

In the unlikely event that the author did not send a complete manuscript and there are missing pages, these will be noted. Also, if material had to be removed, a note will indicate the deletion.



UMI 3496827

Copyright 2012 by ProQuest LLC.

All rights reserved. This edition of the work is protected against unauthorized copying under Title 17, United States Code.



ProQuest LLC
789 East Eisenhower Parkway
P.O. Box 1346
Ann Arbor, MI 48106-1346

Abstract

The Magnetic Fields of the Solar Interior

Charles S. Baldner

Yale University

2011

Measuring the internal magnetic fields of the Sun would provide important constraints on our understanding of the mechanisms that underly solar activity. In this work, we have used a full solar cycle's worth of high quality helioseismic data from the Michelson Doppler Imager (MDI) instrument onboard the SOHO spacecraft to explore changes in the interior thermal structure, using the techniques of both global and local helioseismology. We have also used these data to attempt to directly measure the magnetic fields in the convection zone.

We have found that the interior of the Sun changed slightly but significantly over the course of the last solar cycle. Analyzing the global mode frequencies measured during solar cycle 23, we find a change, which we interpret as a change in the sound speed, at the base of the convection zone. At $r = (0.712^{+0.0097}_{-0.0029})R_{\odot}$, the change in sound speed is a decrease of $\delta c^2/c^2 = (7.23 \pm 2.08) \times 10^{-5}$. Modeling the effects of magnetic fields on the helioseismic splitting coefficients, we find that a field of strength necessary to cause the thermal change we find is not detectable with our data. We find that the signal that is there can be explained by a shallow toroidal field with a weak poloidal component. This field is tightly correlated with surface activity. We find that the toroidal field peaks at $r_0 = 0.999R_{\odot}$ and $r = 0.996R_{\odot}$, with peak field strengths of 380 ± 30 G and 1.4 ± 0.2 kG for the shallower and deeper fields, respectively. The peak strength of the poloidal field is 124 ± 17 G.

We employ ring diagram analysis to explore these layers of the Sun in more detail. We confirm earlier results that helioseismic frequencies increase in active regions, where strong surface magnetic fields are present, and that acoustic power is suppressed. We find that the changes in frequency depend somewhat on the surface geometry of the magnetic fields. Finally, we find in a large sample of active regions that the thermal structure beneath sunspots is a two layer structure with slower sound speed in the shallower layers (above approximately $r = 0.98R_{\odot}$) and a faster sound speed between approximately $r = 0.975R_{\odot}$ and $r = 0.985R_{\odot}$.

Copyright © 2011 by Charles S. Baldner
All Rights Reserved

Acknowledgments

It is an altogether pleasant task to sit down and write this bit (written last, though it comes first) where I acknowledge all those individuals and organizations who have contributed to this work. I hope hereby to spread the blame around a bit. With that in mind, I express my heartfelt thanks:

To my advisor, Sarbani, for her patience and guidance (the latter I invariably regretted not asking for sooner, the former necessary for that reason), but mostly for her even temper — and her toaster.

To Rick Bogart, at Stanford, for all his help — without him, this thesis would be much easier to lift. To Tim Larson, at Stanford, for the laughs. To Jesper Schou, at Stanford, for being consistently crazier than I am, and for his help. To the whole MDI cum HMI team at Stanford, for two fantastic instruments with which to study the Sun, and for their help in using them.

To Professor H. M. Antia, at the Tata Institute for Fundamental Research, for his guidance and for his awe-inspiring ability to pick up a page-long derivation he hasn't looked at in fifteen years and find my sign error immediately.

To the GONG team, for the instrument, and for being nice to me.

To NASA, for the financial support in the form of an Earth and Space Sciences Fellowship — I hope it was a worthwhile investment. Also, I'd like to acknowledge here their general support for science, without which we'd know a lot less about this universe of ours.

To Rob, for teaching me how to fly.

To my fellow graduate students (and the postdocs, too!). You know why, you beautiful bastards.

On a related note, to the wonderful breweries of the North-East, and New Haven's wonderful bars and restaurants. I'm pretty sure I owe you all thanks, but

I don't clearly remember why.

To my parents, whose fault, ultimately, all of this is.

To the rats.

And to my wife — no, to *Anne*.

Contents

| | | |
|----------|---|-----------|
| 1 | Introduction | 1 |
| 1.1 | The Solar Activity Cycle | 3 |
| 1.2 | The solar dynamo | 7 |
| 2 | Helioseismology | 9 |
| 2.1 | Helioseismic data | 9 |
| 2.2 | The forward and inverse problem | 12 |
| 2.2.1 | Oscillations in the Sun | 12 |
| 2.2.2 | The inverse problem | 25 |
| 2.3 | Results in helioseismology | 31 |
| 2.3.1 | Studying the interior | 32 |
| 2.3.2 | Local helioseismology | 33 |
| 2.3.3 | Solar activity and helioseismology | 35 |
| 2.3.4 | Magnetic Fields | 36 |
| 3 | Solar cycle related changes at the base of the convection zone | 39 |
| 3.1 | Introduction | 39 |
| 3.2 | Data & analysis | 42 |
| 3.2.1 | Data | 42 |
| 3.2.2 | Method | 43 |

| | | |
|----------|---|------------|
| 3.3 | Results & discussion | 46 |
| 3.3.1 | Mean frequencies | 46 |
| 3.3.2 | Latitudinal changes | 57 |
| 3.4 | Conclusions | 64 |
| 4 | Solar Magnetic Field Signatures in Helioseismic Splitting Coefficients | 65 |
| 4.1 | Introduction | 65 |
| 4.2 | Perturbations to solar oscillation frequencies | 67 |
| 4.3 | Data | 69 |
| 4.4 | Results | 72 |
| 4.4.1 | Models | 72 |
| 4.4.2 | Fits to observed data | 77 |
| 4.5 | Discussions and conclusions | 85 |
| 5 | A Statistical Study of Mode Parameters of Active Regions | 92 |
| 5.1 | Introduction | 92 |
| 5.2 | Analysis | 94 |
| 5.2.1 | The active region sample | 94 |
| 5.2.2 | The ring diagrams | 95 |
| 5.2.3 | The magnetic activity index | 96 |
| 5.3 | Results | 97 |
| 5.3.1 | Changes in frequency | 97 |
| 5.3.2 | Changes in other mode parameters | 104 |
| 5.4 | Discussion | 111 |
| 6 | The Structure of Active Regions | 115 |

| | | |
|----------|---|------------|
| 6.1 | Introduction | 115 |
| 6.2 | Ring diagram frequencies and errors | 116 |
| 6.3 | Inversions | 117 |
| 6.4 | Results | 120 |
| 6.5 | Discussion | 125 |
| 7 | Conclusions | 130 |
| A | Principal Component Analysis | 134 |
| B | | 138 |
| | Bibliography | 145 |

List of Figures

| | | |
|------|--|----|
| 1.1 | A modern butterfly diagram. | 4 |
| 1.2 | The line-of-sight magnetic field of the Sun. | 6 |
| 3.1 | The first four eigenvectors for the MDI data set. | 47 |
| 3.2 | The scaling coefficients for the first four eigenvectors. | 49 |
| 3.3 | Two reconstructed data sets compared to actual data. | 51 |
| 3.4 | The first two eigenvectors for the GONG data sets. | 53 |
| 3.5 | Inversion for sound speed of the $\vec{\xi}_1$ eigenvector. | 54 |
| 3.6 | Change in inferred sound speed as function of activity level. | 56 |
| 3.7 | The first eigenvector $\vec{\xi}_1(\theta)$ for latitudes from 0° to 75° | 58 |
| 3.8 | The scaling coefficients plotted as a function of time and latitude. | 59 |
| 3.9 | The inversions of the latitudinal frequencies. | 61 |
| 3.10 | The $\vec{\xi}_1$ eigenvectors for the asphericity terms | 62 |
| 3.11 | The scaling coefficients for the asphericity eigenvectors. | 63 |
| 4.1 | Splitting coefficients ℓa_2 due to poloidal magnetic fields. | 71 |
| 4.2 | Splitting coefficients ℓa_2 due to toroidal field with different latitudi- nal distributions. | 73 |
| 4.3 | Splitting coefficients ℓa_2 due to near-surface toroidal magnetic fields. | 75 |

| | | |
|------|--|-----|
| 4.4 | Same as Fig. 4.3, but plotted as a function of the lower turning radius r_t | 76 |
| 4.5 | Effects of toroidal magnetic fields at the base of the convection zone. | 77 |
| 4.6 | Effects of various magnetic fields on the ℓa_4 splitting coefficients | 78 |
| 4.7 | Fits to observed splitting coefficients ℓa_2 for different magnetic field configurations. | 81 |
| 4.8 | Comparisons of data to models for ℓa_4 splitting coefficients from two different data sets. | 82 |
| 4.9 | Fits to measured splitting coefficients ℓa_2 for six different sets throughout solar cycle 23 | 84 |
| 4.10 | The strength of the inferred magnetic fields as a function of time over solar cycle 23. | 86 |
| 4.11 | The strength of the inferred magnetic fields as a function of 10.7 cm radio flux. | 87 |
| 5.1 | Distribution of the active region sample in solar coordinates. | 95 |
| 5.2 | An example of the differences in ring diagram parameters between an active region and a quiet comparison region. | 98 |
| 5.3 | Averaged frequency differences in three different frequency bins | 99 |
| 5.4 | Slopes $a_{n,\ell}$ of individual mode frequency shifts with magnetic activity as a function of frequency. | 102 |
| 5.5 | Frequency differences for two different modes and frequency ranges split by phase of the solar cycle. | 103 |
| 5.6 | Frequency differences for two different modes and frequency ranges as a function of the growth parameter. | 104 |
| 5.7 | Averaged frequency differences separated by spot type. | 105 |

| | | |
|------|---|-----|
| 5.8 | Differences in mode frequency slopes between sunspot type. | 106 |
| 5.9 | Averaged differences of the logarithm of the amplitudes. | 107 |
| 5.10 | Averaged mode width differences. | 108 |
| 5.11 | Slopes of individual mode amplitudes and widths. | 109 |
| 5.12 | Relation between slopes of mode amplitudes and mode widths. . . . | 110 |
| 5.13 | Changes in power in each individual mode with increasing MAI, plotted as a function of frequency. | 111 |
| 5.14 | Averaged mode asymmetry differences. | 114 |
| 6.1 | A comparison of calculations in ring diagram frequencies | 118 |
| 6.2 | Examples of inversions for adiabatic sound speed squared c^2 for eight active regions. | 121 |
| 6.3 | Examples of inversions for adiabatic index Γ_1 for eight active regions. | 122 |
| 6.4 | Averages of inversions for c^2 over two depth ranges as a function of Δ MAI. | 123 |
| 6.5 | Position of transition between the negative and positive perturba- tions in the sound speed inversions | 124 |
| 6.6 | Averages of inversions for Γ_1 over two depth ranges as a function of Δ MAI. | 126 |
| 6.7 | Position of transition between the negative and positive perturba- tions in the Γ_1 inversions | 127 |

List of Tables

| | | |
|-----|--|-----|
| B.1 | The sample of active regions used in this work | 138 |
|-----|--|-----|

Chapter 1

Introduction

The Sun is the nearest star to our planet. This is obvious, but it is the reason that the Sun is such an interesting object to study. At such a close distance, the Sun can be studied in detail that no other astrophysical object can be. Thus, our understanding of stars, and more generally of the universe, is in many ways dependant on our understanding of the Sun. Furthermore, physical processes that would be extremely difficult or impossible to recreate in an Earth-bound laboratory can be studied in detail as they occur in or around the Sun. Finally, the Sun's proximity to the Earth, and its status as the primary source of energy for the climatic and ecological processes that take place here, make the Sun an object of practical importance for human life.

The object of this thesis is the study of one particular aspect of the solar constitution: the magnetic fields of the interior. We are interested here in furthering the understanding of what the structure of these magnetic fields is, how they are generated and evolve, and how they in turn influence the structure and evolution of the Sun. As our interest here is restricted to the interior, we make use of the techniques of helioseismology, by which we can make measurements of the interior

of the Sun which would otherwise be inaccessible to us. Magnetic fields at the surface of the Sun and the processes they drive, collectively referred to as ‘solar activity’, are more amenable to direct detection and study, and throughout this thesis we will attempt to relate what we can discover in the solar interior to solar activity at and above the surface.

This thesis addresses three general questions:

1. How does the internal structure of the Sun change over the course of a solar activity cycle?
2. What are the strengths and configurations of magnetic fields in the solar interior, and how do they change with respect to changes in surface activity?
3. How does local-scale activity, i.e. active regions, affect the structure of the Sun, and how are these phenomena connected to global changes in the Sun?

The remainder of this chapter gives an overview of solar activity and how it is thought to connect with global scale internal processes in the Sun. Chapter 2 discusses the field of helioseismology, outlining the physics that underpins the waves we measure, describing the interpretation of the waves, and finally reviewing the history of the field and its relevant results.

In the chapters that follow, we describe the work done in the course of this thesis. Chapter 3 describes the changes in structure in the solar interior over the course of a solar activity cycle. We find a small but significant variation in sound speed at the base of the convection zone, which has been previously suggested but never before detected with this level of confidence. In Chapter 4, we directly measure the strength and configuration of the internal magnetic fields, assuming our measured signal is entirely due to global, axisymmetric magnetic fields. We are unable to detect any magnetic fields at the base of the convection

zone, though the signal-to-noise in the data would not allow us to detect the strengths of fields we postulated in Chapter 3. We find instead that the helioseismic splitting coefficients can be explained by a global, axisymmetric toroidal field with a small poloidal component in the very near-surface layers of the Sun — the regime where individual active regions likely play an important role in affecting structure. Chapter 5 discusses the helioseismic properties of these active regions, and Chapter 6 discusses inferences about the thermal structure of the Sun beneath these regions. Chapter 7 summarizes our findings.

1.1 The Solar Activity Cycle

Solar activity is comprised of transient and local scale phenomena on the surface of the Sun and in the solar atmosphere. These phenomena include sunspots, plages, faculae, prominences, coronal loops, flares, coronal mass ejections (CMEs), and numerous other phenomena. A full discussion of solar activity is well beyond the scope of this introduction. We wish here only to summarize some of the most important features of solar activity and give a general review of some of the aspects most relevant to this work.

The most obvious and well known aspect of solar activity are sunspots. Sunspots are dark, compact areas of relatively cool plasma on the solar surface. Sunspots have been observed in the West since the time of Galileo, though there are suggestions that the ancient Greeks had seen sunspots as early as 400 BCE (Hoyt & Schatten 1997), and the Chinese and Koreans recorded sunspots from roughly 28 BCE onward, and possibly earlier (Clark & Stephenson 1978).

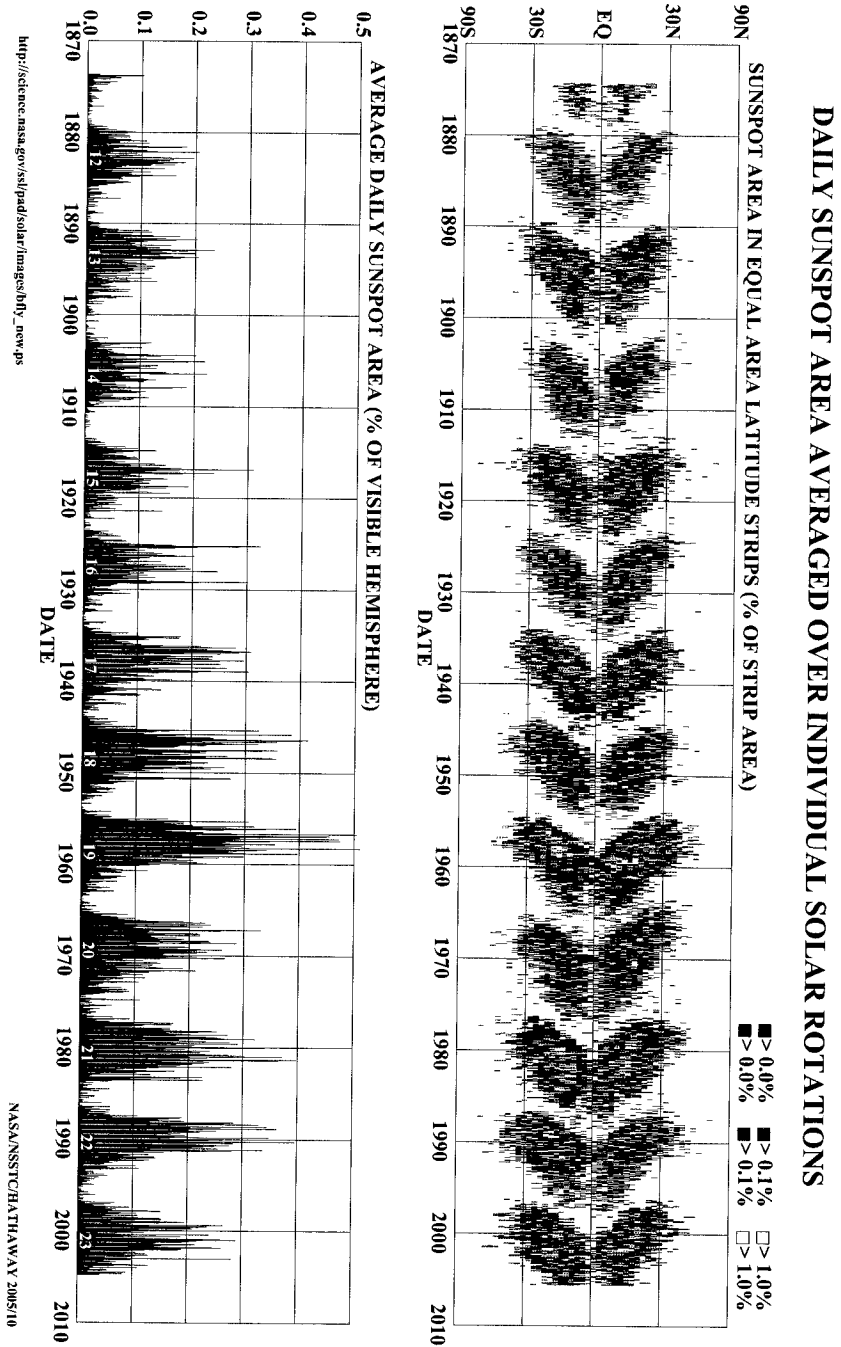


Fig. 1.1.— A modern butterfly diagram. The bottom panel shows the daily total sunspot coverage (as a fraction of the total visible disk). The top panel shows the sunspot coverage as a function of latitude. The migration of the active latitudes over the course of each solar cycle can clearly be seen. Figure courtesy of D. Hathaway, NASA/MSFC (http://solarscience.msfc.nasa.gov/images/bfly_new.ps).

In the 19th century, Heinrich Schwabe noted that the numbers of sunspots on the sun appeared to be periodic, with a periodicity of roughly 10 years (Schwabe 1844). It was Walter Maunder who first noted that not only is the total number of sunspots cyclic, but that their distribution in heliographic latitude also follows a pattern, with sunspots appearing at mid-latitudes early in a sunspot cycle, and migrating equatorward as the cycle progresses (Maunder 1904). Maunder's plot of sunspot latitudinal distribution as a function of time is today called a 'butterfly diagram', due to its characteristic shape. Figure 1.1 shows the butterfly diagram up to the present day. It is this cycle that we call the solar activity cycle.

Sunspots are fundamentally magnetic phenomena. The discovery that sunspots are strongly magnetic belongs to George Ellery Hale (Hale 1908). Using a (then novel) spectrograph, Hale was able to detect the Zeeman broadening of the $H\alpha$ line in all sunspots which he observed. Moreover, he found that sunspots have distinct magnetic polarities. In later work with collaborators, he noted that in bipolar spots, the polarity of all leading spots in the northern hemisphere is the same, and the opposite polarity leads in all southern hemisphere bipolar spots (Hale et al. 1919; Hale & Nicholson 1925). This is known as Hale's law. This ordering reverses itself every solar cycle. In the same work, it was noted that the preceding sunspot in all sunspot pairs is always closer to the solar equator. This is known as Joy's law.

With modern instrumentation, it is fairly easy to measure magnetic fields at the surface of the Sun, or at least their line-of-sight component, through their effect on certain spectral absorption lines. Sunspots are known to be only the areas of strongest magnetic field concentration in large complexes which we call active regions. For the purposes of this thesis, we can consider active regions to be the atomic building blocks of solar activity, as most of the important activity

phenomena are associated with active regions.

Figure 1.2 shows the solar activity cycle more directly than Figure 1.1, by showing the line-of-sight magnetic fields over the course of three activity cycles. The magnetic fields show the same spatial evolution as the sunspot butterfly diagram, and the same periodicity. The polarity of the polar magnetic field reverses itself every cycle, so the underlying magnetic cycle is twice as long as the sunspot cycle. The horizontal components of the magnetic field have also been shown over the course of several solar cycles (Ulrich & Boyden 2005).

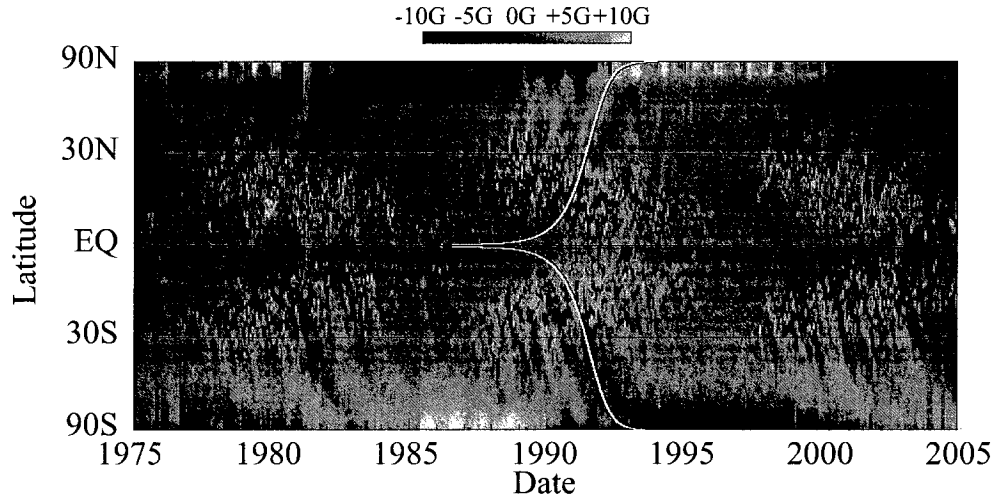


Fig. 1.2.— The line-of-sight magnetic field of the Sun, over three activity cycles. The data are taken from instruments on Kitt Peak and the SoHO spacecraft. Figure courtesy of D. Hathaway, NASA/MSFC (<http://solarscience.msfc.nasa.gov/images/magbfly.ps>)

1.2 The solar dynamo

Although individual active regions show a great deal of complex structure and heterogeneity, the organization of these regions on a global scale is strongly indicative of a global process generating and mediating these fields. This process is referred to as the solar dynamo, and understanding the operation of this dynamo is one of the most important outstanding questions in solar physics at the present time.

Any model of the solar dynamo must reproduce a number of observed properties of the Sun. First, it must be able to generate magnetic fields of strengths sufficient to generate active regions. It must reproduce the observed 11 year sunspot cycle and 22 year polarity reversal (the Hale cycle). It must reproduce the latitudinal evolution of surface magnetic fields — both the equatorward migration of active regions and the poleward migration of the polar field (see Figure 1.2. We mention here some of the features of current dynamo models, but for more detailed information, the reader should refer to reviews in the literature, e.g. Charbonneau (2010).

In most dynamo models, the solar magnetic field, or at least the large scale axisymmetric component, is separated into a toroidal and a poloidal component. The poloidal component dominates at the low phase of the activity cycle, and the toroidal component at the high phase of the activity cycle. Active region magnetic fields are surface manifestations of the toroidal field, though the details of how these fields rise and their dynamics once they emerge is another major open question in solar physics. The dynamo problem, then, is how to generate a toroidal field from a poloidal field, and then how to generate a poloidal field from that toroidal field.

The first of these two steps — poloidal to toroidal — is fairly easily explained. Differential rotation in the near-surface layers of the Sun can take a poloidal field

and shear it into a toroidal field. The reverse process is more difficult to explain. Some departure from axisymmetry is required; otherwise the toroidal field cannot be supported against resistive dissipation (Cowling 1933). Convective motions and turbulence can provide this, and are often included in dynamo models with the parameter α , and referred to as the α -effect.

A second problem is the strength of the observed fields in sunspots. Any fields of those strengths will be strongly buoyant, and storing them in the convection zone for time scales on the order of the activity cycle length is difficult to explain. In addition, the α -effect quenches when the magnetic energy density reaches equipartition with the convective energy density. One common solution to this problem is to store the fields below the convective envelope, in the shear layer called the tachocline (Parker 1993; Charbonneau & MacGregor 1996, etc., see also review by Dikpati 2006).

Although these so-called ‘interface dynamos’ have dominated the literature for much of the past two decades, fresh attention has been paid in recent years to the possibility of dynamo action that operates in the bulk of the convection zone or even almost entirely in the near-surface shear layer (see review by Brandenburg & Subramanian 2005). In these models, the strong velocity asymmetry in convection is invoked to counteract some of the adverse buoyancy, while action in the near-surface shear might serve to counteract α -quenching.

We will not discuss the relative merits of the various dynamo models here. Helioseismology can provide constraints on these models, however, by determining where changes in the solar structure are occurring over the course of the activity cycle, and where the magnetic fields are located. It is to contribute to those constraints that is one of the central aims of this thesis.

Chapter 2

Helioseismology

The Sun is observed to oscillate in millions of modes. These modes are standing waves of global or pseudo-global scale whose restoring force is pressure or gravity. The Sun is acting as a resonant cavity, and the properties of this cavity determine the properties of the resonant oscillations. Thus, the oscillations observed on the surface of the Sun can be used to probe the Sun's interior. This field is generally referred to as helioseismology ¹, and in this section we give a brief discussion of the basic ideas which underly the helioseismic techniques used in this thesis, and summarize some of the important results in the field.

2.1 Helioseismic data

Helioseismic observation involve time-resolved measurements of the solar surface or atmosphere. These measurements can be made either in intensity or in line-of-sight velocity, though it is the latter type of measurement that will be used

¹The term helioseismology obviously implies a debt to the much older field of terrestrial seismology. The idea of using waves observed at the surface to probe the interior is the core of the discipline of seismology. Chaplin (2006) gives credit for the name 'helioseismology' to Douglas Gough and Jørgen Christensen-Dalsgaard, though the first use of the term in the literature appears to have been Severnyi et al. (1979).

exclusively in this thesis.

Oscillatory motion in the Sun with periods of approximately five minutes were first detected by Leighton et al. (1962), and this detection was confirmed by Evans & Michard (1962). Ulrich (1970) and Leibacher & Stein (1971) suggested that these observations could be explained by standing acoustic waves trapped in the solar envelope. The observations of discrete power along ridges in $k - \nu$ space by Deubner (1975) confirmed this hypothesis. Rhodes et al. (1977), with somewhat better signal-to-noise, measured ridges of power in the solar power spectrum and argued convincingly that the power was due to trapped non-radial oscillations. The study of helioseismology was well and truly underway (though not yet so-named; see above).

Spurred by Deubner's observations, as well as subsequently discounted observations thought to be evidence of g -modes, the prospect of seismically probing the Sun was explored by a number of authors (Scuflaire et al. 1975; Christensen-Dalsgaard & Gough 1976; Iben & Mahaffy 1976). Conclusive demonstration of the existence of truly global modes was done by Claverie et al. (1979), whose integrated-light observations detected low-degree, global five-minute oscillations. Individual multiplets were resolved by observations made at the South Pole (Grec et al. 1980). The low-frequency observations of Claverie et al. (1979) and the higher frequency measurements of Deubner (1975) were argued to have common origin (Christensen-Dalsgaard & Gough 1982), and this was confirmed by Duvall & Harvey (1983), whose spatial and temporal power spectra — an early $\ell - \nu$ diagram — bridged the gap between the low and high frequency measurements.

Helioseismic observations benefit from long-term, high cadence and high duty cycle campaigns, due both to the nature of time series analysis and to the relatively low amplitude of solar acoustic oscillations. The diurnal rotation of the

Earth makes this challenging, however. The earliest solution to this problem was to observe from the South Pole during the austral summer (Grec et al. 1980; Duvall & Harvey 1984; Duvall et al. 1984, 1986). Longer term observations require either a ground-based network or an instrument in space. The Active Cavity Irradiance Monitor (ACRIM) on the Solar Maximum Mission (SMM) made the first space-based low-degree observations (Woodard & Noyes 1985). The network that would become the Birmingham Integrated Solar Network (BiSON Claverie et al. 1984; Elsworth et al. 1990) was the first ground-based helioseismic network experiment, and has now produced high quality low-degree observations of the Sun over three solar cycles. Important medium-degree measurements were made at the Big Bear Solar Observatory (BBSO Libbrecht & Woodard 1990). The integrated-light IRIS network operated from 1989 to 2003 and made low-degree measurements (Fossat 1995); medium-degree measurements were made by the LOWL-ECHO investigation (Tomczyk et al. 1993), and high degree measurements were made by the Taiwan Oscillations Network (TON Chou et al. 1995).

In 1995, a global network of six telescopes, the Global Oscillation Network Group (GONG) began taking data (Harvey et al. 1996). In December of that year, the Solar and Heliospheric Observatory (SoHO) was launched. On this satellite were three helioseismic instruments: the Global Oscillations at Low Frequencies instrument (GOLF Gabriel et al. 1995), the Luminosity Oscillations Imager (LOI Fröhlich et al. 1995), and the Michelson Doppler Imager (MDI Scherrer et al. 1995). The first two of these are low-degree instruments; MDI is a medium and high degree experiment. The GONG and MDI datasets form the backbone of this thesis.

2.2 The forward and inverse problem

2.2.1 Oscillations in the Sun

The Sun is a (nearly) spherical body, so it is convenient to describe pulsational modes in terms of spherical harmonics:

$$Y_\ell^m(\theta, \phi) = a_{\ell,m} P_\ell^m(\cos \theta) e^{im\phi}, \quad (2.1)$$

where P_ℓ^m is the associated Legendre polynomial, and $a_{\ell,m}$ is a normalization constant. Because spherical harmonics form an orthonormal set over the surface of a sphere, these functions are a natural choice of basis functions for observations of waves on a spherical surface, and it turns out that the normal modes of a nearly spherical star have angular dependencies given by the spherical harmonics. The Y_ℓ^m s are degenerate in m for a perfectly spherical star, but departures from spherical symmetry, induced by, among other things, rotation and magnetic fields, lift the degeneracy.

When the departures from spherical symmetry are small, as they are in the case of the Sun, the differences in frequency for different values of m will be small, and it is natural therefore to express the normal mode frequencies in terms of the mean frequency of the mode $\nu_{n\ell}$ and splitting coefficients a_j :

$$\nu_{n\ell m} = \nu_{n\ell} + \sum_{j=1}^{j_{\max}} a_j(n, \ell) \mathcal{P}_j^{(\ell)}(m). \quad (2.2)$$

As is common in the current literature, the polynomials $\mathcal{P}_j^{(\ell)}(m)$ are the Ritzwoller-Lavelly formulation of the Clebsch-Gordan expansion (Ritzwoller & Lavelly 1991). The odd-order splitting coefficients are caused by the rotation of the Sun, and will

not be directly considered in this work. The even-order coefficients are caused by second order effects of rotation, and by the effects of magnetic fields.

The basic equations

We begin with the equations for conservation of mass, momentum, and energy:

$$\frac{\partial \rho}{\partial t} = -\nabla \cdot (\rho \vec{v}), \quad (2.3)$$

$$\rho \frac{d\vec{v}}{dt} = -\nabla p + \rho \vec{f}, \quad (2.4)$$

and

$$\rho \frac{dq}{dt} = \rho \epsilon - \nabla \cdot F_R, \quad (2.5)$$

where ρ is the density, p is the pressure, \vec{v} is the velocity of the gas, \vec{f} is the external force acting on the gas, dq/dt is the rate of heat gain or loss, ϵ is the energy generation rate, and F_R is the radiative flux. We have neglected viscous effects in equation (2.4), and will not consider the contribution of viscous heating to ϵ . In most of the solar interior, this is undoubtedly a good approximation, though turbulent viscosity in the convection zone may have some non-negligible contributions. Equations (2.3)–(2.5) are the Navier-Stokes equations for an inviscid flow.

The relation between the full derivative of a quantity x with respect to time and its partial time derivative is given by

$$\frac{dx}{dt} = \frac{\partial x}{\partial t} + \vec{v} \cdot \nabla x. \quad (2.6)$$

Using this, we can rewrite equation (2.4) as:

$$\rho \frac{\partial \vec{v}}{\partial t} + \rho \vec{v} \cdot \nabla \vec{v} = -\nabla p + \rho \vec{f}. \quad (2.7)$$

For the force \vec{f} , we consider only gravity. Thus,

$$\vec{f} = \vec{g} = \nabla\Phi, \quad (2.8)$$

where Φ is the gravitational potential. We may relate the potential to the distribution of matter using the Poisson equation:

$$\nabla^2\Phi = 4\pi G\rho. \quad (2.9)$$

For this discussion, we approximate the radiative flux as a diffusive process; thus

$$F_r = -K\nabla T, \quad (2.10)$$

where K is the radiative conductivity of the stellar material.

The energy equation (2.5) can also be rewritten using the following relations, known as the adiabatic exponents:

$$\Gamma_1 = \left(\frac{\partial \ln p}{\partial \ln \rho} \right)_{\text{ad}}, \quad \Gamma_3 - 1 = \left(\frac{\partial \ln T}{\partial \ln \rho} \right)_{\text{ad}}. \quad (2.11)$$

Then dq/dt can be written:

$$\frac{dq}{dt} = \frac{1}{\rho(\Gamma_3 - 1)} \left(\frac{dp}{dt} - \frac{\Gamma_1 p}{\rho} \frac{d\rho}{dt} \right). \quad (2.12)$$

The form (2.5) is more useful for formulating the equations of stellar structure; the form (2.12) is of more use in writing down the oscillation equations.

The equilibrium, static state can be obtained by setting all time derivatives and the velocity \vec{v} to zero. We denote the equilibrium quantities in the usual way with a subscript 0: i.e. ρ_0, p_0 , etc. Then, equations (2.3), (2.5), (2.7), (2.9), and

(2.10) become:

$$-\nabla p_0 - \rho_0 \nabla \Phi_0 = 0, \quad (2.13)$$

$$\rho_0 \epsilon_0 - \nabla \cdot F_0 = 0, \quad (2.14)$$

$$\nabla^2 \Phi_0 = 4\pi G \rho_0, \quad (2.15)$$

and

$$F_0 = -K_0 \nabla T_0. \quad (2.16)$$

We can write these equations explicitly in spherical coordinates, and assume spherical symmetry, and we obtain the familiar equations of stellar structure:

$$\frac{dp}{dr} = -\rho g, \quad (2.17)$$

$$\frac{dm}{dr} = 4\pi r^2 \rho, \quad (2.18)$$

and

$$\frac{dL}{dr} = 4\pi r^2 \rho \epsilon, \quad (2.19)$$

given here in their differential form as a function of the radius r . The temperature dependence can be found given an appropriate treatment of the radiative transfer.

The gravitational acceleration g at radius r is given by

$$g = \frac{Gm}{r^2}, \quad (2.20)$$

where m is the mass enclosed by a sphere of radius r , and the luminosity L is given by

$$L = 4\pi r^2 F. \quad (2.21)$$

The equations of oscillation

We now introduce small linear perturbations about the equilibrium state of equations (2.3) - (2.5) of the form

$$x(\vec{r}, t) = x_0(\vec{r}) + x'(\vec{r}, t), \quad (2.22)$$

which is the Eulerian perturbation of the quantity x — that is, the perturbation of a variable x at a fixed point \vec{r} . We may also follow an element in the gas as it is perturbed from \vec{r} to a position $\vec{r} + \delta\vec{r}$. This is called the Lagrangian perturbation, and is related to the Eulerian perturbation by

$$\delta x(\vec{r}) = x'(\vec{r}_0) + \delta\vec{r} \cdot \nabla x_0, \quad (2.23)$$

when high order terms are neglected.

We will denote hereafter the displacement $\delta\vec{r}$ by $\vec{\xi}$, as is common in the literature. We do not explicitly separate the displacement into its radial and horizontal components, as it is not particularly illuminating to do so, though in the actual calculations involving these equations, that must be done. We note that the time derivative of the Lagrangian perturbation is the perturbation in velocity, assuming the equilibrium state flow is zero:

$$\vec{v}' = \frac{\partial \vec{\xi}}{\partial t}, \quad \frac{d\vec{v}'}{dt} = \frac{\partial^2 \vec{\xi}}{\partial t^2}. \quad (2.24)$$

Then, because we are looking for oscillating solutions, so that $\vec{\xi}(t, \vec{r}) = e^{-i\omega t} \vec{\xi}(\vec{r})$, we can write

$$\frac{d\vec{v}'}{dt} = -\omega^2 \vec{\xi}. \quad (2.25)$$

We can write the Eulerian form of the perturbed basic equations as follows, neglecting all high order terms:

$$\frac{\partial \rho'}{\partial t} + \nabla \cdot (\rho_0 \vec{v}) = 0, \quad (2.26)$$

$$\rho_0 \frac{\partial \vec{v}}{\partial t} + \nabla p' + \rho_0 \nabla \Phi' + \rho' \nabla \Phi_0 = 0, \quad (2.27)$$

$$\frac{\partial \delta q}{\partial t} = \frac{1}{\rho_0(\Gamma_{3,0} - 1)} \left(\frac{d\delta p}{dt} - \frac{\Gamma_1 p}{\rho} \frac{d\delta \rho}{dt} \right), \quad (2.28)$$

and

$$\nabla^2 \Phi' = 4\pi G \rho'. \quad (2.29)$$

These are the linear equations of oscillation. The adiabatic form is given by neglecting the heating term on the left hand side of equation (2.28):

$$\frac{d\delta p}{dt} - \frac{\Gamma_1 p}{\rho} \frac{d\delta \rho}{dt} = 0 \quad (2.30)$$

or

$$\delta p = \frac{\Gamma_{1,0} p_0}{\rho_0} \delta \rho \quad (2.31)$$

or again

$$p' + \vec{\xi} \cdot \nabla p_0 = c_0^2 (\rho' + \vec{\xi} \cdot \nabla \rho_0), \quad (2.32)$$

where $c^2 = \Gamma_1 p / \rho$ is the adiabatic sound speed.

The variational principal

In this section, we review the formulation of the inversion problem in helioseismology. In brief, we wish to relate changes in frequencies to changes in the structure of the Sun. These changes can be with respect to the theoretical frequencies of a model or to the actual frequencies of the Sun (measured, for example, at different

times — e.g. Chapter 3). We will begin by writing the time-independent part of the oscillation equation 2.27 (the time-dependant part can be written as $e^{-i\omega t}$ and separated) in the following form:

$$-\omega^2 \vec{\xi} = \mathcal{L} \vec{\xi}, \quad (2.33)$$

where the linear functional \mathcal{L} is

$$\mathcal{L} \vec{\xi} = -\frac{1}{\rho_0} \nabla p' + \nabla \Phi' + \frac{\rho'}{\rho_0} \nabla \Phi_0. \quad (2.34)$$

Following Christensen-Dalsgaard (1981), we define the Hilbert space \mathcal{H} of displacement functions defined on a spherical star with the appropriate regularity and boundary conditions. Then, define the inner product $\langle \vec{\xi}, \vec{\eta} \rangle$ on \mathcal{H} by

$$\langle \vec{\xi}, \vec{\eta} \rangle = \int_V \rho_0 \vec{\xi}^* \cdot \vec{\eta} dV, \quad (2.35)$$

where $\vec{\xi}^*$ is the complex conjugate of $\vec{\xi}$ and the integral is evaluated over the entire volume of the star. If we take the adiabatic version of the operator \mathcal{L} , which we denote \mathcal{L}_a by including equations (2.26) and (2.32):

$$\mathcal{L}_a \vec{\xi} = -\frac{1}{\rho_0} \nabla (c^2 \rho_0 \nabla \cdot \vec{\xi} + \vec{\xi} \cdot \nabla p_0) + \nabla \Phi' + \frac{\rho'}{\rho_0} \nabla \Phi_0, \quad (2.36)$$

it can be shown (Lynden-Bell & Ostriker 1967) that this operator is symmetric, i.e.

$$\langle \vec{\xi}, \mathcal{L}_a(\vec{\eta}) \rangle = \langle \mathcal{L}_a(\vec{\xi}), \vec{\eta} \rangle. \quad (2.37)$$

From this it follows that the squared eigenfrequencies are real (see Aerts et al.

2010, for the proof), and that the eigenfunctions are orthogonal, that is, if

$$-\omega_1^2 \vec{\xi}_1 = \mathcal{L}_a \vec{\xi}_1; \quad -\omega_2^2 \vec{\xi}_2 = \mathcal{L}_a \vec{\xi}_2; \quad \omega_1^2 \neq \omega_2^2, \quad (2.38)$$

then

$$\langle \vec{\xi}_1, \vec{\xi}_2 \rangle = 0. \quad (2.39)$$

Taking the perturbations $\delta\omega$, $\delta\vec{\xi}$, and $\delta\mathcal{L}$ (dropping the subscript a), we can perturb equation (2.33):

$$-(\omega_0 + \delta\omega)^2 (\vec{\xi}_0 + \delta\vec{\xi}) = (\mathcal{L}_0 + \delta\mathcal{L}) (\vec{\xi}_0 + \delta\vec{\xi}). \quad (2.40)$$

From this equation, we can obtain the first order contributions to $\delta\omega$ from $\delta\mathcal{L}$ — the contributions from $\delta\vec{\xi}$ all drop out:

$$\frac{\delta\omega}{\omega_0} = -\frac{\langle \vec{\xi}_0, \delta\mathcal{L} \vec{\xi}_0 \rangle}{2\omega_0^2 \langle \vec{\xi}_0, \vec{\xi}_0 \rangle}. \quad (2.41)$$

This form is due to the operator \mathcal{L} being Hermitian, as was shown by Chandrasekhar (1964). Thus, a variational principal applies, which is at the heart of the inversion techniques we apply in helioseismology. The variational principal states, in effect, that perturbations to the structure of a star cause first order perturbations in the eigenfrequencies but second order perturbations to the eigenfunctions. Thus, we can relate perturbations in frequencies directly to perturbations in structure. The product in the denominator is essentially the mode mass (some authors refer to this as the mode inertia or the mode kinetic energy). We will denote this quantity E_k :

$$E_k = \langle \vec{\xi}_0, \vec{\xi}_0 \rangle. \quad (2.42)$$

The perturbed operator $\delta\mathcal{L}$ is

$$\begin{aligned} \delta\mathcal{L}\vec{\xi} = & \nabla(\delta c^2 \nabla \cdot \vec{\xi} + \delta \vec{g} \cdot \vec{\xi}) + \nabla \left(\frac{\delta \rho}{\rho} \right) c^2 \nabla \cdot \vec{\xi} + \\ & \frac{1}{\rho} \nabla \rho \delta c^2 \nabla \cdot \vec{\xi} + \delta \vec{g} \nabla \cdot \vec{\xi} - G \nabla \int_V \frac{\nabla \cdot (\delta \rho \vec{\xi})}{|\vec{r} - \vec{r}'|} dV, \end{aligned} \quad (2.43)$$

where δc^2 and $\delta \rho$ are the changes in the squared sound speed and density, respectively, and the change in gravitational acceleration $\delta \vec{g}$ can be written in terms of $\delta \rho$. Then equation (2.41) can be written in the form

$$\frac{\delta \omega}{\omega_0} = -\frac{1}{2\omega^2 E_k} (I_1 + I_2 + I_3 + I_4), \quad (2.44)$$

where I_1 is an integral over the radius of the star that depends on $\delta c^2/c^2$ and I_2, I_3 , and I_4 are integrals that depend on $\delta \rho/\rho$. These four terms can be found in, e.g., Antia & Basu (1994); we do not bother to repeat them here. The perturbation in ω can then be written in the following form:

$$\frac{\delta \omega_i}{\omega_i} = \int \mathcal{K}_{c^2, \rho}^{(i)}(r) \frac{\delta c^2}{c^2}(r) dr + \int \mathcal{K}_{\rho, c^2}^{(i)}(r) \frac{\delta \rho}{\rho}(r) dr, \quad (2.45)$$

where $\mathcal{K}_{c^2, \rho}^{(i)}(r)$ and $\mathcal{K}_{\rho, c^2}^{(i)}(r)$ are functions of the reference model which describe the sensitivity of the i^{th} eigenfrequency to changes in the model at various depths. These are known as the inversion kernels. The power of the variational principal is apparent here — we do not need to recompute the kernels for the perturbed model when we invert for structure. To first order, the eigenfunctions and therefore the kernels are stationary about small perturbations to the underlying structure.

The surface term

Assuming a perfectly modeled star, and assuming that the normal modes of oscillation are completely adiabatic, equation (2.45) completely describes the (first order) effects of changes in structure on the frequencies of oscillation ω . Neither of these assumptions are fully valid. Non-adiabatic effects are negligible in most of the Sun, but near the surface they can become significant. Errors in the modelling of the structure arise principally from failing to properly treat convective processes (Balmforth 1992; Guenther 1994; Robinson et al. 2003). This causes both differences between the models and the actual star in the sound speed and density profiles, as well as giving rise to errors in the wave propagation treatment by neglecting the effects of turbulent viscosity and energy transport. Fortunately, however, both effects become significant only in the very shallow layers of the Sun (Gough 1990; Guzik & Cox 1992; Robinson et al. 2003). Because of this, errors in our treatment of frequency calculations affect frequencies independent of the mode geometry, characterized by the degree ℓ . The effect of errors depends only, then, on the frequency ω_i of the mode and of the inertia of that mode. Thus, when scaled appropriately by the mode inertia, the effects of non-adiabaticity and errors in modelling are a slowly varying function of frequency which we call the surface term $F_{\text{surf}}(\omega)$. We can then rewrite equation (2.45) as

$$\frac{\delta\omega_i}{\omega_i} = \int \mathcal{K}_{c^2,\rho}^{(i)}(r) \frac{\delta c^2}{c^2}(r) dr + \int \mathcal{K}_{\rho,c^2}^{(i)}(r) \frac{\delta\rho}{\rho}(r) dr + \frac{F_{\text{surf}}(\omega_i)}{E_i}. \quad (2.46)$$

Rotation and magnetic fields

Equation (2.33) is valid only for a non-rotating, non-magnetic star. We can include the effects of slow rotation and magnetic fields with some additional effort. The formalism used in this work was developed by Gough & Thompson (1990) and

we sketch the development in this section. Given a characteristic rotation rate Ω_s and a characteristic field strength \bar{B} , we can define the dimensionless quantities $\epsilon = \Omega_s(GM/R^3)^{1/2}$ and $\delta = \bar{B}(\mu_0 GM^2/R^4)^{1/2}$. The oscillation equation can be written, as was shown by Lynden-Bell & Ostriker (1967),

$$\mathcal{L}\vec{\xi} + \rho\omega^2\vec{\xi} = \epsilon\omega\mathcal{M}\vec{\xi} + \epsilon^2\mathcal{N}\vec{\xi} + \delta^2\mathcal{B}\vec{\xi}, \quad (2.47)$$

where

$$\mathcal{M}\vec{\xi} = -2i\rho\vec{v} \cdot \nabla\vec{\xi} \quad (2.48)$$

$$\mathcal{N}\vec{\xi} = -\rho\vec{\xi} \cdot \nabla(\vec{v} \cdot \nabla\vec{v}) + \rho(\vec{v} \cdot \nabla)^2\vec{\xi}, \quad (2.49)$$

$$\mathcal{B}\vec{\xi} = -\frac{\nabla \cdot (\rho\vec{\xi})}{\rho}(\nabla \times \vec{B}) \times \vec{B} - (\nabla \times \vec{B}') \times \vec{B} - (\nabla \times \vec{B}) \times \vec{B}', \quad (2.50)$$

where $\vec{v} = \omega \times \vec{r}$, and $\vec{B}' = \nabla \times (\vec{\xi} \times \vec{B})$ is the linearized Eulerian perturbation to \vec{B} . The operators \mathcal{M} and \mathcal{N} describe the first and second order contributions from rotation, respectively, while \mathcal{B} is the second order contribution from the magnetic field. Both rotation and magnetic fields distort the structure of the star, and it is convenient to express this distortion by the transformation

$$x = (1 + \epsilon^2 h_\Omega(\vec{r}) + \delta^2 h_B(\vec{r})) \quad (2.51)$$

which maps points \vec{r} in the distorted star to points x in the undistorted star. The functions h_Ω and h_B are determined by the rotation profiles and the magnetic fields, respectively. In this case, $x = R$ maps to the surface of the distorted star. The quantities p, ρ, c^2 can be expanded in the same way, e.g.

$$\rho(r) = \rho_0(x) + \epsilon^2 \rho_\Omega(x) + \delta^2 \rho_B(x). \quad (2.52)$$

The operators (2.36, 2.48–2.50) can be expanded in the same way:

$$\mathcal{L}\vec{\xi} = \mathcal{L}_0\vec{\xi} + \epsilon^2\mathcal{L}_\omega\vec{\xi} + \delta^2\mathcal{L}_B\vec{\xi}, \quad (2.53)$$

although for \mathcal{N} , \mathcal{M} , and \mathcal{B} , we need only retain the leading terms. We can separate the solution to equation (2.47) into an unperturbed, spherically symmetric solution $\vec{\xi}_0$, ω_0 , which satisfy (2.33), and a distorted eigenfunction $\vec{\xi}_1$ and the correction to the frequency ω_1 :

$$\vec{\xi} = \vec{\xi}_0 + \vec{\xi}_1, \quad \omega = \omega_0 + \omega_1. \quad (2.54)$$

We can expand (2.47) by substituting in the definition (2.54) and the perturbed thermodynamic variables, and applying the condition on $\vec{\xi}_0$ from (2.33), and retaining terms to second order:

$$\begin{aligned} (\mathcal{L}_0 + \rho_0\omega_0^2)\vec{\xi}_1 = & -2\rho_0\omega_0\omega_1\vec{\xi}_0 + \epsilon\omega_0\mathcal{M}_0\vec{\xi}_0 + \epsilon^2(\mathcal{N}_0 - \mathcal{L}_\Omega - \rho_\Omega\omega_0^2)\vec{\xi}_0 \\ & + \delta^2(\mathcal{B}_0 - \mathcal{L}_B - \rho_B\omega_0^2)\vec{\xi}_0 - \rho_0\omega_1^2\vec{\xi}_0 - 2\rho_0\omega_0\omega_1\vec{\xi}_1 + \epsilon\omega_0\mathcal{M}_0\vec{\xi}_1 + \epsilon\omega_1\mathcal{M}_0\vec{\xi}_0. \end{aligned} \quad (2.55)$$

By taking the scalar product of (2.55) with $\vec{\xi}_0$, we obtain

$$\begin{aligned} 2\omega_0\langle\rho_0\vec{\xi}_0, \vec{\xi}_0\rangle\omega_1 = & \langle\vec{\xi}_0, (\mathcal{N}_0 - \mathcal{L}_\Omega - \rho_\Omega\omega_0^2)\vec{\xi}_0\rangle + \langle\vec{\xi}_0, (\mathcal{B}_0 - \mathcal{L}_B - \rho_B\omega_0^2)\vec{\xi}_0\rangle \\ & - \omega_1^2\langle\rho_0\vec{\xi}_0, \vec{\xi}_0\rangle - 2\omega_0\omega_1\langle\rho_0\vec{\xi}_0, \vec{\xi}_1\rangle + \omega_1\langle\vec{\xi}_0, \mathcal{M}_0\vec{\xi}_0\rangle + \omega_0\langle\vec{\xi}_0, \mathcal{M}_0\vec{\xi}_1\rangle. \end{aligned} \quad (2.56)$$

We should note here that the inner product $\langle \dots \rangle$ is no longer given by equation (2.35), and is instead now simply the volume integral over the star:

$$\langle\vec{\xi}, \vec{\eta}\rangle = \int_V \vec{\xi}^* \cdot \vec{\eta} dV, \quad (2.57)$$

and when we wish to include the density ρ in the product, we do so explicitly. The combined operators here are not symmetric and hermitian as the single operator \mathcal{L} is. By neglecting all second order perturbations, we can see from equation (2.56) that the first order perturbation to the frequencies due to rotation is given by

$$\omega_{1(\text{rot})} = \epsilon \frac{\langle \vec{\xi}_0, \mathcal{M}_0 \vec{\xi}_0 \rangle}{2 \langle \rho_0 \vec{\xi}_0, \vec{\xi}_0 \rangle}. \quad (2.58)$$

The second order contribution from rotation is

$$\begin{aligned} \omega_{2(\text{rot})} = \epsilon^2 \left(\langle \vec{\xi}_0, (\mathcal{N}_0 - \mathcal{L}_\Omega - \rho_\Omega \omega_0^2) \vec{\xi}_0 \rangle + \frac{\omega_{1(\text{rot})}^2}{2\omega_0} - \frac{\omega_{1(\text{rot})} \langle \rho_0 \vec{\xi}_0, \vec{\xi}_1 \rangle}{\langle \rho_0 \vec{\xi}_0, \vec{\xi}_0 \rangle} \right. \\ \left. + \frac{\langle \vec{\xi}_0, \mathcal{M}_0 \vec{\xi}_1 \rangle}{2 \langle \rho_0 \vec{\xi}_0, \vec{\xi}_0 \rangle} + \frac{\omega_{1(\text{rot})} \langle \vec{\xi}_0, \mathcal{M}_0 \vec{\xi}_0 \rangle}{2\omega_0 \langle \rho_0 \vec{\xi}_0, \vec{\xi}_0 \rangle} \right). \end{aligned} \quad (2.59)$$

Finally, the magnetic contribution can be written

$$\omega_{2(\text{mag})} = \delta^2 \frac{\langle \vec{\xi}_0, (\mathcal{B}_0 - \mathcal{L}_B - \rho_B \omega_0^2) \vec{\xi}_0 \rangle}{2\omega_0 \langle \rho_0 \vec{\xi}_0, \vec{\xi}_0 \rangle}. \quad (2.60)$$

Thus, the frequencies for a mode (n, ℓ, m) in a rotating, magnetized star can be computed to second order precision by computing the unperturbed frequency ω_0 , and separately computing the first order rotation correction (2.58), the the second order corrections from rotation (2.59) and from the magnetic field (2.60). Equation (2.2) can then be used to compute the splitting coefficients, and the model can be compared directly to helioseismic data.

The first order correction to the mode frequencies due to rotation affects only the odd-order splitting coefficients, while the second order correction affects only the even-order splitting coefficients. Thus, the odd-order coefficients can be used to determine the rotation profile $\Omega(r)$ (Thompson et al. 1996; Schou et al. 1998),

which can in turn be used to compute the second order rotation correction (Antia et al. 2000). This correction needs to be made if the magnetic perturbation δ^2 is comparable in size to ϵ^2 , which appears to be the case (Gough & Thompson 1990; Antia et al. 2000).

2.2.2 The inverse problem

Given equation (2.46), the inverse helioseismic problem consists in finding a way to determine the unknown quantities $\delta c^2/c^2(r)$, $\delta\rho/\rho(r)$, and $F_{\text{surf}}(\omega)$. The known quantities are the N observed frequency differences $\delta\omega_i/\omega_i$ and the kernels and mode masses which are known functions of the reference model. In addition, account must be taken of the uncertainties in $\delta\omega_i/\omega_i$, which we denote σ_i . We can approach this problem in one of two ways: we can either find functional forms for the two thermal quantities as a function of radius and the surface term as a function of frequency which minimizes some norm with respect to the observed frequencies, or we can construct linear combinations of the frequency differences to obtain averages of the quantities of interest, averaged over some function called the averaging kernel. The former technique will be employed using Regularized Least Squares (RLS), and the latter using the method known as Optimally Localized Averages (OLA).

Though we only explicitly construct the linear combination of frequencies in the OLA inversions, the RLS inversions implicitly obtain the same averaging kernels, as these are at the heart of any linear inversion. We define the averaging kernel $K_i(r)$ by

$$K_i(r) = \sum_i c_i \mathcal{K}_{c^2, \rho}^{(i)}(r). \quad (2.61)$$

The coefficients c_i are the inversion coefficients. The sound speed is then obtained

by

$$\left\langle \frac{\delta c^2}{c^2} \right\rangle = \sum_i c_i \frac{\delta \omega_i}{\omega_i}. \quad (2.62)$$

Some contribution from the cross-term (in this case, ρ) is unavoidable, and that contribution is given by the cross-term kernel $\mathcal{C}(r)$ given by

$$\mathcal{C}(r) = \sum_i c_i \mathcal{K}_{\rho, c^2}^{(i)}. \quad (2.63)$$

Unfortunately, the helioseismic inverse problem is not well-posed. This arises primarily from the problem of trying to select from an infinite model space (that is, the space of all physically reasonable functions of radius $\delta c^2/c^2$ and $\delta \rho/\rho$) using a finite set of observables (the frequency differences $\delta \omega_i$ and the radius of the Sun). For a more formal discussion of the problem, see Backus & Gilbert (1967). In all cases, extra constraints (that the sound speed and density are positive definite, for example, and that mass must be conserved) are applied, but these are not sufficient. In RLS, the chief constraint employed is Tikhonov regularization where we encourage the second derivative to be as small as possible. In OLA, we do not explicitly obtain the functional form, settling instead for averages whose properties we know. Then the problem is how to select the averaging kernels that best suit our needs.

Regularized Least Squares (RLS)

The RLS inversion technique is the more familiar of the two employed in this thesis. The specifics of the inversion we use here are described in detail in Antia & Basu (1994). The problem is to find a solution to equation (2.46) by representing the

three unknown functions with a set of basis functions — in this case B-splines:

$$F(\omega) = \sum_i^m a_i \psi_i(\omega), \quad (2.64)$$

$$\frac{\delta c^2}{c^2}(r) = \sum_i^n b_i \phi_i(r), \quad (2.65)$$

$$\frac{\delta \rho}{\rho}(r) = \sum_i^n c_i \phi_i(r). \quad (2.66)$$

Then, if $\Delta\omega_i$ is

$$\Delta\omega_i = \sum_j b_j \int \phi_j(r) \mathcal{K}_{c^2, \rho}^{(i)} dr + \sum_j c_j \int \phi_j(r) \mathcal{K}_{\rho, c^2}^{(i)} dr + \sum_j a_j \psi_j(\omega_i) / E_i, \quad (2.67)$$

then RLS attempts to minimize the quantity

$$\chi^2 = \sum_i \left(\frac{\frac{\delta\omega_i}{\omega_i} - \Delta\omega_i}{\sigma_i} \right)^2 + \alpha^2 \int_0^R \left[q(r)^2 \left(\frac{d^2}{dr^2} \frac{\delta c^2}{c^2} \right)^2 + \left(\frac{d^2}{dr^2} \frac{\delta \rho}{\rho} \right)^2 \right]. \quad (2.68)$$

The second term in this equation is the regularization designed to promote a smooth solution. The parameter α is used to control the amount of smoothing, and we can basically trade smoothness of solution for smallness of errors. The function $q(r)$ allows us to control the amount of smoothing as a function of radius. We use $q(r) = 1/r$ so that the regularization parameter is larger in the core where there is less information.

In addition to the smoothing constraint, we apply the following five physically motivated constraints. Mass must be conserved:

$$\int_0^R r^2 \delta \rho dr = 0. \quad (2.69)$$

We also apply the four boundary conditions, two each at the core and at the

surface:

$$\begin{aligned} \frac{\delta c^2}{c^2} = 0, \quad \frac{\delta \rho}{\rho} = 0, \quad \text{at } r = R \\ \frac{d}{dr} \frac{\delta c^2}{c^2} = 0, \quad \frac{d}{dr} \frac{\delta \rho}{\rho} = 0, \quad \text{at } r = 0. \end{aligned} \quad (2.70)$$

The basic problem, then, consists of N observations and $2n + m$ unknown coefficients. In this work, the RLS inversion is solved by means of a Singular Value Decomposition (SVD) on the matrix A from the following equation:

$$A\mathbf{x} = \mathbf{d}, \quad (2.71)$$

where A is the $N \times (2n + m)$ matrix defined by the expansion from (2.64) - (2.66) to the equation (2.46), \mathbf{x} is a $2n + m$ vector containing the unknown coefficients, and d is the data vector containing the N observations. The i^{th} row of each matrix is divided by the error σ_i for that observation.

The SVD decomposes A into three matrices: $A = U\Sigma V^T$. U and V both have the property that their transpose is their inverse. Σ is a diagonal matrix whose elements s_i are the singular values of A . Equation (2.71) can then easily be solved for \mathbf{x} :

$$\mathbf{x} = V\Sigma^{-1}U^T\mathbf{d}. \quad (2.72)$$

The error $\sigma(x_k)$ in any component x_k is given by

$$\sigma(x_k)^2 = \sum_{i=1}^{2n+m} \frac{v_{ki}^2}{s_i^2}. \quad (2.73)$$

The smoothing constraint is implemented by discretizing the right-hand integral in (2.68) with the sums

$$\frac{\alpha}{\sqrt{M}} q(r_j) \left(\frac{d^2}{dr^2} \frac{\delta c^2}{c^2} \right)_{r=r_j} = \frac{\alpha}{\sqrt{M}} q(r_j) \sum_i^n b_i \frac{d^2}{dr^2} \phi_i(r_j) = 0, \quad (2.74)$$

defined at M points spaced equally in r , and

$$\frac{\alpha}{\sqrt{M}} q(r_j) \left(\frac{d^2}{dr^2} \frac{\delta \rho}{\rho} \right)_{r=r_j} = \frac{\alpha}{\sqrt{M}} q(r_j) \sum_i^n c_i \frac{d^2}{dr^2} \phi_i(r_j) = 0. \quad (2.75)$$

These $2M$ equations are added to the matrix A , as are the boundary conditions.

The selection of the appropriate inversion is non-trivial. There are two principal choices available to us in this inversions scheme: the regularization parameter α , and the placement of the points — called ‘knots’ — at which the B-splines are defined (e.g. Antia 2002). The placement of the knots for $\psi(\omega)$ is equally spaced in frequency. The knots for the function ϕ are placed equidistant in the acoustic depth τ , which is sensible since helioseismic modes have greater resolving power at shallower depths than at deeper depths. The number of knots in frequency are chosen to minimize non-random structure in the residuals when plotted as a function of frequency. The number of knots in radius are chosen to produce small χ^2 values, without allowing the condition number of the matrix A to grow too large. The value of the smoothing parameter is chosen to minimize the χ^2 value on the one hand and the $||L||^2$ value on the other, where L is the regularization term from equation (2.68).

Subtractive Optimally Localized Averages (SOLA)

As discussed above, the OLA technique tries to construct weighted averages of inversion quantities with sensitivity (hopefully) centered about some target radius r_0 . The OLA technique was developed for terrestrial seismology by Backus & Gilbert (1967, 1968), and its use in helioseismology was first described by Gough (1985). The implementation we use here is known as Subtractive Optimally Localized Averages (SOLA Pijpers & Thompson 1992, 1994), which has the advantage

over other OLA techniques of computational efficiency.

The SOLA technique minimizes the difference between the actual inversion averaging kernel (2.61) and a target kernel:

$$\int_R^0 [K(r_0, r) - \mathcal{T}(r_0, r)]^2 dr + \beta \int_R^0 \mathcal{C}^2 f(r) dr + \mu \bar{\sigma}^{-2} \sum_i c_i^2(r_0) \sigma_i^2, \quad (2.76)$$

where $\mathcal{K}(r_0, r)$ is the averaging kernel and $\mathcal{T}(r_0, r)$ is the target kernel. In this work, we use a target kernel of the form

$$\mathcal{T}(r_0, r) = A r \exp \left\{ - \left[\frac{r - r_0}{\Delta(r_0)} + \frac{\Delta(r_0)}{2r_0} \right]^2 \right\}, \quad (2.77)$$

where A is a normalization constant and $\Delta(r_0)$ is the kernel width, scaled to the sound speed relative to some fiducial depth (in this case, $r = 0.2R_\odot$) which we scale inversely with the sound speed. We control $\Delta(r_0)$, then, with a single parameter Δ_A :

$$\Delta(r_0) = \Delta_A \frac{c(r_0)}{c(r = 0.2R_\odot)}. \quad (2.78)$$

There are two trade-off parameters: μ which acts to suppress errors and β which suppresses the cross-term kernel.

As in the RLS inversions, we expand the surface term with set of Λ suitable basis functions — again, we use B-splines. We require that the surface term be small. We add, therefore, the constraint

$$\sum_i c_i \frac{\phi_j(\omega_i)}{E_i} = 0, \quad \text{for } j = 0, \dots, \Lambda. \quad (2.79)$$

Similarly to the RLS inversion, we can write the inversion as a linear system

of equations:

$$A\mathbf{x} = \mathbf{d} \quad (2.80)$$

by minimizing the expression in (2.76) and adding the extra constraints. We can then solve for the unknown \mathbf{x} . Inversion of the matrix A presents no unusual difficulty since it is symmetric, and standard numerical routines can be used.

The SOLA inversion, then, has four free parameters: the cross-term suppression term β , the error suppression term μ , the characteristic width of the target kernel Δ_A , and the number of B-splines used to expand F_{surf} , Λ . As in RLS, the number of B-splines Λ used to expand the surface term is chosen to eradicate any large-scale structure in the residuals as a function of frequency. The choice of the target kernel width Δ_A is chosen to make the resolution of the inversions as high as possible while simultaneously keeping error correlation between solutions at different target radii as small as possible and keeping the contribution from the cross-term as small as possible. Control over the error correlation and the cross-term contribution can also be exercised using the μ and β parameters, so selection of the appropriate inversion parameters is an iterative and fairly subjective process.

2.3 Results in helioseismology

In this section, we briefly review the history of helioseismology and the important results, particularly as they relate to the present work. As described above, Leighton et al. (1962) first reported solar oscillations, and Ulrich (1970) and Leibacher & Stein (1971) showed that these could be trapped oscillations in the solar interior. Such waves could therefore be used as a probe to study this interior, much as is done with seismic measurements on the Earth.

2.3.1 Studying the interior

One of the first problems addressed using helioseismology was the question of internal rotation. The surface of the Sun rotates with an average synodic period of 27 days, but this rotation is not uniform; the Sun rotates faster at the equator than at the poles. As seen earlier, rotation lifts the mode multiplet degeneracy and ‘splits’ the mode frequencies into $m = 2\ell + 1$ multiplet frequencies. The first detection of mode splitting (Duvall & Harvey 1984) indicated that there may not be strong depth dependence of internal rotation. Measurements of a range of m frequencies (Brown 1985; Duvall et al. 1986; Libbrecht 1989) allowed this question to be studied in detail. Analysis of these data (Brown et al. 1989), and inversions (Christensen-Dalsgaard & Schou 1988; Dziembowski et al. 1989; Kosovichev 1988, and subsequent work), continued to find rotation more or less constant on radial lines in the convection zone. Further, a zone of strong shear, dubbed the ‘tachocline’ (Spiegel & Zahn 1992), was detected at the base of the convection zone. A detailed analysis of the first 144 days of MDI data was undertaken by Schou et al. (1998), who presented a robust result that confirmed earlier detections of the tachocline and ruled out constant rotation on cylinders in the convection zone to a very high degree of confidence. For a detailed review of helioseismic determinations of solar rotation, see the review by Howe (2009).

Attempts to determine the thermal structure of the Sun using helioseismic data were first made by Christensen-Dalsgaard et al. (1985), who used an asymptotic inversion to determine the sound speed in the solar interior, and found reasonably good agreement with solar models. The base of the convection zone has been determined to great precision at $r = 0.713 \pm 0.001 R_{\odot}$ (Christensen-Dalsgaard et al. 1991; Basu 1997), and Christensen-Dalsgaard et al. (1993) showed that diffusion

played a significant role in the evolution of solar structure. More advanced inversions (of the type described above in section 2.2.2) were developed to make more precise measurements of the properties of the solar interior and test models of solar structure and evolution (e.g. Antia & Basu 1994; Antia 1996). The most important application of these techniques in the 1990s was in relation to the solar neutrino problem (see, e.g., Bahcall 1989) — the long-standing deficit of observed neutrinos compared to the predictions from solar models. Confronted with the excellent agreement between solar models and helioseismic tests (e.g. Bahcall et al. 1997, 1998), credence was given to the hypothesis that neutrinos had mass, and therefore could change ‘flavors’ as they travelled from the solar core to the Earth’s detectors. Subsequent work from the Sudbury Neutrino Observatory (Ahmad et al. 2001) confirmed the presence of a second flavor of neutrinos in the solar flux.

2.3.2 Local helioseismology

Early helioseismology concentrated on the ‘global’ problem: measuring and interpreting the global resonant modes of the Sun, which are sensitive to the structure of the Sun taken as a whole, and have only limited ability to distinguish one part of the Sun from another. There are, of course, phenomena of substantial interest to the solar physicist which are fundamentally local in character. The most obvious examples of these for the purposes of this work are active regions. The techniques of local helioseismology have been developed to study small-scale features of the Sun, especially active regions, but these techniques have also been applied to the global structure of the Sun in various ways.

Local helioseismology consists of studying small regions of the solar surface. Whereas global helioseismology uses standing waves with the entire Sun as an acoustic cavity, the waves studied in local helioseismology are generally travelling

waves whose lifetimes are too short to become globally resonant. This has the obvious advantage of allowing the helioseismologist to study the Sun in a spatially resolved way, but it also allows the study of shorter wavelength waves which probe shallower layers in the Sun.

The techniques of local helioseismology include Fourier-Hankel analysis (Braun et al. 1987), ring diagram analysis (Hill 1988), time-distance analysis (Duvall et al. 1993), and helioseismic holography (Lindsey & Braun 1990). Of these four, time-distance and ring diagram analysis are the most widely employed, and in this work we use only ring diagram analysis. For a review of the techniques, and important local helioseismic results, see the review by Gizon & Birch (2005), and references therein.

Ring diagram analysis consists of tracking a small patch of the Sun as it traverses the solar disk, and constructing a three-dimensional power spectrum of this patch. Ring diagrams take their name from the characteristic look of the power spectra at constant temporal frequency: (roughly) concentric rings in $k_x - k_y$ space. Fitting the whole power spectrum allows us to study both the structure and the dynamics of the region below the ring diagram patch. Further details on the construction and analysis of ring diagrams is given in Chapter 5.

Ring diagrams are most commonly used to study the dynamics of the near-surface layers of the Sun (e.g. Schou & Bogart 1998; Basu et al. 1999; Haber et al. 1999). They have also been used to study the characteristics of acoustic wave propagation in active regions (Haber et al. 2000; Rajaguru et al. 2001; Howe et al. 2004; Rabello-Soares et al. 2008), and they have been used to study the thermal structure of the Sun below active regions (Basu et al. 2004; Bogart et al. 2008). Ring diagrams have further been used to study the global asphericity of the near-surface layers (Basu et al. 2007).

2.3.3 Solar activity and helioseismology

Helioseismic frequencies are also known to exhibit changes over the course of the solar cycle. This was first suggested by Woodard & Noyes (1985) and confirmed soon after by Elsworth et al. (1990) and Libbrecht & Woodard (1990). It was quickly established that the frequency shifts were strongly correlated with surface activity (Woodard et al. 1991; Bachmann & Brown 1993; Elsworth et al. 1994; Regulo et al. 1994, etc.). Libbrecht & Woodard (1990) observed that the frequency shifts depended very strongly on mode frequency ν , and very weakly on degree ℓ of the mode, and Anguera Gubau et al. (1992) and Elsworth et al. (1994) confirmed these results. These authors concluded that all or most of the physical changes responsible for the changes in frequency were confined to the shallow layers of the Sun. In general, this picture has been confirmed in more recent studies (e.g., observational results: Howe et al. 1999a, 2002; Basu & Antia 2000; Verner et al. 2004; Dziembowski & Goode 2005, etc., and theoretical results: Goldreich et al. 1991; Balmforth et al. 1996; Li et al. 2003, etc.). A change in the second helium ionization zone at $r = 0.98R_{\odot}$, first suggested by Goldreich et al. (1991) and Gough (2002), has been confirmed by Basu & Mandel (2004) and Verner et al. (2006).

The even-order mode splitting parameters sample effects of structural asphericities on the mode frequency. Kuhn (1988) suggested that they were correlated with observed changes in surface temperature. Subsequent work has shown that the aspherical components of the mode frequencies are tightly correlated with surface magnetic activity (Howe et al. 1999a; Antia et al. 2001b). This high correlation lends further credence to the idea that frequency shifts are caused by surface and/or near-surface effects. This can be tested directly with high degree modes that sample the near-surface layers of the Sun. However, as the degree l increases, global

modes become increasingly hard to measure precisely due to the decrease in mode lifetimes (Rhodes et al. 1998; Rabello-Soares et al. 2001; Korzennik et al. 2004). The lack of reliable measurements of these modes has led some authors to use ring diagrams to measure high degree modes and measure changes in the shallow layers of the solar convection zone. These studies have confirmed that structural changes do occur in the near-surface layers of the Sun (Basu et al. 2007).

Direct inversions of changes in the structure of the solar interior probed by the spherically symmetric global modes have not yielded any measurable differences in the deep interior (Basu 2002; Eff-Darwich et al. 2002) and there have been upper limits placed on the changes at the base of the convection zone (Eff-Darwich et al. 2002). Chou & Serebryanskiy (2005) and Serebryanskiy & Chou (2005) have presented evidence of a possible change in mode frequencies with lower turning points near the base of the convection zone.

Internal dynamics, on the other hand, show clear and unequivocal evidence of change over the course of the solar cycle. In the convection zone, bands of different rotational velocities (called zonal flows) have been shown to migrate poleward at high latitudes and equator-ward at low latitudes (Schou 1999; Howe et al. 2000; Antia & Basu 2000, 2001). Temporal variations in dynamics have been shown to penetrate throughout the entire convection zone, and even below (Vorontsov et al. 2002; Basu & Antia 2006; Howe et al. 2005, 2006).

2.3.4 Magnetic Fields

Although helioseismic determinations of magnetic fields are difficult, there have been many attempts to do so. Isaak (1982) suggested that the then observed frequency splittings in the solar acoustic spectrum could be caused by a large scale magnetic field situated in the core. Dziembowski & Goode (1984) used an

asymptotic approximation to study the effects of magnetic field on the splitting coefficients, and Dziembowski & Goode (1988) argued that a 1 MG field at the base of the convection zone was necessary to explain the observed splitting coefficients. However, Basu (1997); Antia et al. (2000) placed a limit of 0.3 MG on the field at the base of the convection zone; thus the situation was unclear. A megaGauss magnetic field is also inconsistent with dynamo theories and constraints from other observations (e.g., D'Silva & Choudhuri 1993).

Gough & Thompson (1990) developed a formalism to compute the effects of rotation and axisymmetric magnetic fields on the frequency splittings (discussed in the following section), which Antia et al. (2000) used to analyze the first year of Michelson Doppler Imager (MDI) data. They placed limits on the strengths of internal toroidal fields, finding a limit of 20 kG at a depth of 30 Mm, and a limit of 300 kG at the base of the convection zone ($r = 0.713R_{\odot}$). Dziembowski et al. (2000) inverted the mean frequencies and splitting coefficients for changes in temperature, and found that the resulting temperature perturbation could be explained by a change in magnetic field of 60 kG at a depth of 45 Mm ($r \sim 0.93R_{\odot}$).

Dziembowski et al. (2001) found that changes in f -mode frequencies from solar minimum to solar maximum implied a decrease in solar radius with activity, which they associated with a change between 4 and 8 Mm in depth. In explaining this result with changing magnetic fields, they assumed a tangled field, but even so the magnitude of the change in field strength was strongly dependent on the radial distribution of the field. The change they required was 7 kG for a uniform field, or substantially less (1 kG at 8 Mm) for an inwardly increasing field. Chou & Serebryanskiy (2002, 2005) looked for signatures of a change at the base of the convection zone from low activity to high activity, and found signs of a small change, which they proposed could be due to a change in magnetic field of 170

– 290 kG. Baldner & Basu (2008), working with an entire solar cycle’s worth of helioseismic data, found a change in sound speed between solar maximum and solar minimum at the base of the convection zone, which, if due to a change in magnetic field, could indicate a change in field strength of 290 kG at that depth.

Chapter 3

Solar cycle related changes at the base of the convection zone

This chapter is adapted from a paper of the same title published in the Astrophysical Journal as Baldner, C.S. & Basu, S., 2008, ApJ, 686, 1361.

3.1 Introduction

Normal modes of oscillation of the Sun have provided a powerful tool to peer into the solar interior. In particular, modern experiments, both ground- and space-based, have measured the intermediate degree global oscillation spectrum with high precision since the beginning of solar cycle 23. Accurate determinations of interior structure and dynamics are now possible (see, e.g., review by Christensen-Dalsgaard 2002). These measurements contain a wealth of information about the fundamental causes of solar variability.

It is generally believed that the seat of the solar dynamo is located at the base of the convection zone (e.g., review by Charbonneau 2010). Because helioseismology

provides the only direct measurements of this region of the solar interior, these results can play an important role in constraining dynamo theories. In particular, a number of authors have attempted to use global and local helioseismic techniques to determine limits on the strength of the magnetic field at the base of the convection zone (e.g., Chou et al. 2003, and references therein). In this chapter, we attempt to improve helioseismic measurements of changes in this region.

Global modes of solar oscillation are described by three numbers that characterize the spherical harmonics that are used to define the horizontal structure of the mode. These are (1) radial order n that is related to the number of nodes in the radial direction, (2) the degree ℓ that is related to the horizontal wavelength of the mode, and (3) the azimuthal order m that defines the number of nodes along the equator. In a spherically symmetric star, the $2\ell + 1$ modes of an (n, ℓ) multiplet are degenerate, but effects that break spherical symmetry such as magnetic fields or rotation lift the degeneracy and give rise to frequency splittings. The frequencies $\nu_{n\ell m}$ of the modes within a multiplet can be expressed as an expansion in orthogonal polynomials:

$$\nu_{n\ell m} = \nu_{n\ell} + \sum_{j=1}^{j_{\max}} a_j(n, \ell) \mathcal{P}_j^{(\ell)}(m). \quad (3.1)$$

Early investigators (e.g., Duvall et al. 1986) commonly used Legendre polynomials, whereas now one often uses the Ritzwoller-Lavelly formulation of the Clebsch-Gordan expansion (Ritzwoller & Lavelly 1991) where the basis functions are polynomials related to the Clebsch-Gordan coefficients. In either case, the coefficients a_j are referred to as a -coefficients or splitting coefficients. Solar structure is determined by inverting the mean frequency $\nu_{n\ell}$, while the odd-order coefficients a_1, a_3, \dots depend principally on the rotation rate (Durney et al. 1988) and reflect

the advective, latitudinally symmetric part of the perturbations caused by rotation. Hence, these are used to determine the rate of rotation inside the Sun. The even order a coefficients on the other hand result from magnetic fields and asphericities in solar structure, and the second order effects of rotation (e.g., Gough & Thompson 1990; Dziembowski & Goode 1991).

One conclusion that can be drawn unequivocally from previous studies of the changes in solar structure is that any changes deeper than those in the outermost layers of the Sun are very small, and hence very difficult to detect through their signatures in oscillation frequencies. Chou & Serebryanskiy (2005) used a smoothing technique to attempt to remove the effect of surface variations, and found that the scaled frequency differences showed evidence of change near the base of the convection zone, but could not say more about the physical nature of the changes. Attempts to invert the frequencies directly have never shown any changes larger than the inversion errors (e.g., Basu 2002; Eff-Darwich et al. 2002). Therefore, although current helioseismic instruments have determined the solar oscillation frequencies with tremendous precision, statistical errors in those frequencies are still too large to make any direct detections of structure changes in the deep interior.

In this work, we take a somewhat different approach to attempting to detect changes at the base of the convection. We use Principal Component Analysis (PCA) to separate the frequency differences over the last solar cycle into a linear combination of different time-dependent components. This has the effect of decreasing the effects of measurement errors in the measured helioseismic frequencies, which allows us to isolate as precisely as possible the changes in frequency over time. In section 3.2, we describe the data used, and the methods employed to analyze them. In section 3.3, we present the results in detail. Finally, in section

3.4 we discuss the significance of the results and present our conclusions.

3.2 Data & analysis

3.2.1 Data

For this work, we use helioseismic global-mode data sets from two different projects, one from the Michelson Doppler Imager (MDI) on-board the SOHO spacecraft, and the other from the Global Oscillations Network Group (GONG). The MDI mode sets consist of frequencies and splittings obtained from 72-day long time series (Schou 1999). We use 54 of these sets, spanning the period from 1996 May 1 to 2007 May 16. The GONG mode sets are derived from 108-day time series (Hill et al. 1996). Although GONG provides sets that overlap in time, we only use non-overlapping sets in the present work. We use 40 sets from the period 1995 May 7 to 2007 April 14. Because the two sets are from completely different instruments and independent data reduction pipelines, any real solar signatures should show up in both sets. The f -modes do not sample the deep interior and are dominated by surface effects, so we exclude them from our study. The $n = 1$ modes have larger errors than the higher order modes, and so we exclude them as well. The included modes are low and intermediate degree modes up to $\ell = 176$, with order n from 2 to 16.

As a proxy for total solar activity, we use the 10.7cm radio flux measurements taken by the Dominion Radio Astrophysical Observatory (DRAO). This measurement has been found to be very tightly correlated with solar activity (e.g., Tapping 1987). We average the $F_{10.7}$ measurements over 72-day periods for comparison with MDI data, and 108-day periods for comparison with GONG data. For latitudinal structure in surface activity, we use the surface magnetic field, taken from

SOHO/MDI synoptic maps ¹. The magnetic field strengths are averaged over the same 72-day periods as the $F_{10.7}$ data, and over the appropriate ranges in latitude.

3.2.2 Method

We use Principal Component Analysis to describe the temporal variations of the weighted frequencies as a small number of uncorrelated basis functions. The use of PCA is a common technique in multivariate data analysis to reduce dimensionality and expose underlying variables (see F. Murtagh & A. Heck 1987, Chapter 2, for a discussion of its astrophysical applications). A brief description of the method and discussion of its limitations is included in the Appendix. PCA is a technique whereby a set of observations is expressed as a set of uncorrelated vectors. The usefulness of the technique arises from the fact that variation of the data about the first vector is maximal, and about the second vector, maximal subject to the constraint that it be orthogonal to the first vector, and so on. In other words, PCA provides a very efficient linear representation of a data set, and it is able to substantially reduce the dimensionality of the data set without losing any significant information.

It has been known for many years that the frequencies of the solar global modes of oscillation change with the solar activity cycle. With the arrival of high quality measurements of intermediate degree modes, it is clear that the amount of frequency shift over the solar cycle is dependent on the mode. Each mode has an associated mode inertia $E_{n\ell}$. Frequency differences can be scaled by the quantity $Q_{n\ell} = E_{n\ell}/\bar{E}_0(\nu_{n\ell})$, where $\bar{E}_0(\nu_{n\ell})$ is the inertia of the $\ell = 0$ modes interpolated to the frequency of the (n, ℓ) mode (Christensen-Dalsgaard & Berthomieu 1991).

¹MDI synoptic maps of Carrington rotations can be found at <http://soi.stanford.edu/magnetic/index6.html>

This scaling accounts for the fact that the frequencies of modes with lower inertia are changed by a larger amount than modes with a higher inertia by the same underlying perturbation. When scaled in this way, the degree-dependence of the frequencies over the solar cycle largely vanish, and the frequency changes become slowly varying functions of frequency only (e.g., Chaplin et al. 2001; Basu 2002).

Our data points are the scaled frequency differences $Q_{n\ell}\delta\nu_{n\ell}/\nu_{n\ell}$. For the MDI observations, there are 54 total mode sets in our work, which, when one is removed to be used as the base set, gives us 53 sets of scaled frequency differences. There are 40 mode sets in our GONG data set, or 39 difference sets. Because the PCA method requires a complete covariance matrix (see the Appendix), we can only include a mode if it is present in all mode sets. This dramatically reduces the amount of usable information, particularly since many excluded modes are missing in only one or two sets out of 53. For these modes, it is possible to interpolate a value for the missing frequency differences. In this case, because most of the frequency differences for the mode in question will be actually observed, any errors introduced through the interpolation will have a negligible effect on the PCA results. We tested two interpolation methods — one a spline interpolation along ridges in the ℓ - ν diagram (interpolated from modes with the same radial order n), and the other a linear interpolation between neighboring modes in time. When tested against existing modes, the interpolation along time proved superior, reproducing the actual data to better than a factor of 1.2σ , while the interpolation along the ridge results had a 2σ distribution. Therefore, only results using the time interpolation are discussed in this paper, but the PCA results using interpolation over degree were entirely consistent. Finally, to ensure that the PCA is robust, Monte Carlo simulations were performed to ensure that the exclusion of certain modes would not affect the results. The PCA analysis of these data appears to be

very robust. Errors in the PCA components were computed by means of a Monte Carlo simulation.

In addition to the mean frequencies $\nu_{n\ell}$, which contain information about the spherically symmetric part of the solar interior, we have the even-order splitting coefficients $a_{2j}(n, \ell)$, which allow us to reproduce mode frequencies as a function of latitude. Latitudinal frequencies as a function of colatitude θ can be obtained as follows:

$$\nu_{n\ell}(\theta) = \nu_{n\ell} + \sum_k \frac{\ell a_{2k}(n, \ell)}{\mathcal{Q}_{\ell k}} P_{2k}(\cos \theta), \quad (3.2)$$

where $\mathcal{Q}_{\ell k}$ are the angular integrals given by

$$\int_0^{2\pi} d\phi \int_0^\pi \sin \theta d\theta Y_\ell^m (Y_\ell^m)^* P_{2k}(\cos \theta) = \frac{1}{\ell} \mathcal{Q}_{\ell k} \mathcal{P}_{2k}^{(\ell)}(m), \quad (3.3)$$

and $P_{2k}(\cos \theta)$ are Legendre polynomials of degree $2k$, and the $\mathcal{P}_{2k}^{(\ell)}$ are the same polynomials as in equation 3.1.

Ultimately, we are interested in helioseismic data for what they can tell us about the solar interior. To extract this information, we invert these data sets for the parameters of interest. We use two different inversion techniques, and invert for the change in sound speed relative to the comparison frequency. The first technique used is Subtractively Optimized Local Averages (SOLA Pijpers & Thompson 1994). A description of the implementation used here, and how to select inversion parameters can be found in Rabello-Soares et al. (1999). The second inversion technique is that of Regularized Least Squares (RLS). The implementation used here and the selection of inversion parameters have been discussed in Antia & Basu (1994) and Basu & Thompson (1996). The use of these two techniques in tandem is crucial because the techniques are complimentary in nature (Sekii 1997). Inversions can be trusted if both inversion techniques return the same results.

The quantities which we invert are appropriately scaled eigenvectors from the PCA of the frequency differences. The differences are taken relative to some fiducial set, usually the first mode set (corresponding to activity minimum at the beginning of solar cycle 23). The eigenvectors, $\vec{\xi}_i$, are normalized so that $\vec{\xi}_i \cdot \vec{\xi}_i = 1$. Each data set is the vector $\vec{x}(t)$ that contains the individual mode frequencies $Q_{nl}\delta\nu_{nl}/\nu_{nl}$. These data can be represented as a linear combination of the the eigenvectors with coefficients given by $c_i(t) = \sum_j \xi_{ij}x_j(t)$ (see the Appendix). The scaled eigenvector $c_i(t)\vec{\xi}_i$, therefore, has a physically reasonable magnitude, and in all following cases, it is this quantity that we invert. In general, we choose the coefficient with the largest magnitude, which represents the largest variation in sound speed. This coefficient is usually the one associated with the set at maximum activity.

3.3 Results & discussion

3.3.1 Mean frequencies

We have performed the PCA decomposition of the MDI mean frequencies with respect to the first set (set #1216, start day 1996 May 1, end day 1996 July 12). This is a low activity set. The first four eigenvectors $\vec{\xi}_1 - \vec{\xi}_4$ are shown in Fig. 3.1, both as a function of frequency and of the lower turning point of the modes. The scaling coefficients for the first four eigenvectors are presented in Fig. 3.2. Also shown in the figure is the difference in the 10.7 cm radio flux between the first set and the subsequent sets.

When plotted as a function of frequency, the first eigenvector $\vec{\xi}_1$ appears to be almost entirely due to near-surface effects — it seems to be a slowly varying function of frequency only. As a function of r_t , however, a change in the average level of the frequency differences can be seen below the base of the convection zone

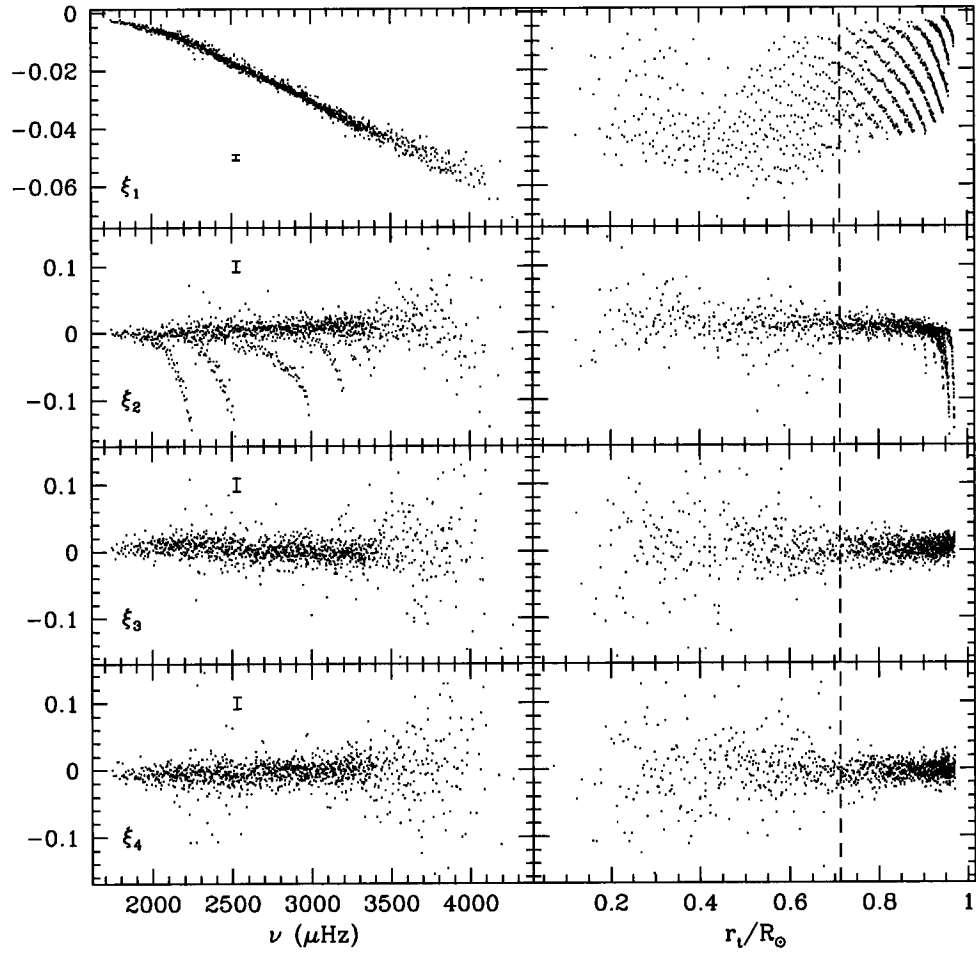


Fig. 3.1.— The first four eigenvectors for the MDI data set are shown. The base set is #1216 (1996 May 1). The left-hand panels show the eigenvectors as a function of frequency, and the right-hand panels show them as a function of the lower turning point of the mode. The vertical line shows the position of the base of the convection zone. The vertical axis units are arbitrary (the vectors are normalized so that $\vec{\xi}_i \cdot \vec{\xi}_i = 1$). The error bars show representative errors calculated using a Monte Carlo simulation.

(around $r \approx 0.713R_{\odot}$ — marked by a vertical line in Fig. 3.1). This implies a time dependent change near the base of the solar convection zone. We conclude, therefore, that there is a statistically significant component of the frequency variability picked out by $\vec{\xi}_1$ that does not originate at the surface. The coefficients for $\vec{\xi}_1$ are tightly correlated with the 10.7cm radio flux, a proxy for surface activity; the correlation coefficient is 0.99. A linear regression fit to the change in radio flux relative to solar minimum, $\Delta F_{10.7}$, gives the relation between the 10.7cm flux and the coefficients of $\vec{\xi}_1$ as:

$$c_1 = (2.53 \times 10^{-5} \pm 3.13 \times 10^{-6})\Delta F_{10.7} + 3.95 \times 10^{-5} \pm 1.6 \times 10^{-4}. \quad (3.4)$$

Thus, all changes, as manifest by $\vec{\xi}_1$, are tightly correlated with surface magnetic activity.

The second eigenvector, $\vec{\xi}_2$, also shows variability over the solar cycle. Comparing it as a function of ν and of r_t , it is clear that the structure is neither a pure function of frequency nor of lower turning point. The first four obvious downturn features correspond to modes of order $n = 2, 3, 4$, and 5. As a function of r_t , it seems clear that the structure is concentrated at or near the surface. However, the differences can not be fit by the usual “surface term”, and further examination reveals that it cannot be fit even by higher-order surface terms of the form considered in Brodsky & Vorontsov (1993) and Antia (1995). The coefficients for $\vec{\xi}_2$ offer some hint as to what is going on. They exhibit no obvious solar cycle dependency, but rather seem to be a roughly linearly decreasing function of time. There does not seem to be any periodicity on a scale of eleven years or shorter. Larson & Schou (2008) have undertaken an in depth study of the systematics in the MDI data reduction pipeline. The plate scale in the MDI instrument has changed

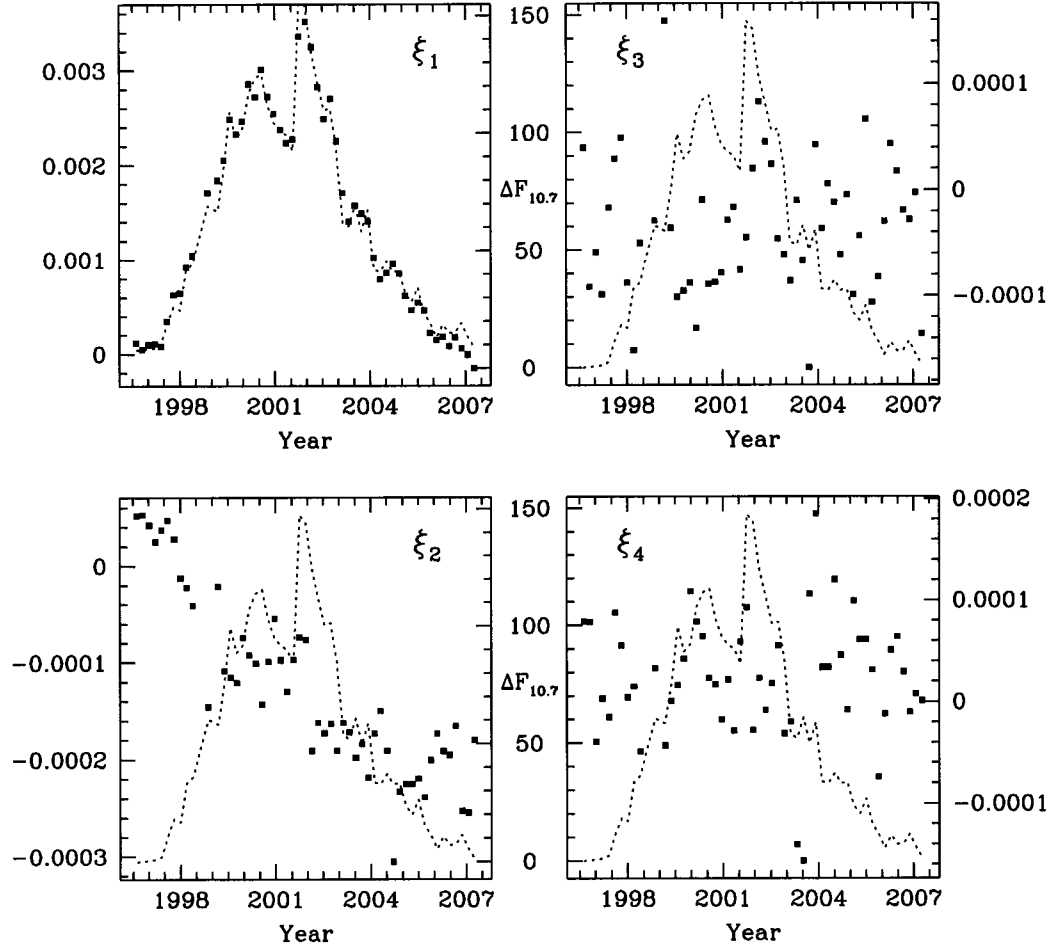


Fig. 3.2.— The scaling coefficients for the first four eigenvectors are shown as points. They are shown as a function of time (the start date of the MDI mode sets). The dotted line is the change in 10.7cm radio flux with respect to the beginning of the solar cycle. The units are Solar Flux Units (SFU).

slightly over the course of SOHO's mission, and they have shown that the effect of the resultant error in the measured radius introduces errors that look exactly like the $\vec{\xi}_2$ eigenvector computed in this work. We do not believe, therefore, that the features in $\vec{\xi}_2$ are solar in origin, but are rather artifacts from the MDI data reduction pipeline. As we will show below, analysis of GONG data confirms our belief.

The third and fourth eigenvectors, $\vec{\xi}_3$ and $\vec{\xi}_4$ do not exhibit any significant structure at all. The vector $\vec{\xi}_3$ shows a slight trend with frequency, but the scaling coefficients c_3 are normally distributed, and we cannot identify any physical significance in this eigenvector. The remaining eigenvectors are statistically consistent with Gaussian noise distributed around zero. We conclude, therefore, that the temporal variation of the MDI frequencies is dependent on a linear combination of $\vec{\xi}_1$ and $\vec{\xi}_2$ alone. In Fig. 3.3, we show two data sets reconstructed from the first two eigenvectors. This figure shows that the PCA decomposition does indeed accurately capture the original data while significantly reducing the random scatter in the data. The residuals normalized by the errors are plotted, and are consistent with Gaussian noise, with distributions of 1.1σ and 0.9σ for the two cases. Having confirmed that the third and subsequent eigenvectors are Gaussian noise, we do not consider them further in this paper. This reduction in noise is important for attempting to invert the small signatures we are looking at here.

The fact that the PCA is applied to a set of mode sets relative to a single base set raises the possibility that we are unduly influenced by the choice of that base set. We therefore repeat the PCA taking a base set from halfway up the solar cycle: MDI set #2224 (start date: 1999 February 3, end date 1999 April 16, and an activity level during the 72 day period of $F_{10.7} = 130.7$ SFU). The eigenvectors are consistent with those obtained from the base #1216 set insofar as their inner

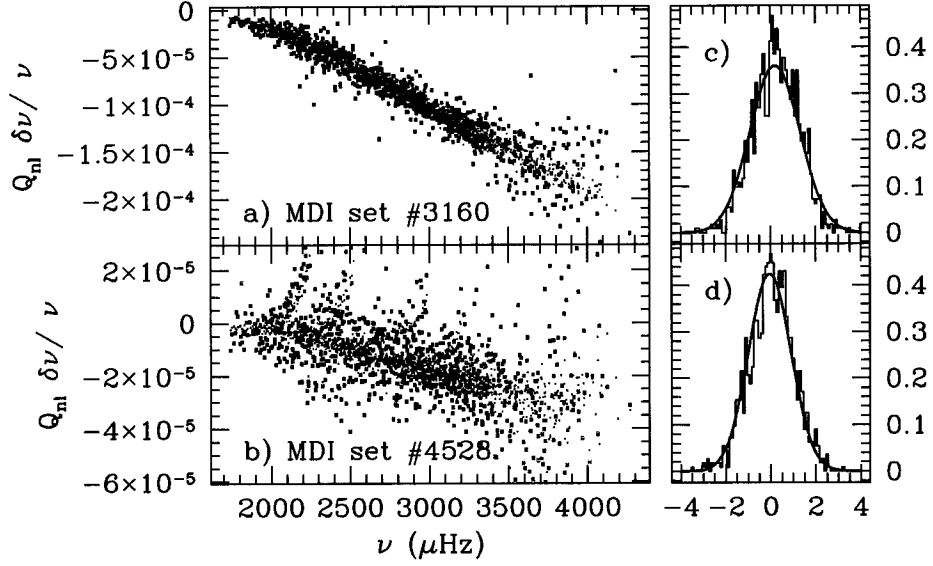


Fig. 3.3.— To demonstrate that the PCA representation of the data does indeed capture the actual data, we present two reconstructed data sets and compare them to the actual data. Two frequency difference sets are examined: sets #3160 (2001 August 27, panel a) and # 4528 (2005 May 26, panel b), both with respect to # 1216. At left, the frequency differences are plotted (panel (c) for set #3160 and panel (d) for set #4528). The actual data is shown in red, and the reconstructed data set using $\vec{\xi}_1$ and $\vec{\xi}_2$ are overplotted in black. The residuals, normalized by the errors in the measurements, are binned and shown against a Gaussian curve to show that the information which has been removed is statistically random.

products are close to unity. We conclude, therefore, that the PCA results are not unduly influenced by the choice of base set.

The mode parameters measured from GONG data are somewhat noisier than those measured from MDI data. Nevertheless, a similar analysis of the GONG data allows us to confirm results obtained from MDI data. The first two eigenvectors from the GONG observations are shown in Fig. 3.4. As with the MDI data, $\vec{\xi}_1$ plotted against r_t shows some structure in the deep interior. The second eigenvector, $\vec{\xi}_2$, shows no more structure than the MDI $\vec{\xi}_3$ eigenvector, and the remaining eigenvectors appear to be Gaussian noise, reinforcing our conclusions that the structure in $\vec{\xi}_2$ from the MDI data set is instrumental in origin.

We invert the appropriately scaled $\vec{\xi}_1$ eigenvectors to determine the change in the sound speed as a function of radius. We show the results of the inversion of the $\vec{\xi}_1$ vector with the #1216 base set in Fig. 3.5. This vector has been scaled by the coefficient for set #3160 (start date: 2001 August 27) in order to give the inversion results physical meaning. It is readily apparent that at a depth of $r \approx 0.713R_\odot$, near the location of the convection zone base, there is a change in the sound speed. This feature is well matched in both the RLS and the SOLA inversions, which implies that the feature is actually present in the data. The depression in sound speed at the base of the convection zone with increasing activity is matched with a corresponding enhancement below the convection zone. We invert the GONG data as well. The inversion results are shown in Fig. 3.5. There is a clear feature at the base of the convection zone, as seen with MDI data. The presence of this feature in the data of an independent instrument with an independent reduction pipeline is very encouraging — it strongly implies that the changes implied by the inversions are present in the Sun itself rather than artifacts in the data. Figure 3.5 shows the difference in sound speed between two extrema in the solar cycle.

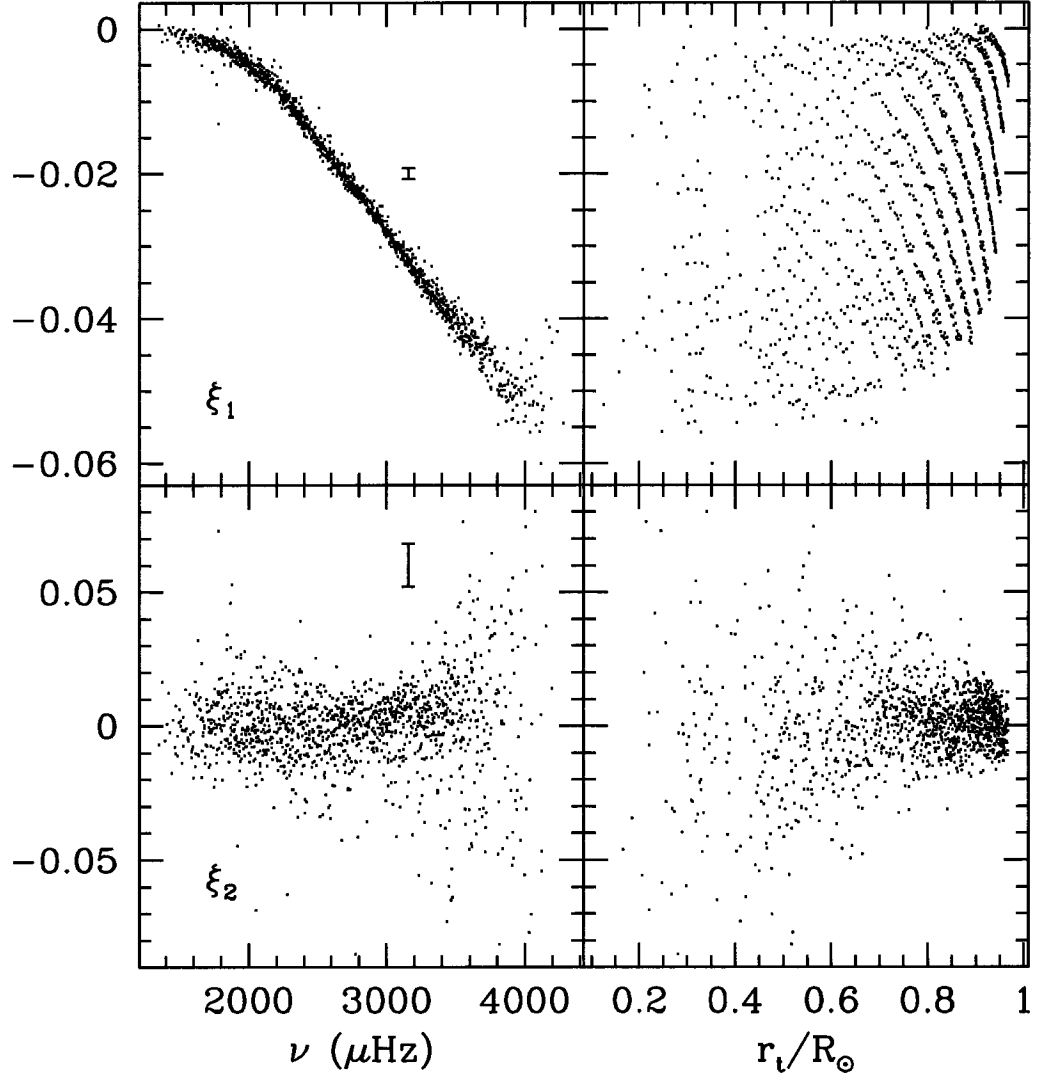


Fig. 3.4.— The first two eigenvectors for the GONG data sets plotted as a function of frequency (the left-hand panels) and as a function of the lower turning radius (the right-hand panels). The first eigenvector $\vec{\xi}_1$ shows a signature similar to the one seen in the MDI data, albeit much less obviously. The eigenvector $\vec{\xi}_2$ shows no structure, unlike the equivalent eigenvector for MDI, implying that the MDI $\vec{\xi}_2$ is an instrumental artifact.

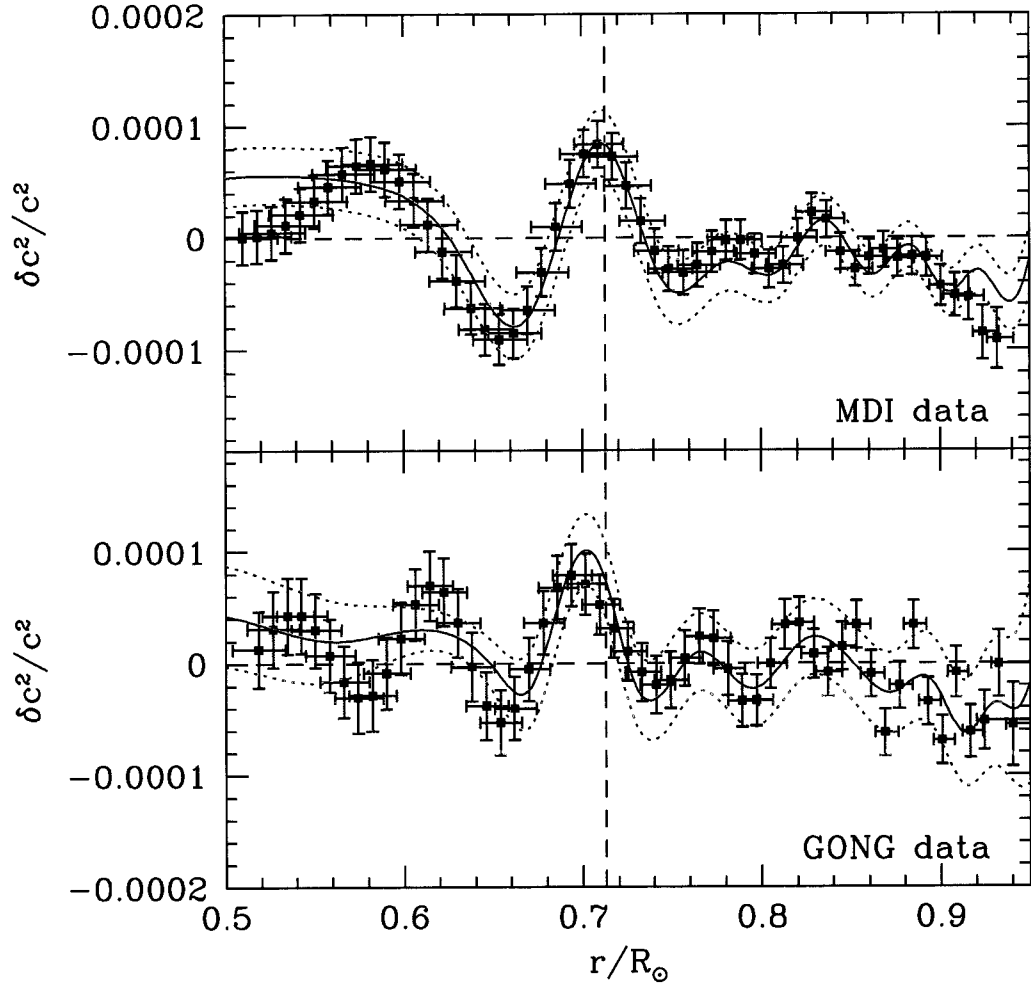


Fig. 3.5.— Inversion for sound speed of the $\tilde{\xi}_1$ eigenvector. The top panel shows the inversion of the MDI data. The lower panel shows the inversion of the GONG data. The solid cyan line is the result from the RLS inversion (the dotted lines are the vertical error bounds). The red points are the results from the SOLA inversion. The horizontal dashed line is the zero-point. The vertical dashed line represents the location of the base of the convection zone. At the convection zone base, the MDI inversion results show a clear depression in sound speed at high activity (the sense of the inversion is low activity minus high activity) and an enhancement in the tachocline region. The depression is matched in the GONG inversion results. The location of this feature, though slightly deeper, is within the horizontal errors of the MDI result.

To show how the interior changes with time, in Fig. 3.6 we show the sound speed inversions at three radii as a function of $\Delta F_{10.7}$.

We confirm, therefore, that the signature in mode frequencies is consistent with a change in structure at the base of the convection zone. Other authors have looked for changes in this region, but have not found any changes. The change that we have detected, while statistically significant, is very small, and it is only with the benefit of an entire solar cycle's worth of high precision observations that we can detect changes at this level. Basu & Antia (2001) examined the mode frequencies for evidence of a change in the location of the base of the convection zone. They did not detect any change, and the sound speed profile that we find in Fig. 3.5 is very different from the one they expected from a change in the base of the convection zone. This implies that, even if the change we are detecting is thermal in nature, it is unlikely to be related in any way to a change in the position of the base of the convection zone.

These inversions have been done assuming that the frequency differences are a result of a change in sound speed only. It is almost certain, however, given how tightly correlated this change is with solar activity, that the observed changes are related in some way to changes in the internal magnetic fields. What we have really inverted for, therefore, is a change in the *wave* speed. If we assume that the entire change is due to a change in the wave propagation speed due the presence of magnetic fields, in other words that $\delta c^2/c^2 \approx v_A^2/c^2$, as in Basu et al. (2004), we can obtain a value for B . The change at the base of the convection zone is $\delta c^2/c^2 = (7.23 \pm 2.08) \times 10^{-5}$, which implies a magnetic field strength of 290 kG. This is consistent with the results of earlier authors — Goode & Dziembowski (1993) placed an upper limit of 1MG on the toroidal field at the base of the convection zone, and Basu (1997) found that the magnetic field in this region

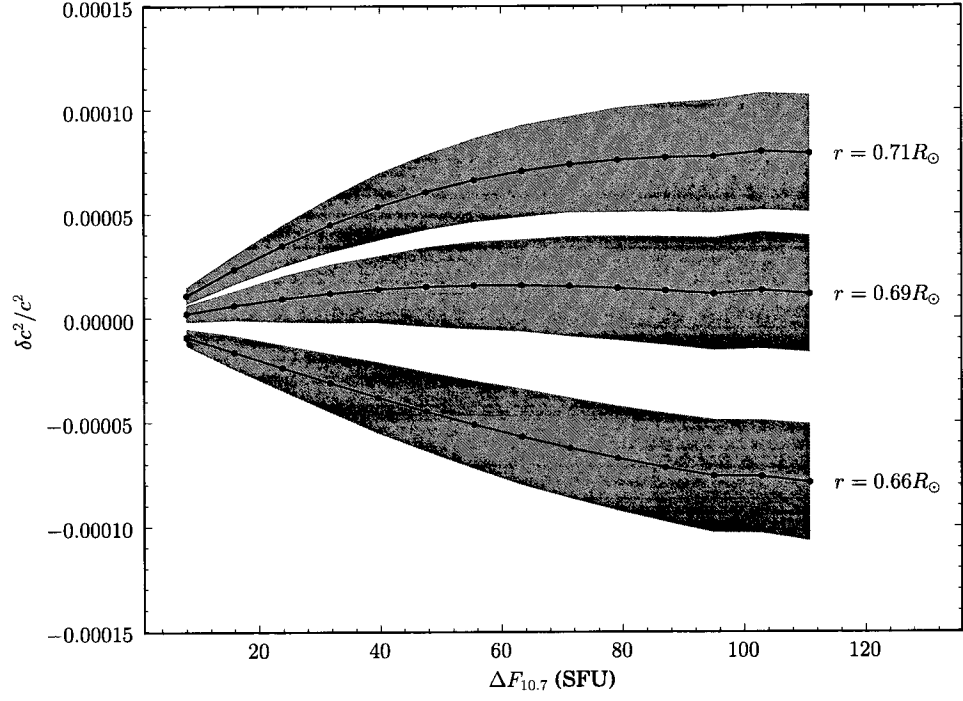


Fig. 3.6.— Change in inferred sound speed as function of activity level (10.7cm radio flux) is shown for different radii around the base of the convection zone. The shaded regions show the errors for each set of inversions.

could not exceed 300kG. Chou & Serebryanskiy (2002) found somewhat stronger fields (400 to 700kG).

3.3.2 Latitudinal changes

The MDI and GONG data sets also contain splitting coefficients. The even-order coefficients contain information about the non-spherically symmetric structure in the solar interior. Because the surface manifestations of solar activity are strongly latitudinally dependent, we have used these coefficients to study the temporal variability of structure at different latitudes. The frequencies corresponding to different latitudes are computed using equation 3.2. The PCA procedure is performed for each latitude as was done with the mean frequencies, and as usual is done with respect to set #1216. The first eigenvector for six different latitudes is shown in Fig. 3.7. When plotted as a function of frequency, the latitudes from the equator to 30° show a similar frequency dependence as in the case of the mean frequencies in Fig. 3.1. When plotted as a function of r_t , we see change at and below the convection zone base. The higher latitudes show no structure, and the eigenvectors for these latitudes are consistent with Gaussian noise. The scaling coefficients for each latitude as a function of time are shown in Fig. 3.8, along with the surface magnetic field. Like the scaling coefficients for the mean frequencies shown in Fig. 3.2, the latitudinal scaling coefficients closely follow the surface activity.

We show the sound speed inversions for the equator, 15° , 30° , and 45° in Fig. 3.9. The errors in the eigenvectors are larger here than for the mean frequencies, in large part because each frequency is a combination of mean frequency and splitting coefficients, each with their own errors. Nevertheless, there are several points of interest in these inversions. The first is a clear sound speed change for radii greater than approximately $r = 0.86R_\odot$ at 15° and the equator. The

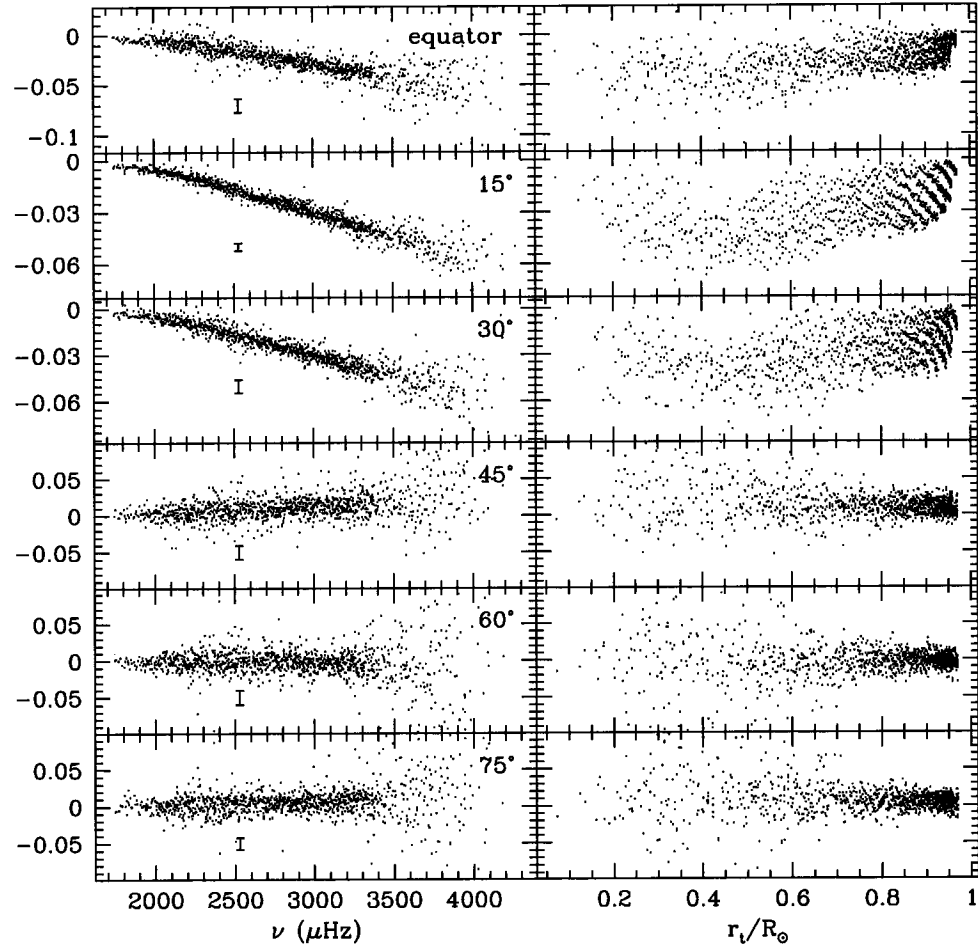


Fig. 3.7.— The first eigenvector $\vec{\xi}_1(\theta)$ for latitudes from 0° to 75° . The data are from MDI and are relative to the #1216 mode set. The left-hand panels show the eigenvectors as functions of frequency, and the right-hand panels as functions of the lower turning points.

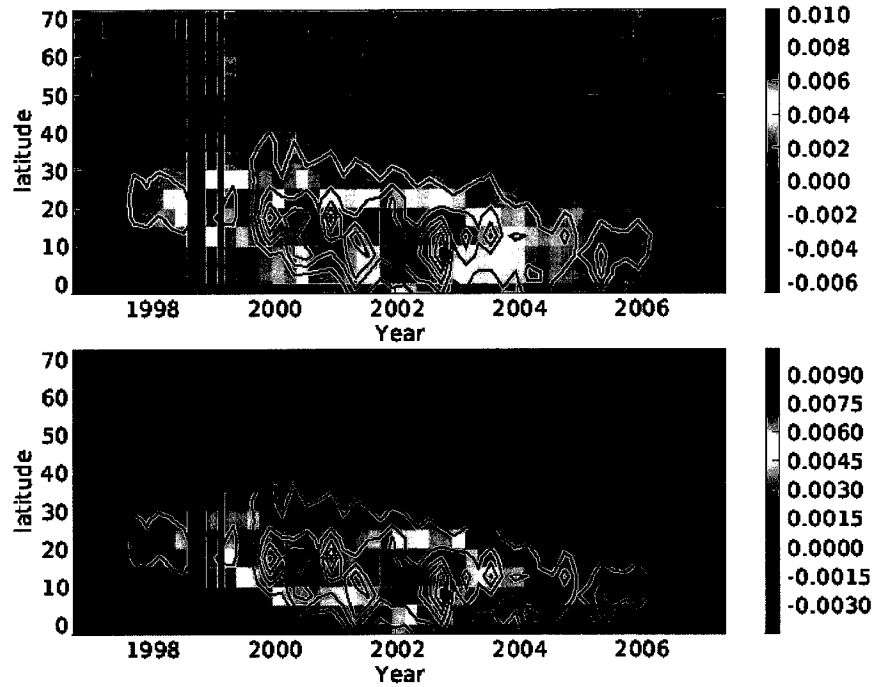


Fig. 3.8.— The scaling coefficients are plotted as a function of time and latitude. The top panel shows the coefficients for each individual eigenvector $\vec{\xi}_1(\theta)$. The bottom panel shows the scaling coefficients for all the latitudes as a function of the $\vec{\xi}_1(15^\circ)$. This shows how the changes represented by that eigenvector change as a function of both time and latitude. The average unsigned magnetic flux from MDI Carrington rotation synoptic maps over each 72-day period is shown in contour. The contours are spaced every 52G, with the lowest at 56.5G. The vertical bars in 1998 are gaps in MDI coverage due to spacecraft problems.

change seen in the SOLA inversion results is well matched in this region by the RLS inversion results, and the significance of the change approaches 2σ . There is the possibility, though less statistically significant, of a change at greater depth, i.e., approximately $r = 0.82R_{\odot}$. At 30° , a change in sound speed through the tachocline is seen in the RLS results, but it does not appear to be as clear in the SOLA results.. It is unclear whether or not this result is statistically significant. At latitudes of 45° and higher, the inversion errors become large, and the inversion results themselves become extremely sensitive to the inversion parameters. We conclude that there are no structural changes in the solar interior at or above a latitude of 45° large enough to be present in our data sets.

We have also analyzed directly the change in solar structural asphericity over the course of the solar cycle, by taking the scaled frequency differences of high latitudes with respect to the equator. For this analysis, therefore, we have 54 mode sets at each latitude. The difference is equator–latitude. Figure 3.10 shows the $\vec{\xi}_1$ eigenvectors for five different latitudes with respect to the equator. Clearly, the signal to noise in these data is worse than either the latitudinal frequencies or the mean frequencies, but radial structure is discernible in the eigenvectors for the equator relative to 15° , 30° , and 45° . In fig. 3.11, the scaling coefficients for the asphericity terms are shown. There is an evident phase delay in the scaling coefficients of 15° and 30° with respect to the equator. This is expected from Fig. 3.8. The scaling coefficients for higher latitudes (45° and 60° with respect to the equator) show no structure except for an abrupt change from mostly positive to negative, corresponding closely to the peak of the solar activity cycle.

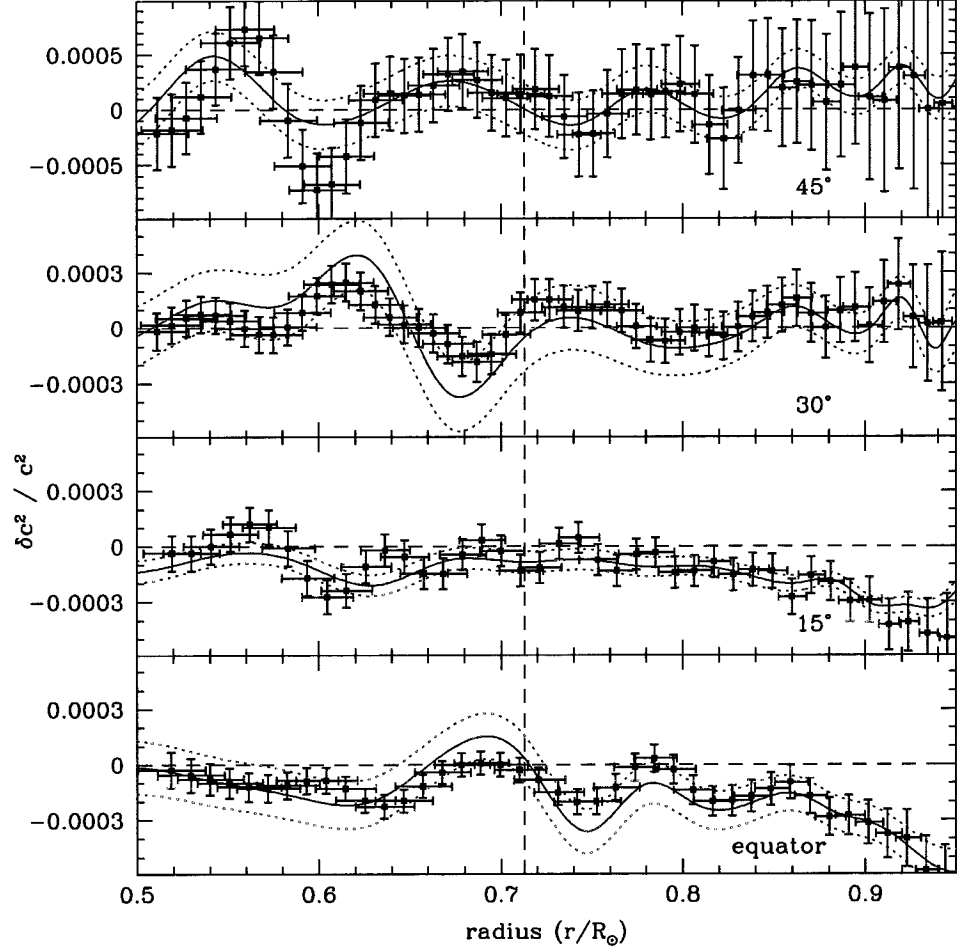


Fig. 3.9.— The inversions of the latitudinal frequencies are shown for four different latitudes from the equator to 45° . The differences are with respect to MDI set #1216. As expected from an examination of the raw frequencies, there are no discernible features in the inversion for 45° and above — the inversions are extremely unstable to the choice of inversion parameters. At 15° and the equator, a significant (about 2σ) enhancement in sound speed at high activity is observed above approximately $r = 0.98R_{\odot}$. As before, the vertical dashed line indicates the position of the base of the convection zone ($r = 0.713R_{\odot}$).

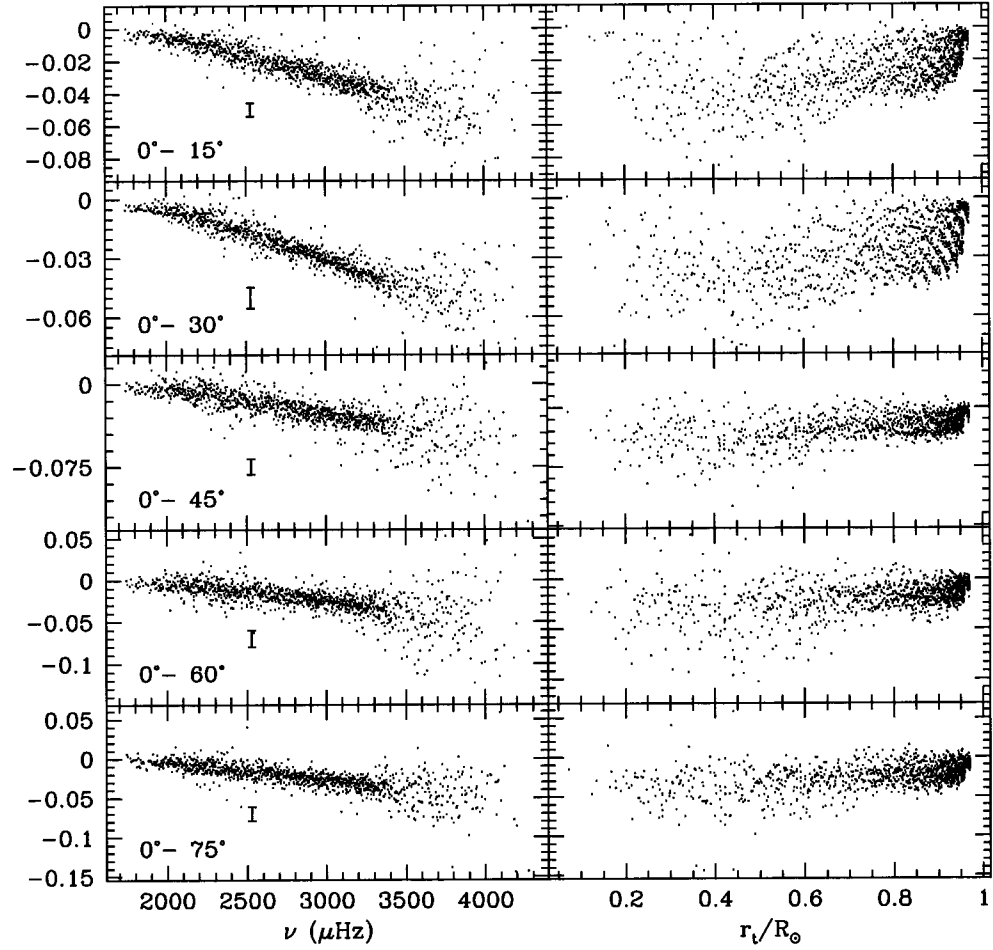


Fig. 3.10.— The $\vec{\xi}_1$ eigenvectors for the asphericity terms — equator minus latitude — are shown for five different latitudes. As usual, the left panels show the eigenvectors with respect to frequency, and the right hand panels are with respect to lower turning point.

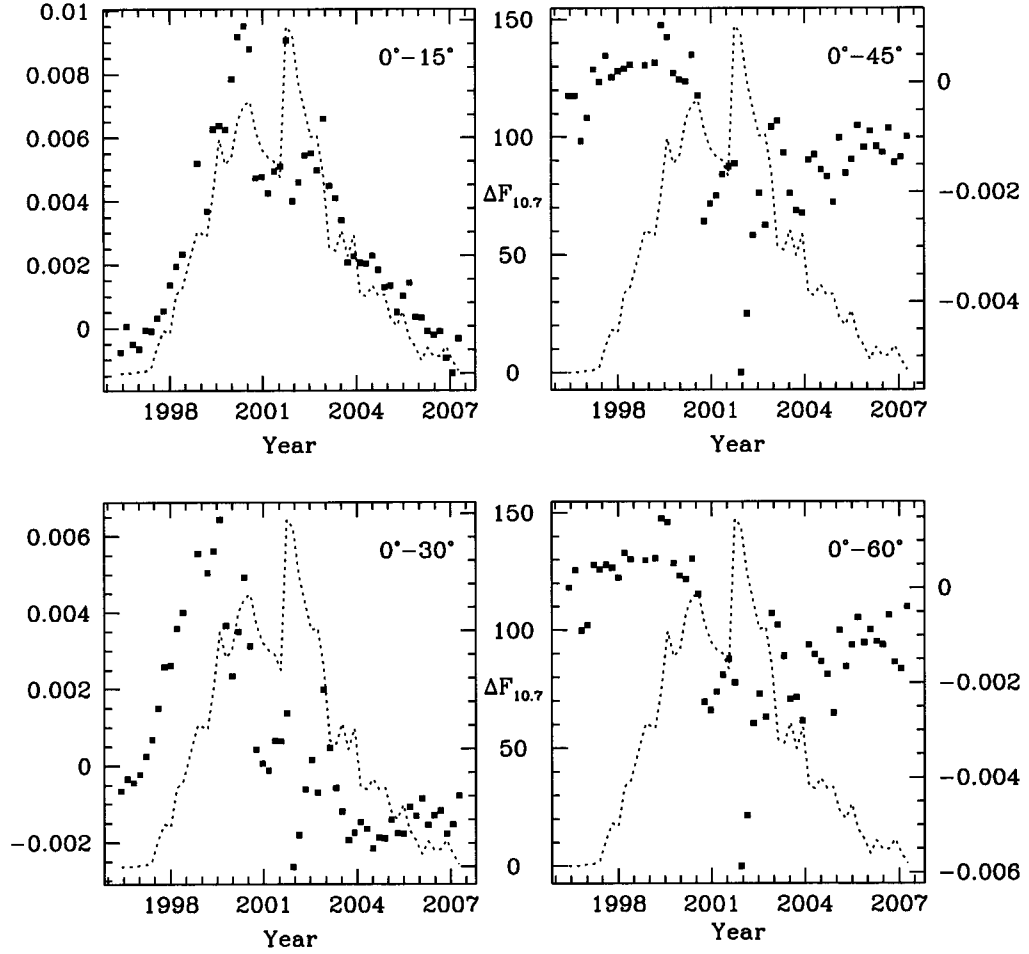


Fig. 3.11.— The scaling coefficients for the asphericity eigenvectors are shown. The dotted line is the $F_{10.7}$ flux. The $0^\circ - 15^\circ$ and $0^\circ - 30^\circ$ both show a phase shift, consistent with the butterfly diagram from Fig. 3.8. The higher latitudes show a distinct change from mostly positive to negative at high activity.

3.4 Conclusions

We have analyzed the changes in solar oscillation frequencies over the course of solar cycle 23. In order to reduce the effects of measurement errors and detect the faintest signatures of solar variability possible, we have employed a Principal Component Analysis of the frequencies. The mean frequencies are known to vary over the solar cycle, and this variation is known to be tightly correlated with surface activity. We have found this correlation as well.

In addition to the frequency dependent change which these earlier authors have detected, we have found a small but statistically significant change in modes with turning points at or below the convection zone. This confirms the result of Chou & Serebryanskiy (2005). This signature is present in both the MDI and the GONG data sets. We have inverted these results to obtain the difference in sound speed, and we have confirmed that there is a change in solar structure at the base of the convection zone over the course of the solar cycle. The measured change at a radius of $r = (0.712^{+0.0097}_{-0.0029})R_{\odot}$ is $\delta c^2/c^2 = (7.23 \pm 2.08) \times 10^{-5}$, where the errors in radius are a measure of the resolution of the inversion taken from the first and third quartile points of the inversion kernel.

We have also used the splitting coefficients to investigate how the changes in structure vary over latitude. We have found that the changes in the solar interior are tightly correlated with the latitudinal distribution of surface activity. The most statistically significant changes detected in the analysis are changes in sound speed in the outer fifteen percent (by radius) of the solar interior.

Chapter 4

Solar Magnetic Field Signatures in Helioseismic Splitting Coefficients

This chapter is adapted from the paper of the same title originally published in the Astrophysical Journal as Baldner, C. S., Antia, H. M., Basu, S., & Larson T. P., 2009, 705, 1704.

4.1 Introduction

In the previous chapter, we discovered a change in the structure of the convection zone which we argued was related to solar activity. Since solar activity is fundamentally magnetic in nature, the natural next question is what magnetic fields could be responsible for this change? In this chapter, we use helioseismology to study the global scale internal magnetic fields over the course of solar cycle 23. We do this by directly computing the effects of various axisymmetric magnetic fields

on the helioseismic splitting coefficients.

Helioseismology is the most powerful tool available to solar physicists to study the interior of the Sun. The oscillation frequencies have been used to study the structure and dynamics of the solar interior with great precision. Magnetic fields, however, have proved to be much more challenging. There are a number of important difficulties in dealing with magnetic fields in a helioseismic context. The magnitudes of the signatures in the data are quite small, making statistically significant measurements challenging. Secondly, the interpretation of data is very difficult. The physics of wave propagation in the presence of magnetic fields is far more complex than in the non-magnetic case. Further, the geometry of the underlying field strongly affects the signatures in helioseismic global mode frequencies, meaning different field configurations and strengths can be difficult to distinguish from their helioseismic signatures. Even worse, Zweibel & Gough (1995) showed that because magnetic fields act on mode frequencies both by perturbing the thermal structure of the Sun and by changing the wave propagation speeds directly, there is a degeneracy between magnetic field effects and other thermal perturbations which cannot be distinguished a priori from helioseismic data.

In this work, we exploit the fact that we have much more helioseismic data than previous investigators had access to, and try to get a coherent picture of sub-surface solar magnetic fields and their temporal evolution. We extend the work of Antia et al. (2000), who considered toroidal magnetic fields, to include poloidal fields. This means that we can, in principle, consider any axisymmetric magnetic field configuration. We compute the effects of a wide variety of magnetic field configurations on the a_2 splitting coefficients, and compare them to a solar cycle's worth of MDI data. It is not clear if the solar magnetic field has large scale structure of the form we assume or whether it is in a tangled state due to

turbulence in the convection zone. Since the effect of magnetic field manifests itself through a quadratic term in magnetic field, our estimate may also be applicable to tangled field with some degree of approximation.

4.2 Perturbations to solar oscillation frequencies

The frequencies of normal modes of oscillation $\nu_{n\ell m}$ are degenerate in m in the case of a spherically symmetric star. Departures from spherical symmetry lift this degeneracy. When the departures from spherical symmetry are small, as they are in the case of the Sun, the differences in frequency for different values of m will be small, and it is natural therefore to express the normal mode frequencies in terms of the mean frequency of the multiplet $\nu_{n\ell}$ and splitting coefficients a_j :

$$\nu_{n\ell m} = \nu_{n\ell} + \sum_{j=1}^{j_{\max}} a_j(n, \ell) \mathcal{P}_j^{(\ell)}(m). \quad (4.1)$$

As is common in the current literature, the polynomials $\mathcal{P}_j^{(\ell)}(m)$ are the Ritzwoller-Lavelly formulation of the Clebsch-Gordan expansion (Ritzwoller & Lavelly 1991). The odd-order splitting coefficients are caused by the rotation of the Sun, and will not be directly considered in this work. The even-order coefficients are caused by second order effects of rotation, and by the effects of magnetic fields or any other departure from spherical symmetry in the solar structure. In this work, we treat rotation and magnetic fields as perturbations on the spherically symmetric case, which allows us to avoid explicitly constructing a model of a rotating, magnetized star. The formalism was developed by Gough & Thompson (1990) and Antia et al. (2000) extended the formalism to include the perturbation to the gravitational potential (i.e., to relax the Cowling approximation) and to include differential

rotation.

The first order correction to the mode frequencies due to rotation affects only the odd-order splitting coefficients. These effects are due to the perturbation of the mode frequencies by advection of the waves. The second order correction affects only the even-order splitting coefficients, and is caused by the perturbation to the eigenfunctions and the centrifugal force. The odd-order coefficients can be used to determine the rotation profile $\Omega(r)$ (Thompson et al. 1996; Schou et al. 1998), which can in turn be used to compute the second order rotation correction (Antia et al. 2000) to the even-order coefficients. This correction needs to be made if the magnetic perturbation is comparable in size to second order rotation effect, which appears to be the case (Gough & Thompson 1990; Antia et al. 2000).

In this work, we consider two different axisymmetric magnetic field configurations: toroidal and poloidal. Following Gough & Thompson (1990), the toroidal field is expressed in the form

$$\mathbf{B} = \left[0, 0, a(r) \frac{d}{d\theta} P_k(\cos \theta) \right], \quad (4.2)$$

where P_k are the Legendre polynomials of degree k and $a(r)$ describes the radial profile of the magnetic field. We consider only even values of k to ensure antisymmetry about the equator, consistent with the observed field at the surface. The poloidal field is assumed to be of the form

$$\mathbf{B} = \left[k(k+1) \frac{b(r)}{r^2} P_k(\cos \theta), \frac{1}{r} \frac{db}{dr} \frac{d}{d\theta} P_k(\cos \theta), 0 \right], \quad (4.3)$$

where $b(r)$ describes the radial profile of the magnetic field. In this case we use only odd values of k to ensure that the field is antisymmetric about the equator. With appropriate combinations of these two fields we can, in principal, represent

any axisymmetric magnetic field.

The effect of these magnetic field configurations on the frequency splittings of p -modes is calculated using the formulation of Gough & Thompson (1990); Antia et al. (2000). There are two ways in which the magnetic field can affect the frequencies, one is the so-called direct effect due to the additional force, and the second is the distortion effect due to the equilibrium state being distorted from the original spherically symmetric one. Both these effects are included in all calculations. These formulations treat the effect of these magnetic fields separately. Unfortunately, the effect of magnetic fields is not linear and hence strictly the contributions from two different configurations cannot be added. In principle, there will be some cross-terms when the combination of toroidal and poloidal fields have a region of overlap in the solar interior. In this work, we neglect these terms and add the contributions from toroidal and poloidal fields to get the total effect. We expect the cross terms to be small.

4.3 Data

The data we use for comparison are 72-day mode parameter sets from the Michelson Doppler Imager (MDI) on the SOlar and Heliospheric Observatory (SOHO). We use mode parameter sets from the corrected pipeline described by Larson & Schou (2008). The original MDI analysis pipeline (Schou 1999) did not take into account a number of instrumental effects which introduced secular trends in the mode parameter sets. In particular, the plate scale of the MDI instrument has changed somewhat over SOHO's mission, and this results in an apparent change in the solar radius if not properly corrected in the analysis. Baldner & Basu (2008) found a signature in the mean frequencies which became increasingly significant

over the course of the solar cycle. A repetition of that work with reanalyzed mode parameter sets removed this effect completely (Baldner et al. 2009). The splitting coefficients, which we focus on in this work, suffer from similar instrumental effects as the mean frequencies, and hence we use the reanalyzed data in this work.

We include 56 mode sets which cover solar cycle 23. The mode sets are identified by the MDI start day, beginning with set #1216 (start day 1 May 1996), and ending with set #5320 (start day 27 July 2007). The coverage begins and ends at low activity, with a 10.7 cm radio flux of 72.7 SFU for the first set and a flux of 69.1 SFU for the last set. The highest activity set, #3160 (start day 27 August 2001), has a 10.7 cm flux of 223.9 SFU.

We fit only the a_2 splitting coefficients, as the higher order splitting coefficients have larger errors, and as such did not distinguish well between different field configurations. The rotation profile determined from the odd-order splitting coefficients (Antia et al. 2008) was used to calculate the second-order contribution to the even-order coefficients, and this contribution was subtracted from the data.

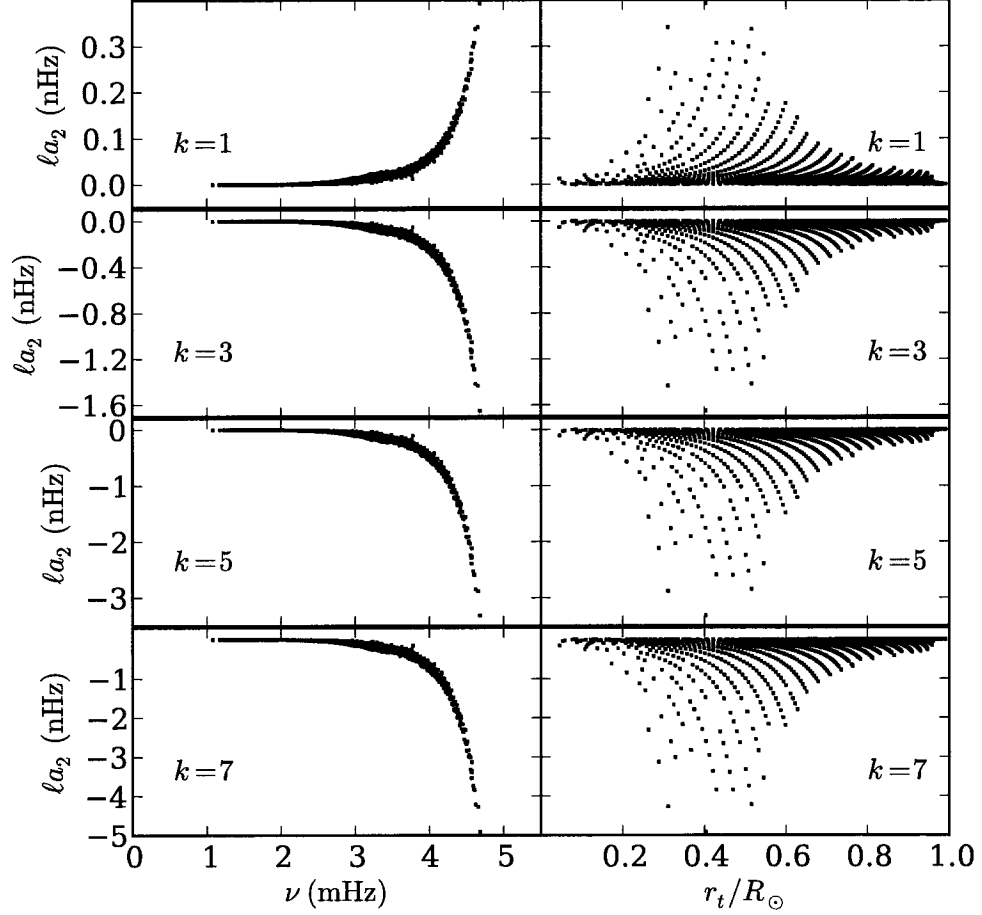


Fig. 4.1.— Splitting coefficients ℓa_2 due to poloidal magnetic fields. The left hand panels are shown as a function of frequency ν , the right hand panels are shown as a function of lower turning radius r_t . The four configurations shown have peak field strengths of 1 G at the surface. The fields have four different values of k . To facilitate direct comparison with later figures, only modes measured in the MDI data (specifically, the high activity set #3160) are plotted.

4.4 Results

4.4.1 Models

In Fig. 4.1, we show the second splitting coefficient for four different poloidal field configurations. The actual quantities plotted are ℓa_2 , both as a function of frequency ν and as a function of the lower turning radius of the modes, r_t . The radial profile in this case is taken to be

$$b(r) = B_0 r^{-k}, \quad (4.4)$$

where B_0 is a constant which determines the peak field strength and r is the radial distance measured in units of solar radius. The models shown in Fig. 4.1 all have a peak strength of $B = 1$ G (note that they do not all have the same value of B_0). The most obvious difference between different order poloidal fields is that for the $k = 1$ field the splitting coefficients are all positive, whereas for the higher order fields they are largely negative, although the shallow modes have positive a_2 .

The toroidal field we employ is similar to that used by Antia et al. (2000), with a radial profile given by

$$a(r) = \begin{cases} \sqrt{8\pi p \beta_0} \left(1 - \left(\frac{r-r_0}{d_0}\right)^2\right) & \text{if } |r - r_0| \leq d_0 \\ 0 & \text{otherwise} \end{cases} \quad (4.5)$$

where p is the gas pressure, β_0 is the ratio of the magnetic to gas pressure at r_0 , and r_0 and d_0 are position and width of the field. As is the case for the poloidal fields, the toroidal field corrections are linear in magnetic field strength squared. Excepting field strength, therefore, our toroidal fields are described by three quantities: the order of the Legendre polynomial k , which determines the

latitudinal distribution of the field, the central radius r_0 , which determines the location, and the width d_0 . Figure 4.2 shows the splitting coefficients due to toroidal fields with different values of k but the same radial profile (in this case, $\beta_0 = 10^{-4}$, $r_0 = 0.999R_\odot$ and $d_0 = 0.001R_\odot$). For the a_2 coefficient, the order k of the field makes very little difference except to the scale of the perturbation — increasing k for the same β_0 effectively increases the total amount of flux, but except for this effect, the a_2 coefficients are not sensitive to different latitudinal distributions. For the remainder of the work, therefore, we restrict ourselves to $k = 2$ fields.

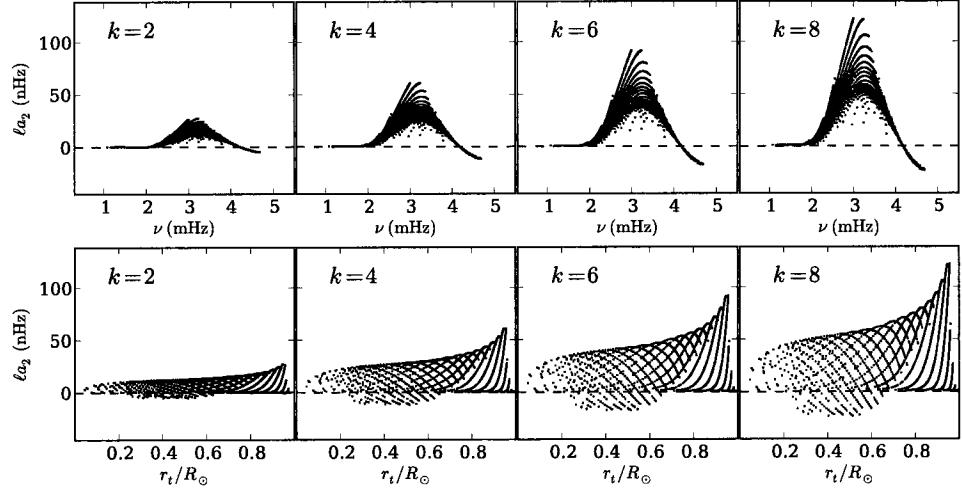


Fig. 4.2.— Splitting coefficients ℓa_2 due to toroidal field with different latitudinal distributions. The upper panels show the coefficients as a function of frequency ν , the lower panels show the coefficients as a function of lower turning radius r_t . All the results are with $\beta_0 = 10^{-4}$, $r_0 = 0.999R_\odot$ and $d_0 = 0.001R_\odot$. Only modes present in the MDI data have been plotted.

Figure 4.3 shows the splitting coefficients ℓa_2 for near-surface toroidal fields with different central radii r_0 and widths d_0 as a function of frequency. Figure 4.4 shows the same, but as a function of the lower turning radius, r_t . The behavior of the splitting coefficients is not surprising. In general, the fields which penetrate

below the surface show oscillatory behavior as a function of frequency similar to that seen in mode frequency (Gough 1990; Gough & Thompson 1990) and used by Roxburgh & Vorontsov (1994); Basu et al. (1994) and others to study the convection zone base. The period of these oscillations is related to the acoustic depth of the perturbation in the structure. Decreasing the depth of the perturbation lengthens the period of the oscillatory behavior. Fields which are confined near the surface, on the other hand, do not exhibit oscillatory behavior, but instead resemble the ‘surface term’ correction which is removed in structure inversions (e.g., Dziembowski et al. 1990; Antia & Basu 1994). Increasing the width of the perturbation smears out the oscillatory signature, as seen in Fig. 4.3. Because all the modes sampled have lower turning radii below the magnetic fields considered here, there are no obvious signatures in the splitting coefficients as a function of r_t .

In addition to fields near the surface, in Fig. 4.5, we show the splitting coefficients due to some toroidal fields located at the base of the convection zone. The fields shown differ only in the width d_0 of the fields. Unlike the surface fields shown in previous figures, the deep field signatures show both positive and negative splitting coefficients. These models are most interesting as a function of lower turning radius r_t . The splitting coefficients are positive above the center of the magnetic field, and negative below the center of the magnetic field. Further, as the width of the field is increased, the width of the perturbations to the splitting coefficients (when plotted against r_t) increases as well.

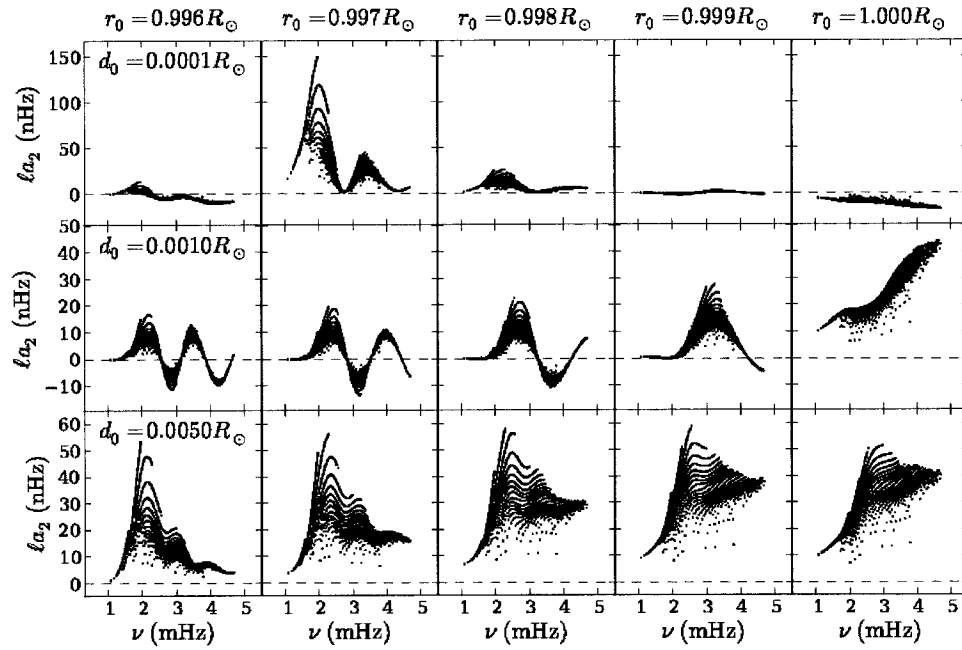


Fig. 4.3.— Splitting coefficients $l a_2$ due to near-surface toroidal magnetic fields, as a function of frequency ν . The results are shown for $k = 2$ with five different values of central radius r_0 (from $0.996 R_\odot$ to R_\odot), and three different values of the width of the field d_0 ($0.0001, 0.001$, and 0.005) R_\odot . Only modes present in the MDI data have been plotted.

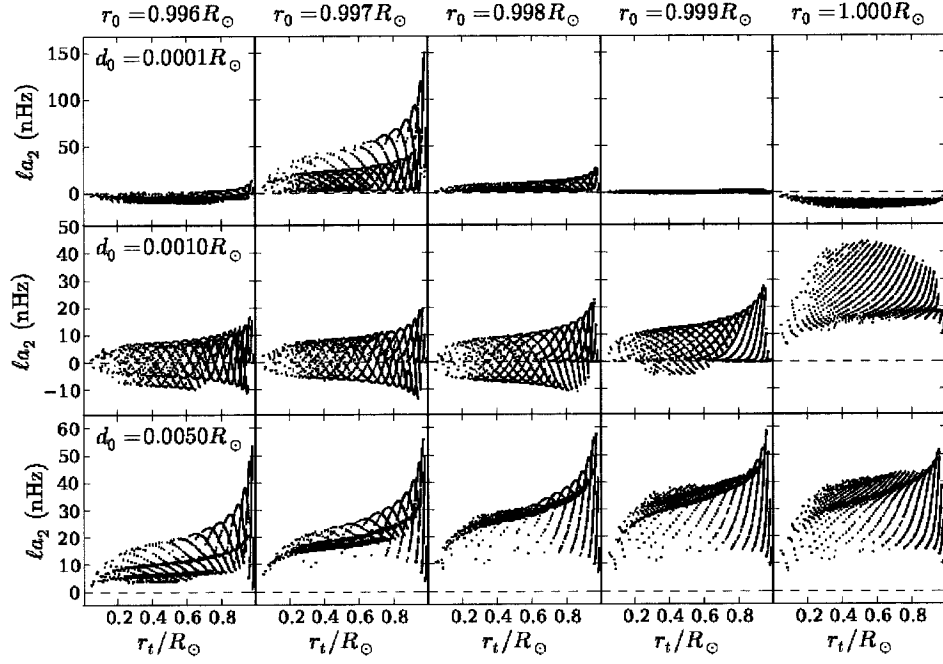


Fig. 4.4.— Same as Fig. 4.3, but plotted as a function of the lower turning radius r_t .

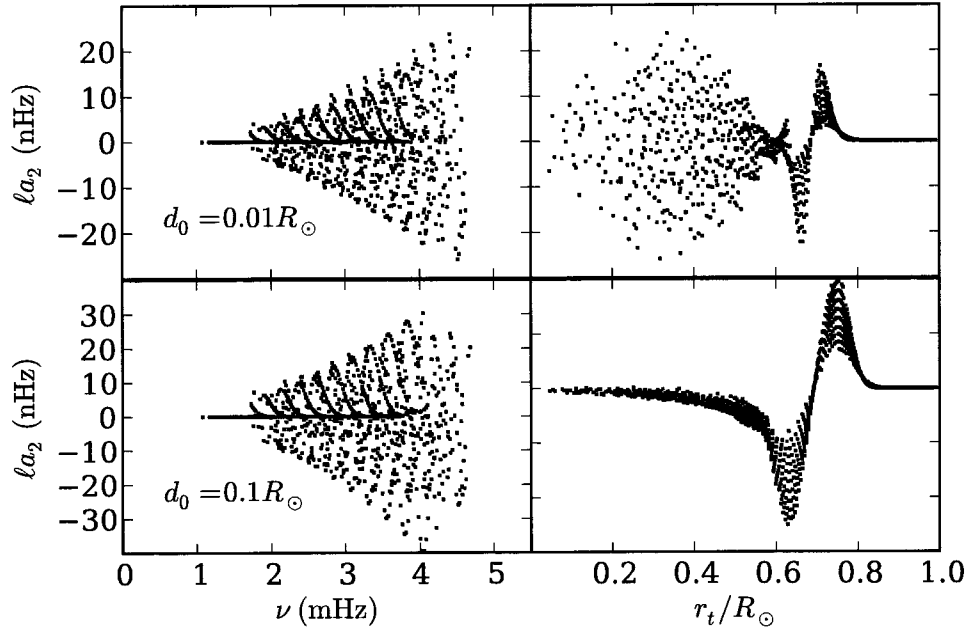


Fig. 4.5.— Effects of toroidal magnetic fields at the base of the convection zone on the ℓa_2 splitting coefficients. Results for two magnetic field configuration with $k = 2$, $r_0 = 0.71R_\odot$ and $\beta_0 = 10^{-4}$ are shown. The fields have widths of $d_0 = 0.01R_\odot$ and $d_0 = 0.1R_\odot$ for the top and bottom panels, respectively. Left hand panels show the splitting coefficients as a function of frequency ν , right hand panels show the splitting coefficients as a function of lower turning radius r_t . Only observed modes have been plotted.

The a_4 splitting coefficients due to various poloidal and toroidal fields are shown in Fig. 4.6, which shows the results for two poloidal fields, the $k = 3$ and $k = 7$ fields, as well as two toroidal fields with different values of k ($k = 2$ and $k = 8$), each with $r_0 = 0.999R_\odot$ and $d_0 = 0.001R_\odot$. The $k = 1$ field has essentially no effect on the a_4 splitting coefficients.

4.4.2 Fits to observed data

In order to choose the fields which best match the actual data, we have computed the splitting coefficients for a large grid of field configurations, with fields through-

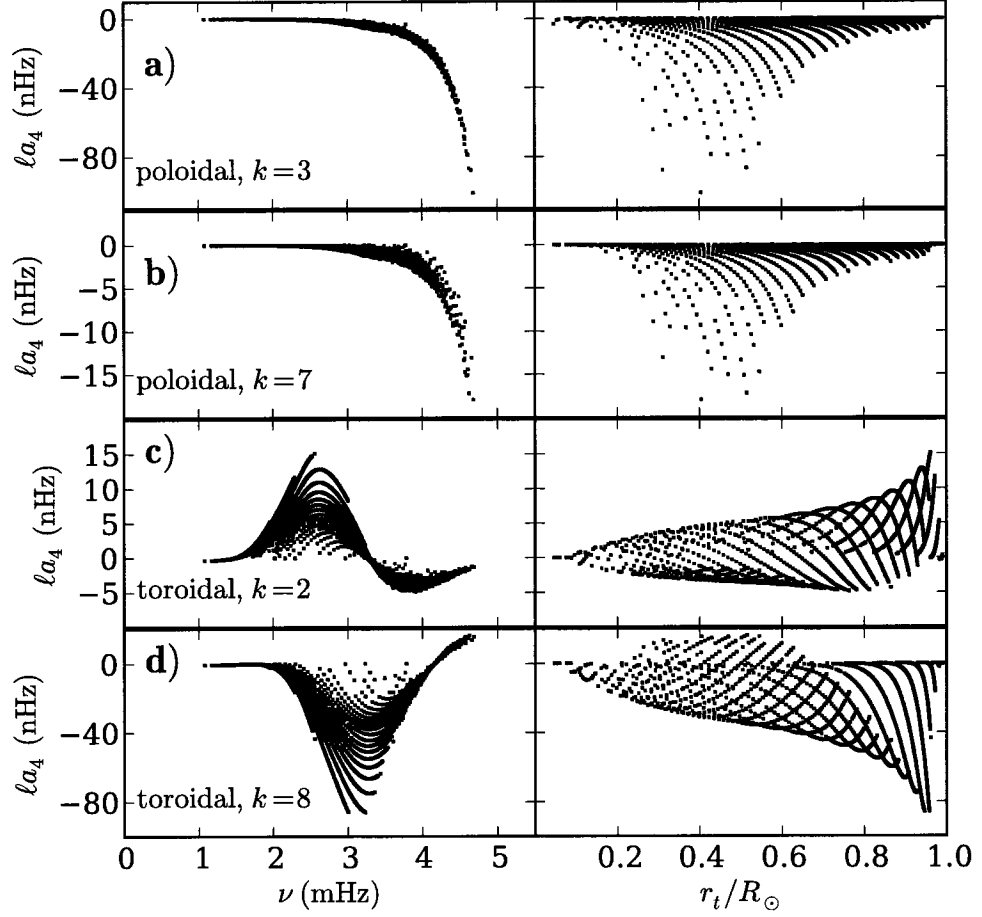


Fig. 4.6.— Effects of various magnetic fields on the ℓa_4 splitting coefficients, as a function of both frequency ν (left hand panels) and lower turning radius r_t (right hand panels). The top two panels show the results for poloidal fields with $k = 3$ (panel a) and $k = 7$ (panel b). The bottom two panels show the results for toroidal fields, both with $\beta_0 = 10^{-4}$, $r_0 = 0.999R_\odot$ and $d_0 = 0.001R_\odot$. Panel (c) is for a $k = 2$ field and panel (d) for a $k = 8$ field. Only observed modes have been plotted.

out the convection zone. For poloidal fields we varied k — the form of the radial profile was found not to matter very much for the splitting coefficients, so long as the field penetrated below the surface. For the toroidal fields, we varied the location r_0 , the width of the field d_0 , and the latitudinal distribution with k . The range in r_0 was between $0.70R_\odot$ and $1.0R_\odot$. The values for d_0 ranged from $10^{-4}R_\odot$ to $0.2R_\odot$. In order to judge goodness-of-fit, we use the χ^2 statistic. For both the poloidal and the toroidal fields, the perturbations vary linearly with the square of the field strength, so to fit the field, we allowed the field strength to vary freely, and chose the strength that minimized the χ^2 . We have computed the χ^2 for all the field configurations in our grid, as well as for many combinations of two and three different fields. The results we present below represent the best fits from the entire grid of computed models.

The largest signal-to-noise ratio in a_2 is found at peak activity, and so the highest activity set ought to be the easiest to fit. Comparison of different field configurations with the splitting coefficients at high activity are shown in Fig. 4.7, and the fits are shown both as a function of frequency and as a function of lower turning radius. The residuals, normalized by the errors in the data, are also shown. A fit to a $k = 1$ poloidal field is shown in panel (a). The reduced χ^2 for this fit is 16, and it is evident that the field does a poor job of reproducing the observed splitting coefficients. Higher order poloidal fields are considerably worse, as an examination of Fig. 4.1 will show — these fields perturb all the splitting coefficients negatively, whereas the observed splittings are all positive. Panel (b) shows the effect of a toroidal field situated near the surface. Although we attempted to fit toroidal fields throughout the convection zone, fields not located very near the surface were extremely poor fits to the data. The field shown in panel (b) is the best fit for a single toroidal field, with $r_0 = 0.999R_\odot$ and $d_0 = 0.001R_\odot$. The reduced χ^2 is 5.

The residuals are mostly without structure in r_t , but are oscillatory in frequency, a hint that there could be a second, somewhat deeper field. The splitting coefficients at peak solar activity cannot be well fit by either a toroidal field or a poloidal field of the form considered by us.

The third field configuration shown (panel c) is a combination of a $k = 1$ poloidal field and a near-surface toroidal field ($r_0 = 0.999R_\odot$, $d_0 = 0.001R_\odot$ — the same field from panel (b)). This combination of fields yields a much better fit to this data set, with a reduced χ^2 of 2.8. Using a surface toroidal field instead of a poloidal field does not fit the data as well, although it is an improvement over the fit in (b), with a χ^2 value of 3.5. Like the toroidal-only fit, the residuals are more or less without structure in r_t , but show oscillatory behavior in frequency. The peak field strengths of the two fields are 133 G and 368 G for the poloidal and toroidal fields, respectively. The residuals from this fit can be fit by a toroidal field centered at $r_0 = 0.996R_\odot$, so in panel (d) we show the best fit to the data: a $k = 1$ poloidal field with two toroidal fields, one centered at $r_0 = 0.999R_\odot$ and another centered at $r_0 = 0.996R_\odot$. Both toroidal fields are $k = 2$ fields and have widths $d_0 = 0.001R_\odot$. The poloidal field has a peak field strength at the surface of 124 ± 18 G, while the toroidal fields have peak field strengths of 380 ± 30 G and 1.4 ± 0.2 kG, respectively. The reduced χ^2 of this fit is 1.7. Attempts to fit the data with a single toroidal field which occupies the same region as the two fields in this fit did not yield a good fit — the data seem to require a double peaked field.

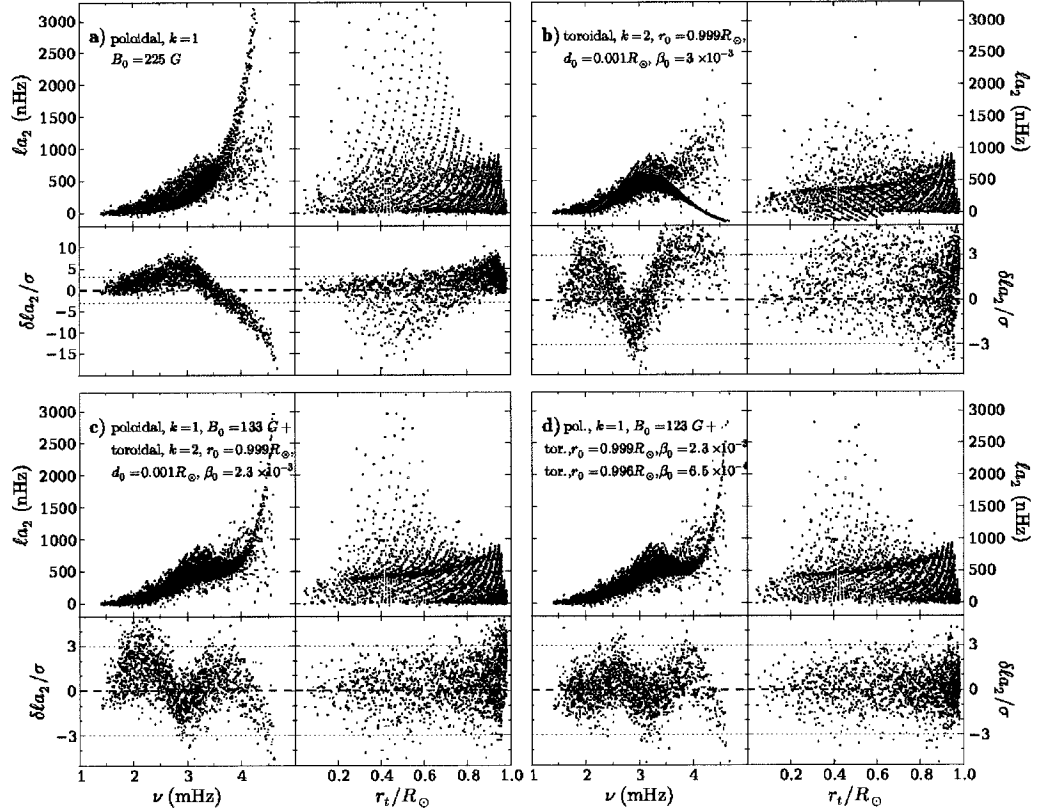


Fig. 4.7.— Fits to observed splitting coefficients ℓa_2 for different magnetic field configurations. Four different fits are shown, both as a function of frequency ν and as a function of lower turning radius r_t . The data are shown in black, and the modeled points in red. The residuals, scaled by the errors in the data, are also shown below the comparisons. The data are the ℓa_2 splitting coefficients from an MDI 72 day mode parameter set, taken at the peak of solar cycle 23 (MDI set #3160, start day 2001 Aug 27). Panel (a) shows a fit from a $k = 1$ poloidal field. Panel (b) shows the fit from a near-surface toroidal field. Panel (c) shows the best fit field combination with two fields to this data set — a combination of a dipole poloidal field with a toroidal field located just below the surface ($r_0 = 0.999R_\odot$, $d_0 = 0.001R_\odot$). Panel (d) shows the best fit with three fields — the same poloidal and toroidal field as in panel (c) (though with slightly different field strengths) and another toroidal field at $r_0 = 0.996R_\odot$ and a width of $d_0 = 0.001R_\odot$.

Figure 4.8 shows the a_4 splitting coefficients for two different data sets (#2224 and #3160), and the same models shown in Fig. 4.7 panel (d). The errors on the data are large compared to the signal — thus the normalized residuals are comparable to those for the a_2 coefficients, but some other field configurations also fit the a_4 coefficients equally well, so we do not use them to constrain the field configurations or determine the field strengths.

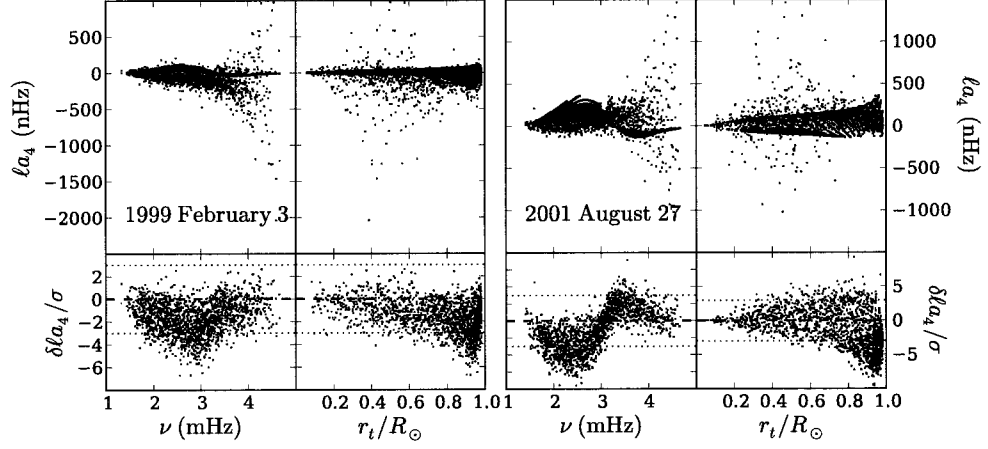


Fig. 4.8.— Comparisons of data to models for $l a_4$ splitting coefficients from two different data sets. The field configurations are the same as from Fig. 4.7 (a). The left hand panels are from set #2224, the right hand panels are from #3160. As in the previous figure, data and model are shown both as a function of frequency ν and as a function of lower turning radius r_t . The residuals are shown below the data, and are normalized by the errors in the data. The model is obtained by fitting only the a_2 coefficients.

Having fit the high activity set, we repeat the fits for all 56 sets in our study. Figure 4.9 shows fits of the same $k = 1$ poloidal plus toroidal field combination to six representative mode sets, covering the rise and fall of solar cycle 23. The first set, #1216, is the first 72-day mode set from the MDI program, and is a low activity set. Two rising phase sets are shown, #2224 and #2728, with 10.7 cm fluxes of 131.4 SFU and 187.3 SFU, respectively. The high activity set from Fig. 4.7 is shown, and a declining phase set (#3952, $F_{10.7} = 126.4$) and a set from the current

minimum (#4744). For all sets, the same combination of poloidal and toroidal fields — but with differing field strengths — was found to be the best fit. The residuals show the same structure with frequency.

No mode set in our study is well fit by any magnetic field at the base of the convection zone. For low activity sets (10.7 cm flux of less than 100 SFU), we can find an upper bound on the field that could be present in the data. For a field centered at the base of the convection zone with $k = 2$ and $d_0 = 0.01R_\odot$, we find that fields of up to 300 kG can be fit to the data, although this is an upper limit, not a detection, since the models of that field strength or lower give the same χ^2 as a zero field strength model. At high activity, the dominant signal is from the surface, which we have attempted to explain with magnetic fields located in those layers.

The field strengths of the poloidal and shallow toroidal field fits to all 56 sets used in this study are shown in Fig. 4.10. Also shown in this figure is the ratio of the poloidal field strength to the $r_0 = 0.999R_\odot$ toroidal field strength. With the exception of the low activity sets at the beginning and end of the solar cycle, where the uncertainty in the fits is relatively large, the ratio between the poloidal and toroidal field strengths is roughly constant. The field strengths from Fig. 4.10 are correlated with global activity indices from solar cycle 23. The correlation coefficients are 0.90, 0.93, and 0.92 for the poloidal and two toroidal field components, respectively. In Fig. 4.11, we plot the toroidal and poloidal field strengths as a function of one such global index, the 10.7 cm radio flux. The field strengths prove to be highly correlated with activity, although there is a hysteresis-like effect evident in the toroidal field strengths — the rising phase (shown in blue) is weaker than the declining phase fields. The same effect may also be present at low activity in the poloidal field strengths. The poloidal field strengths do seem to saturate at

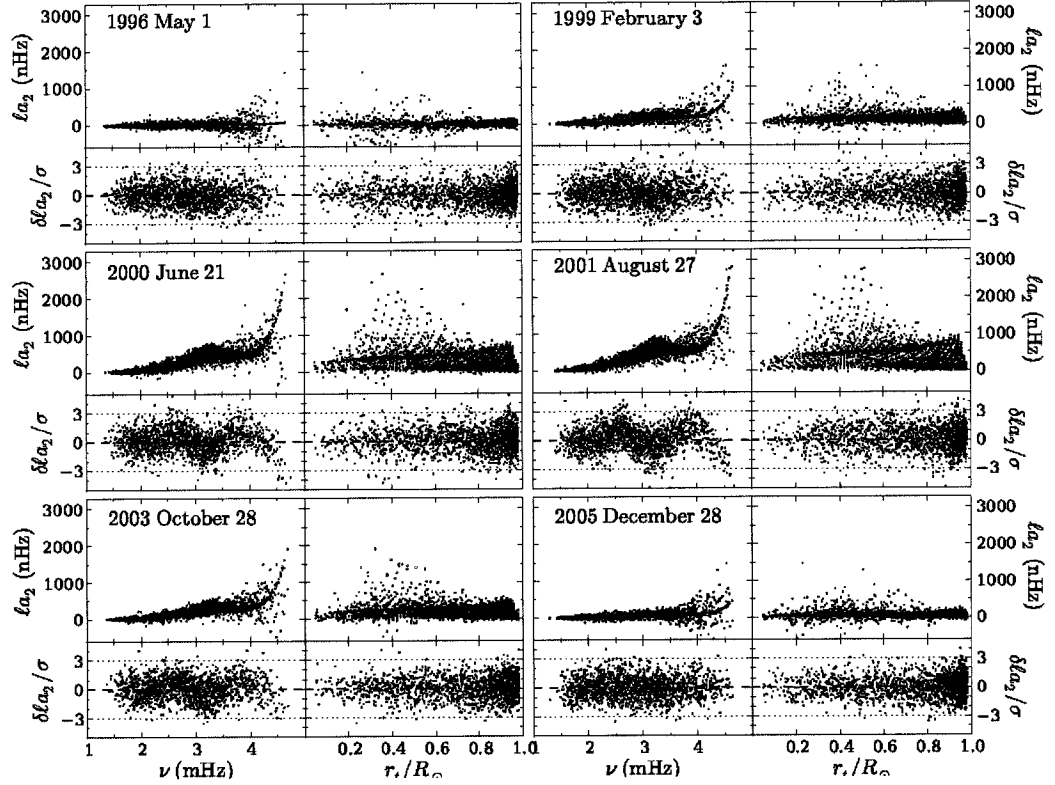


Fig. 4.9.— Fits to measured splitting coefficients ℓa_2 for six different sets through solar cycle 23. The data (shown in black) are from MDI 72 day mode parameter sets. The magnetic field configuration is the same as panel **d** in Figure 4.7: a dipole poloidal field and two toroidal fields at $r_0 = 0.996R_\odot$ and $r_0 = 0.999R_\odot$, with $d_0 = 0.001R_\odot$ and $k = 2$. The fits are shown both as a function of frequency ν and as a function of lower turning radius r_t . The residuals scaled by the errors in the data are also shown. The toroidal field strengths at $r = 0.999R_\odot$ correspond to $\beta_0 = 10^{-4}$, 7.8×10^{-4} , 2×10^{-3} , 2.5×10^{-3} , 1.3×10^{-3} , and 5×10^{-4} for the six sets, respectively. The toroidal field strengths at $r = 0.996R_\odot$ correspond to $\beta_0 = 1.2 \times 10^{-5}$, 2×10^{-4} , 5.6×10^{-4} , 6.6×10^{-4} , 2.9×10^{-4} , and 1.4×10^{-4} . The poloidal field strengths at the surface are $B = 0$ G, 68 G, 115 G, 125 G, 94 G, and 58 G.

high activity. The strengths of the two toroidal fields are extremely well correlated.

4.5 Discussions and conclusions

We have attempted to use the first even order splitting coefficient (a_2) to infer the configuration and strength of the Sun's internal magnetic fields over the course of solar cycle 23, assuming that the entire signature in a_2 after correction for rotation effects is magnetic and that the fields are axisymmetric. The field that we have found is a combination of poloidal field and a double-peaked near-surface toroidal field. The strengths of the poloidal and toroidal components, at least for the high activity period, are well correlated. The relative strengths of the two toroidal fields are also extremely well correlated.

Although the fits we have shown are the best fit to the data from the grid of models that we have computed, we can say nothing about the uniqueness of these fits over the set of all possible magnetic field configurations in the solar interior. In particular, the choice of radial profile of the toroidal fields is virtually limitless, and by restricting our work to profiles of the form (4.2), we have limited our search to a restricted class of fields. It is possible that there are fields we did not consider with quite different radial and latitudinal distributions which fit the data as well as the fields we have presented as best fits. In addition, as noted above, it is not strictly correct to add the splitting coefficient perturbations together as we have done without explicitly accounting for the perturbations arising from the cross terms. We do not expect, however, these corrections to be significant, and a full treatment of these corrections would be considered in a future work.

Our inferred magnetic field does not change its latitudinal distribution over the course of the solar cycle. This is in part due to the fact that we are only fitting

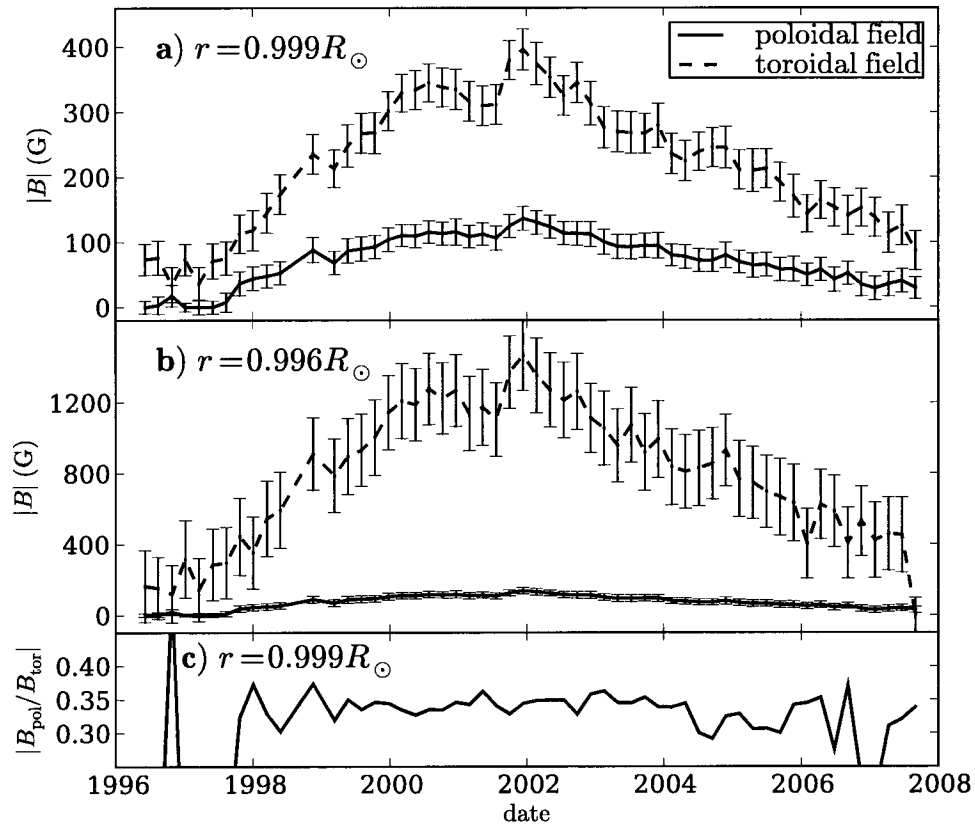


Fig. 4.10.— The strength of the inferred magnetic fields as a function of time over solar cycle 23. Each MDI 72 day mode parameter set is fitted with the same magnetic field configuration as Fig. 4.9. The strengths (in Gauss) of the poloidal field at $r = 0.999 R_{\odot}$ (solid black line) and the toroidal field at $r = 0.999 R_{\odot}$ (dashed line) are shown in the upper panel (a). The middle panel (b) shows the same quantities as in the upper panel, but this time at a radius of $r = 0.996 R_{\odot}$. The lower panel (c) shows the ratio of the poloidal field strength to the toroidal field strength at $r = 0.999 R_{\odot}$. The ratio of poloidal to toroidal at $r = 0.996 R_{\odot}$ looks very similar.

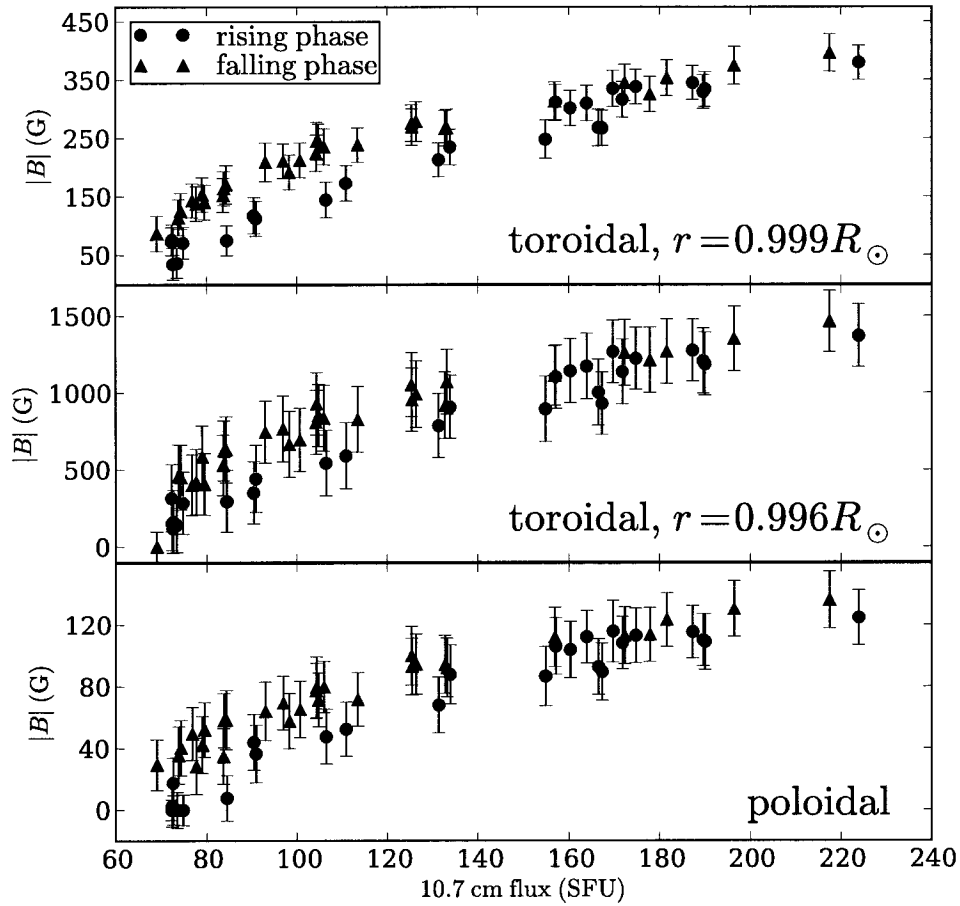


Fig. 4.11.— The strength of the inferred magnetic fields as a function of 10.7 cm radio flux. The top panel shows the $r_0 = 0.999 R_{\odot}$ toroidal field strength, the middle panel shows the $r = 0.996 R_{\odot}$ toroidal field strength, and the bottom panel shows the poloidal field strength at $r = 0.999 R_{\odot}$. Rising and declining phase are distinguished with blue circles for the rising phase and red triangles for the declining phase. The toroidal field shows a hysteresis effect. The poloidal field shows some hysteresis at low activity, as well as a hint of saturation at high activity.

the a_2 coefficient (as noted above, the higher order splittings had large errors), so our sampling of the interior is not really latitudinally sensitive. Thus, we do not see a butterfly diagram in our magnetic fields. Ulrich & Boyden (2005) measured the surface toroidal component of the solar magnetic field over almost an entire 22-year cycle. The field they measure is roughly a tenth of the peak strength of our toroidal field. Strictly speaking, however, we see no toroidal field at all at the surface, since in our inferred field, the field strength becomes zero precisely at $r = 1R_\odot$. The peak strength that we measure, however, is only 700 km below the surface, and the field could penetrate the surface somewhat. Ulrich & Boyden (2005) find a field which gives a $\beta \sim 6 \times 10^{-5}$ at the surface at high activity, and drops to nothing at low activity, while we find a field that changes from $\beta_0 \sim 10^{-4}$ at low activity to $\beta_0 = 2 \times 10^{-3}$ at high activity at a radius of $r = 0.999R_\odot$ (a depth of approximately 700 km).

Recently, attention has been focused on the strength and configuration of the quiet Sun surface magnetic field. Harvey et al. (2007) reported the presence of a ‘seething’ horizontal magnetic field with an rms field strength of 1.7 G. With the launch of Hinode (Solar B), the high spatial resolution of the onboard spectropolarimeter has been used to study the horizontal fields of the solar photosphere. Lites et al. (2007, 2008) have measured the horizontal flux, which they find to be 55 G, compared to the average vertical flux of 11 G. Petrie & Patrikeeva (2009) found that the zonal component (component in the East-West direction) was much smaller than the radial component, reporting an inclination angle of less than 12° from vertical in the East-West direction.

The fields being studied in the aforementioned works are generally very tangled fields which thread through the intergranular lanes and so they are not axisymmetric fields. It is worthwhile to compare our results with theirs, since tangled fields on

local scales can organize into roughly axisymmetric fields on global scales. However, the contribution to splittings are more sensitive to $\langle B^2 \rangle$ rather than $\langle B \rangle^2$ and hence tangled field may also contribute to it, even when the average $\langle B \rangle$ is very small. Further, considering the general behavior of the perturbation to the mode frequencies, our inference about the location of required magnetic field is more robust as a different location will yield a very different behavior of splitting coefficients. The exact magnitude of the field may depend on the assumption of geometry and on it being tangled or large scale. Nevertheless, we believe that our estimate is of the right order, though the statistical error bars obtained by us may not be realistic. The systematic errors in these estimates would be certainly larger. The dominance of poloidal field orientation at the surface found by Petrie & Patrikeeva (2009) is found in our own results — at the surface, the toroidal field is weak or vanishing, but the poloidal field remains. In the period analyzed by Lites et al. (2007, 2008), we find a poloidal field strength of 40 G, and a toroidal field of 90 G at a depth of 700 km. The vertical flux they find (11 G) is weaker than what we detect, but their 55 G horizontal flux may be roughly consistent with our toroidal field.

Schrijver & Liu (2008) found that the dipole moment of the surface magnetic field, measured from MDI magnetograms, was half the strength in 2008 that it was in 1997, during the last solar minimum. We do not see such a difference from the beginning of our period to the end — in fact, we find the poloidal field strength is slightly higher during the current minimum, although the level of the difference is within the errors, and our data sets end in 2007, so the comparison is not contemporaneous.

Hysteresis in the relations between activity indices has been observed before, for example in the relation between low degree (Anguera Gubau et al. 1992; Jimenez-

Reyes et al. 1998) and intermediate degree (Tripathy et al. 2000, 2001) acoustic modes and global magnetic indices. It should be noted that an analysis of a full solar cycle's worth of intermediate degree p -modes data does not show any hysteresis in mean frequencies as a function of 10.7 cm flux (Baldner & Basu 2008). Tripathy et al. (2001) noted that, among the global mode indices, the relation between global line-of-sight magnetic flux and 10.7 cm radio flux showed a hysteresis effect, but the relation between the radiative indices and 10.7 cm flux did not. Moreno-Insertis & Solanki (2000) argued that the observed hysteresis could be almost entirely due to the latitudinal distribution of magnetic flux on the surface of the Sun. We believe that this is a compelling explanation for the hysteresis that we find. The 10.7 cm flux is the integrated flux received at the Earth and does not contain any information about the latitudinal variation, while the a_2 splitting coefficient is associated with definite latitudinal variation, given by $P_2(\cos \theta)$ (Antia et al. 2001a), and hence the two would not be the same. More importantly, we expect the actual magnetic fields in the near surface layers to drift equatorward — as the surface fields do.

Few conclusions can really be drawn from this work with respect to dynamo theory since the fields we have inferred are predominantly shallow fields, whereas most dynamo models operate much deeper down, in the shear layer at and below the base of the convection zone. (some useful recent reviews include Ossendrijver 2003; Charbonneau 2010; Miesch & Toomre 2009). The upper limits that we place on fields at that depth are consistent with earlier helioseismic results (e.g., Basu 1997; Antia et al. 2000; Chou & Serebryanskiy 2002, 2005; Baldner & Basu 2008). Many deep-seated dynamo mechanisms predict an anticorrelation between the poloidal and toroidal field components, as the dynamo converts poloidal to toroidal field and toroidal field back to poloidal. We do not see any evidence of

such conversion. Some dynamo mechanisms, however, operate in the near-surface shear layer (e.g. Brandenburg 2005). Although the fields generated in these models are generally extremely tangled, on global scales these fields can have toroidal and poloidal components (e.g. Brown et al. 2007, 2010). In particular, although they were considering a more rapidly rotating star than the Sun, Brown et al. (2007) noted that their field contained both a poloidal and a toroidal component, and that the toroidal component was much the stronger of the two.

Chapter 5

A Statistical Study of Mode Parameters of Active Regions

A portion of this chapter is adapted from a paper entitled “Evidence for solar frequency dependence on sunspot type”, published in the Astrophysical Journal Letters as Baldner, C. S., Bogart, R. S., & Basu, S., 2011, 733, L5.

5.1 Introduction

We have seen in Chapter 4 that the global mode even-order splitting coefficients can be explained by a strong toroidal field with a weak poloidal component, buried in the very shallowest layers of the solar convection zone. This region is normally inaccessible to global mode analysis — the information contained in these layers is sparse. To detect changes in these layers, we turn to the techniques of local helioseismology, ring diagrams in particular, for further research.

The use of so-called ‘ring diagrams’ (Hill 1988) to study solar structure is by now a well-established technique in helioseismology (see review by Gizon &

Birch 2005). In this paper, we will discuss the changes to mode parameters in ring diagrams between active regions and the surrounding quiet Sun.

Global mode parameters change with the overall level of solar activity; this is by now very well established (see Chapters 3 and 4). The frequencies of both low degree modes (e.g. Chaplin et al. 2007) and medium degree modes (e.g. Dziembowski et al. 1998; Howe et al. 1999b; Dziembowski et al. 2000) increase with solar activity level, and this frequency increase is stronger at higher frequencies. Though high degree global mode measurements are not routinely made, some sets of high degree mode frequency measurements have been made, and these are found to increase with activity as well (Rabello-Soares & Korzennik 2009).

Ring diagrams prove useful for studying the effects of solar activity on helioseismic modes for two reasons. First, rings are measured on a localized patch of the Sun, providing both temporal and spatial resolution. This allows us to isolate phenomena associated with solar activity from the surrounding Sun. Second, measurements can be made to much higher degree much more easily than with global mode analysis. Ring diagrams were first used by Hill (1988) to measure flow rates near the solar surface. Rings have been used subsequently by a number of authors to study the near-surface dynamics of the Sun (e.g. Schou & Bogart 1998; Basu et al. 1999; Haber et al. 1999).

The effects of active regions on ring diagram mode parameters have been studied in previous works. Haber et al. (2000) found that the high degree mode frequencies obtained from ring diagrams were enhanced in active regions. Rajaguru et al. (2001) found that the mode widths were also enhanced in active regions, while the amplitudes were suppressed, and Rabello-Soares et al. (2008) found that the relation between the change in width and mode amplitude was very nearly linear. Howe et al. (2004) assumed that the relation between activity and mode

parameter variation was quadratic, and found a peak increase in mode frequency at around 5mHz, with a corresponding maximum change in width and amplitude.

In this work, we study the properties of 264 active region ring diagrams from solar cycle 23. This sample gives us a statistically significant number of measurements over a substantial range of activity levels from all phases of the solar cycle, when compared to earlier works. In Section 5.2 we describe the statistical sample of active regions and the ring diagrams we use to analyze them. In Section 5.3 we discuss this analysis, studying first the changes in frequencies with magnetic activity, then several other parameters (amplitude, mode width, and asymmetry). In this section, we demonstrate that the shifts in frequency exhibit a dependence on active region classification. In Section 5.4, we discuss the results, compare them to previous results, and speculate on the physical reason for the results that frequency changes depend on active region geometry.

5.2 Analysis

5.2.1 The active region sample

Targets are selected from the list of NOAA active regions. Ring diagrams require higher resolution Dopplergram data than the usual MDI ‘medium- ℓ ’ data that are collected continuously. We use full-disk Dopplergram data which are one of MDI’s ‘high rate’ data products, produced mainly during yearly two to three month dynamics run campaigns. We require a data coverage of greater than 80%. Figure 5.1 shows the distribution of the active region targets in latitude and Carrington coordinate. The clumping due to the limited data availability is obvious.

Ring diagrams suffer from a number of systematic effects. These arise primarily from foreshortening effects when away from disk center, and secular changes in the

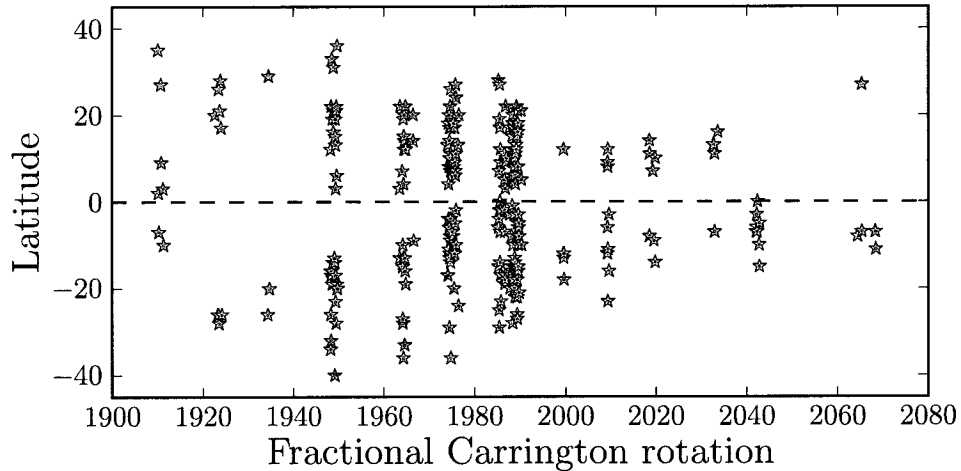


Fig. 5.1.— Distribution of the active region sample in solar coordinates. The clustering is due to limited high rate data availability from the MDI instrument.

characteristics of the MDI instrument. These effects can be minimized by studying the mode parameters in an active region relative to a quiet Sun region, tracked at the same latitude and as near in time as possible. For this sample, two quiet regions were chosen for each active region, one on either side of the active region. For the analysis, however, only one comparison region is used. In general, the comparison region with the smaller MAI is chosen, though in some cases various problems with the data prompt us to use the other. The entire sample, with coordinates for both the active and the chosen comparison region, is shown in Table B.1, which can be found in Appendix B.

5.2.2 The ring diagrams

The data are resolved line-of-sight velocity measurements of the solar surface taken by the Michelson Doppler Imager (MDI) on board the *Solar and Heliospheric Observatory* (SOHO) spacecraft. Ring diagrams are constructed from small, $16^\circ \times 16^\circ$ patches of the solar disk, tracked at the Snodgrass rate for the latitude of the center

of the aperture. The regions are tracked across the solar disk center. The cadence of observation is 1 minute, and the patches are tracked for 8192 minutes. They are projected on to a rectangular grid using Postel's projection and corrected for the distortion in the MDI optics. The Doppler cubes are then Fourier transformed to obtain a three dimensional power spectrum. A more detailed discussion of the construction of ring diagrams can be found in Patron et al. (1997) and Basu et al. (1999).

The spectra are fit in the same way as Basu et al. (2004). The functional form is from Basu et al. (1999):

$$P(k_x, k_y, \nu) = \frac{e^{B_1}}{k^3} + \frac{e^{B_2}}{k^4} + \frac{\exp [A_0 + (k - k_0)A_1 + A_2(k_x/k)^2 + A_3(k_x k_y/k)^2] S_x}{x^2 + 1}, \quad (5.1)$$

where

$$x = \frac{\nu c k^p - U_x k_x - U_y k_y}{w_0 + w_1(k - k_0)}, \quad (5.2)$$

$$S_x = S^2 + (1 + Sx)^2. \quad (5.3)$$

The 13 parameters are fit to each ridge independently using a maximum likelihood method. Although the dispersion relation fit is of the form $\nu = ck^p$, each slice in frequency is fit independently. The degree ℓ fit using this method need not be an integer, so for analysis the ring fits are interpolated to integer ℓ .

5.2.3 The magnetic activity index

In order to characterize the level of activity in our rings, we use a measure of the total unsigned line-of-sight magnetic flux. This measure is the Magnetic Activity Index (MAI), which is described in Basu et al. (2004) and is a measure of the strong magnetic unsigned flux in the ring diagram aperture. In brief, the MAI is

the spatial and temporal average of all MDI magnetogram pixels with a flux greater than 50G, taken over the same aperture and time range as the velocity data for the ring diagrams. The activity in each region, then, is characterized by a single number, and differential measurements can be characterized by the difference in MAI, ΔMAI , between the active region and the quiet comparison region. We also fit a linear trend in time to the spatial averages of the magnetograms. This gives a rough measure of the growth or decay of the active region, and we refer to this quantity as the growth parameter. Pixels are compared to the average of their neighbors: when this average is greater than 400 G, the pixel is rejected if it differs from this average by more than a factor of 6. These outliers are generally cosmic ray hits, and are relatively uncommon.

5.3 Results

5.3.1 Changes in frequency

Mode parameters for all rings and comparison regions were fit using the profile from equation (5.1). We interpolate the ridge fits to integer values of ℓ , and take the differences in frequency $\delta\nu$. The sense of the differences is active minus quiet. Examples of parameter differences for one active region are shown in Figure 5.2. In Figure 5.3, we show averages of the scaled frequency differences $\langle \delta\nu/\nu \rangle$ for the f -mode and the first three p -modes. The frequency ranges chosen have relatively small errors and were fit in most regions in the sample. The behavior seen in Figure 5.3 is nevertheless representative of the rest of the data in our sample. The majority of ΔMAI values are fairly small — this is in part due to the fact that the majority of active regions do not have particularly large MAI values, but also due to the fact that, at high activity levels in particular, it is sometimes difficult

to find a suitable quiet region for comparison. The comparison regions therefore sometimes have fairly significant MAI values — in some cases as high as 50 G.

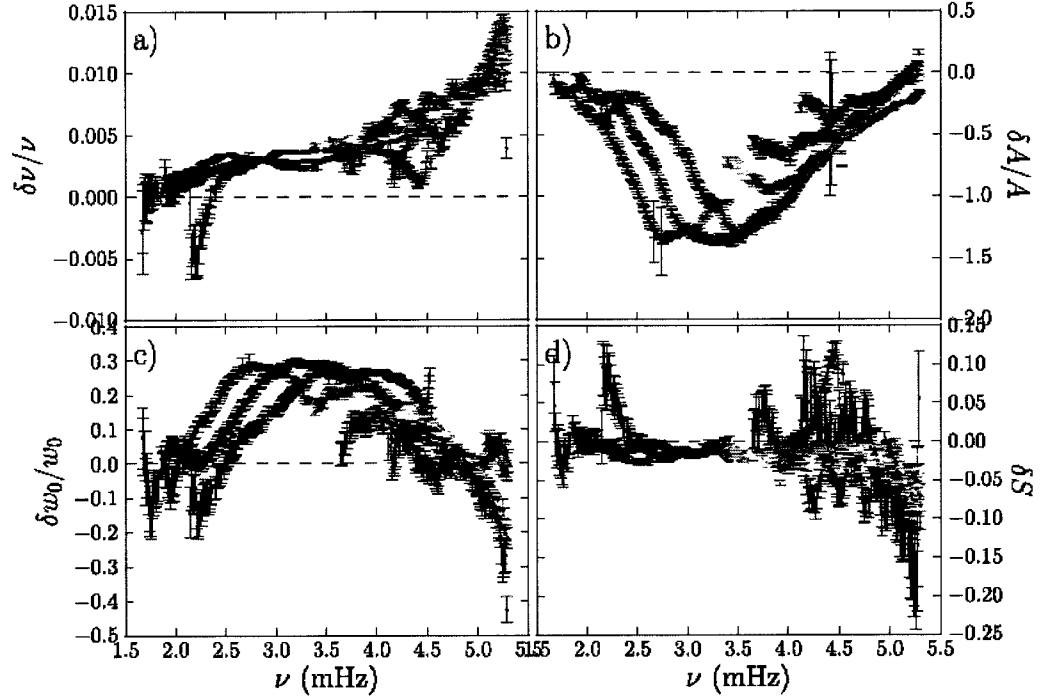


Fig. 5.2.— An example of the differences in ring diagram parameters between an active region and a quiet comparison region. Shown are the differences in frequency ν (panel a), amplitude A (panel b), width w_0 (panel c) and mode asymmetry (panel d). The region shown is AR9017 with $\Delta\text{MAI} = 198.72$ G. In all panels, different radial orders n are plotted in different colors.

We confirm earlier results finding that, in the presence of magnetic fields, helioseismic frequencies increase. We find that, for small and intermediate magnetic field strengths ($\Delta\text{MAI} \lesssim 200$ G), the relationship is linear. For the p -mode differences, the Pearson correlation coefficients (that is, of the frequency differences with respect to ΔMAI) mostly range between 0.6 and 0.7. The f -mode frequencies have larger errors, and the correlation coefficients are correspondingly lower. The best fit linear regression lines are also shown. The reduced χ^2 values computed

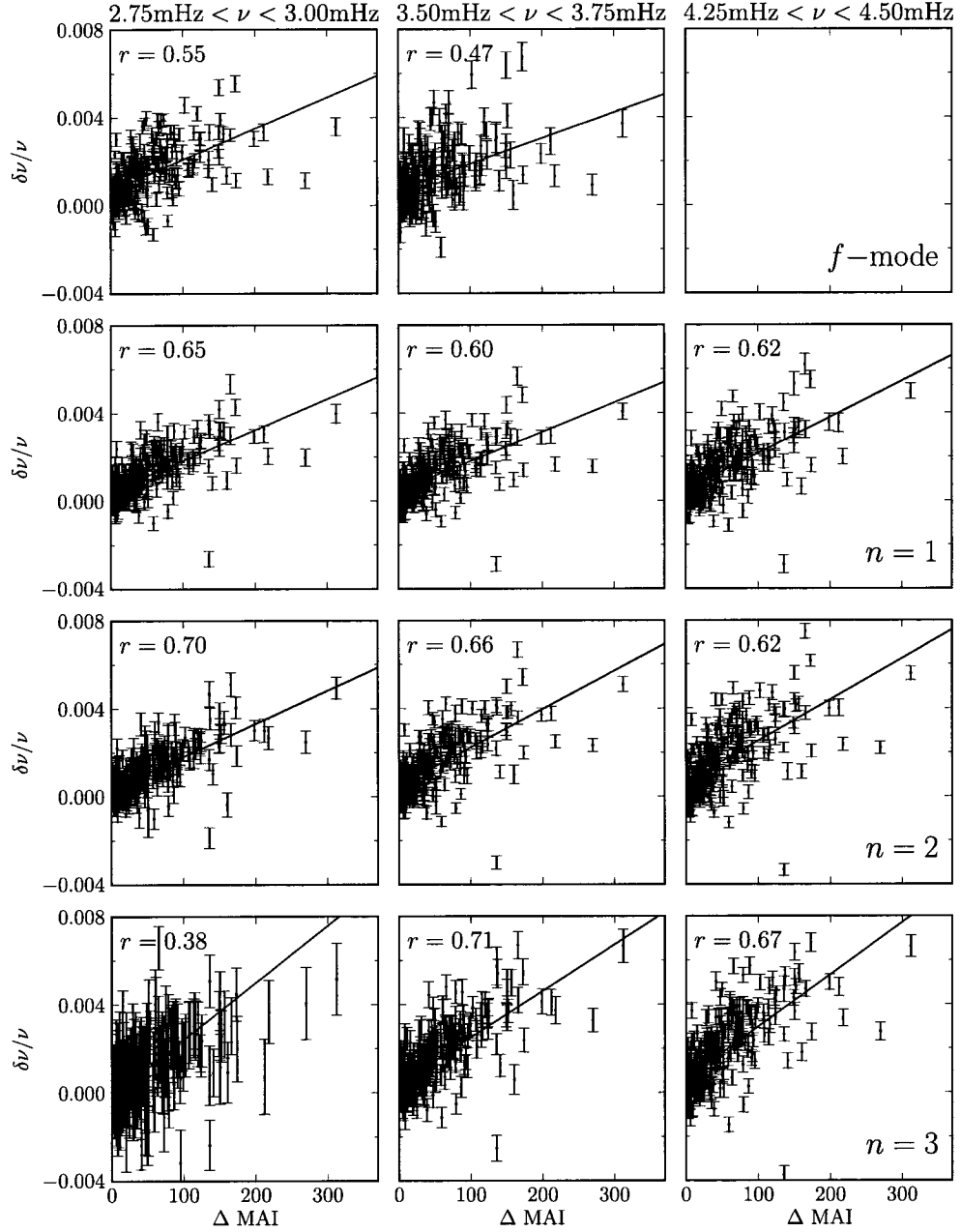


Fig. 5.3.— Averaged frequency differences in three different frequency bins are shown for the f -mode and first three p -modes, as a function of the difference in MAI. The differences are with respect to a quiet region near the active region. The Pearson correlation coefficient r is shown in each panel. The top right panel is blank because the f -mode does not extend that high in frequency.

from the residuals are large — between 3 and 15 for sets of averages. Thus, the computed errors in the fitted frequencies do not completely account for the observed scatter in the frequency differences. It is possible that a linear relation does not completely account for the dependence of frequency on ΔMAI , but we have tested a variety of higher order polynomials and other functional forms without substantially reducing the χ^2 values. When fitting higher order polynomials, the best fits return essentially the same linear fits as shown in Figure 5.3, with negligibly small non-linear coefficients. Other functional forms generally increased the χ^2 values.

As a test of the assumption of linearity, we apply an Anderson-Darling test to the residuals from the linear best fits. The residuals from the linear regression fit fail an Anderson-Darling test at the 1% level. This implies either that the errors are non-gaussian, or that the relation between magnetic activity and shift in frequency is not entirely linear.

At high magnetic field strengths ($\Delta \text{MAI} \gtrsim 200 \text{ G}$), a visual inspection of Figure 5.3 might suggest a ‘saturation’ effect in the frequency shifts. Evidence for such an effect in thermodynamic perturbations beneath active regions has been suggested (Basu et al. 2004; Bogart et al. 2008). In this case, however, we do not find that the outliers at high field strengths are statistically significant. Fitting different slopes at low and high activity does not change the χ^2 values of the residuals, and removing the high activity regions from the sample does not substantially change either the χ^2 values or the Anderson-Darling A^2 statistic of the residuals. Further, we have tested whether or not the presence of some comparison regions with significant activity is introducing bias. We find that, when the sample is divided between quiet and moderately active comparison regions, the frequency differences are indistinguishable. It must be noted, however, that a saturation

effect is *not* inconsistent with our data, either. A larger sample of high field strength regions will be required to adequately address this problem.

To show the behavior of the dependence of frequency on activity, we fit a straight line to each individual mode difference as a function of MAI:

$$\frac{\delta\nu_{n,\ell}}{\nu_{n,\ell}} = a_{n,\ell}\Delta\text{MAI} + b_{n,\ell}. \quad (5.4)$$

The slopes $a_{n,\ell}$ are shown in Figure 5.4. The slopes in frequency shifts are seen to increase with frequency. It is notable, however, that the slopes are not a pure function of frequency — different n -ridges have slightly different dependences on frequency. At high frequency, there is some indication that the slopes turn over. It has been observed using ring diagram analysis in MDI data (Howe et al. 2008) and in Helioseismic and Magnetic Imager (HMI) data (Howe et al. 2011) that for frequencies above the acoustic cutoff, the slopes of frequency with magnetic field strength do in fact become negative. In our own sample, however, the quality of the fits do not permit us to extend our work much beyond the acoustic cutoff. The offsets $b_{n,\ell}$ are zero to within the uncertainties.

In order to determine the causes of the shifts, we have examined the relations between magnetic field strengths and mode parameters for various subsets of the total sample. In Figure 5.5, we have split the sample by phase of the solar cycle: the rising phase (1996 to 1999), the peak phase (2000 to 2002), and the falling phase (2002-2007). Although the correlation we find in frequency difference seems to differ between the peak phase, and the rising and falling phases, this is mostly due to the presence of very strong active regions in the peak phase and the aforementioned saturation at high frequencies.

We have also plotted the frequency differences against the time derivative of the

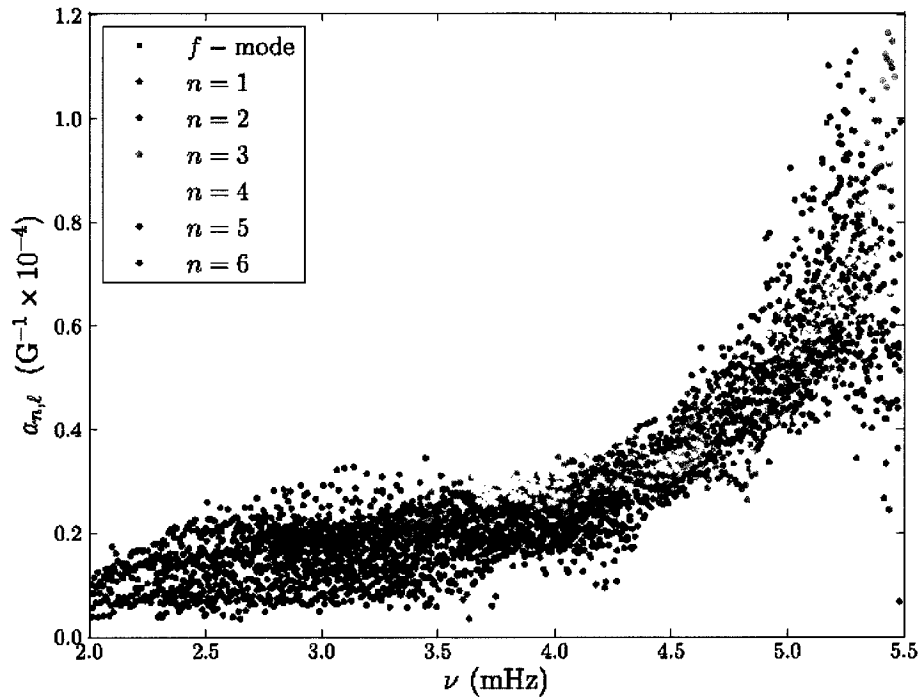


Fig. 5.4.— Slopes $a_{n,\ell}$ of individual mode frequency shifts with magnetic activity as a function of frequency up to $\nu = 5.5$ mHz. Different colors are used for different radial orders n .

Magnetic Activity Index of the active region, $d\text{MAI}/dt$. Here, we see some evidence of a difference, particularly in the f -modes. Figure 5.6 shows the frequency differences $\delta\nu$ as a function of ΔMAI , separated between positive $d\text{MAI}/dt$ (that is, regions which are growing in strength) and negative $d\text{MAI}/dt$ (decaying regions). We find no statistically significant difference between the two subsets.

We have examined the differences between different classes of sunspots in the centers of active regions. The majority of the active regions in our sample are classified as α or β types. When subdivided by type, the linear correlation is somewhat changed (though the correlation coefficients are not), and the distribution of the residuals for the α -type active regions now satisfy an Anderson-Darling test for

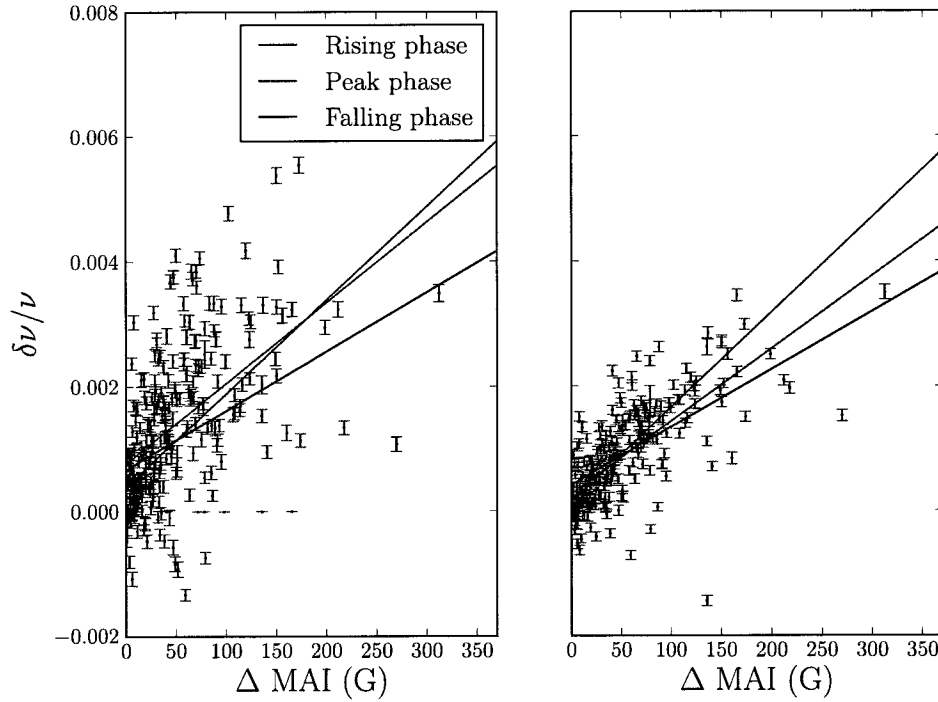


Fig. 5.5.— Frequency differences for two different modes and frequency ranges, plotted as a function of change in magnetic activity ΔMAI and split by phase of the solar cycle. Different colors denote different phases: the rising phase (cyan), the peak phase (green), and the falling phase (red). The left-hand panel shows the f -mode averaged for all modes with $2.75\text{mHz} < \nu < 3\text{mHz}$, and the right-hand panel shows the $n = 4$ ridge averaged over all modes with $4\text{mHz} < \nu < 4.25\text{mHz}$.

normality at the 15% level. The residuals for the β -type active regions do pass the 10% test, but do not do as well as the α -types. The slopes of the fits and the correlation coefficients are not changed by a statistically significant amount. In Figure 5.7 we show examples of $\langle \delta\nu \rangle$ separated by active region type, and the residuals to a linear fit.

The differences in the slopes between the α -type regions and the β -type regions are shown in Figure 5.8. There is a small but systematic trend with frequency in the slopes. For $\nu \lesssim 3.5 \text{ mHz}$, α -type spots have very slightly smaller slopes $a_{n,\ell}$,

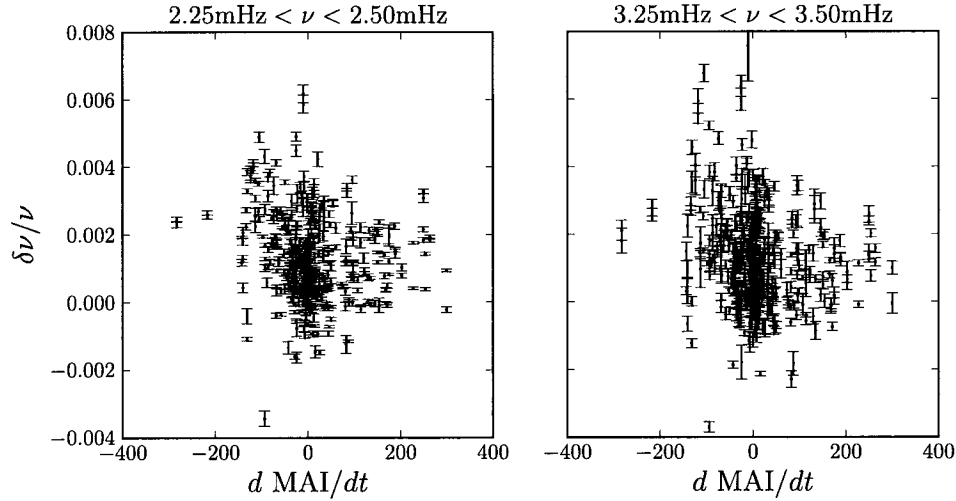


Fig. 5.6.— Averaged frequency differences in two different frequency bins are shown for the f -mode as a function of the growth parameter. The growth parameter is a linear fit to the the MAI with time.

while they are slightly larger for modes with $\nu > 3.5$ mHz.

5.3.2 Changes in other mode parameters

Other mode parameters are also known to change in the presence of magnetic fields. The mode amplitude A for the azimuthally symmetric component of the ring is related to the parameter A_0 from equation (5.1) by $A = \exp(A_0)$. In Figure 5.9, we show the changes in amplitudes A as a function of Δ MAI, averaged over the same modes as Figure 5.3. As has been seen in other works, we find that the amplitudes are decreased in the presence of magnetic fields. As is the case for frequencies, the dependence on MAI is linear. The mode widths w_0 are shown in Figure 5.10, and they are increased in the presence of magnetic fields.

We fit slopes to these parameters in the same way we did for frequencies,

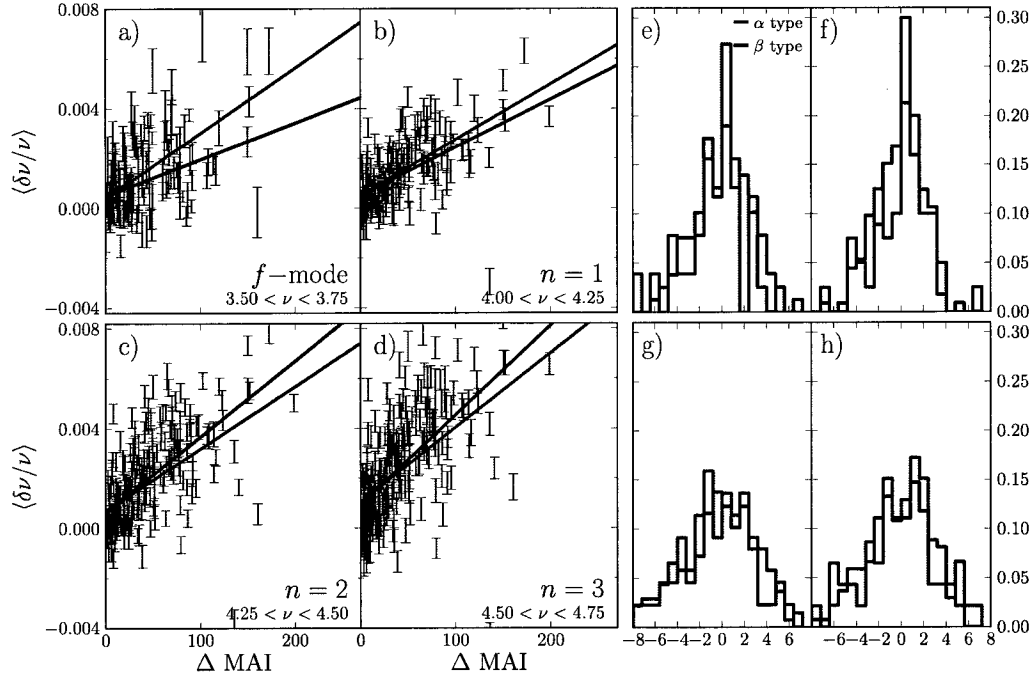


Fig. 5.7.— Averaged frequency differences separated by spot type for the f -mode and the first three p -modes as a function of the change in magnetic activity ΔMAI . The frequency ranges are shown in panels a) — d). Blue points denote α -type sunspots, red points denote β -type sunspots. Histograms of the residuals are also shown in panels e) — h).

defining our slopes by

$$\frac{\delta A(n, \ell)}{A(n, \ell)} = a_A(n, \ell) \Delta \text{MAI} + b_A(n, \ell) \quad (5.5)$$

and

$$\frac{\delta w_0(n, \ell)}{w_0(n, \ell)} = a_w(n, \ell) \Delta \text{MAI} + b_w(n, \ell). \quad (5.6)$$

The slopes for A and w_0 are shown in Figure 5.11. The amplitude slopes are, in general, negative as seen above, with a maximal change at approximately 3 mHz in the f -mode. The locations of the maximal changes in the p -mode ridges occur at higher frequencies with increasing radial order. The slopes are generally smaller in

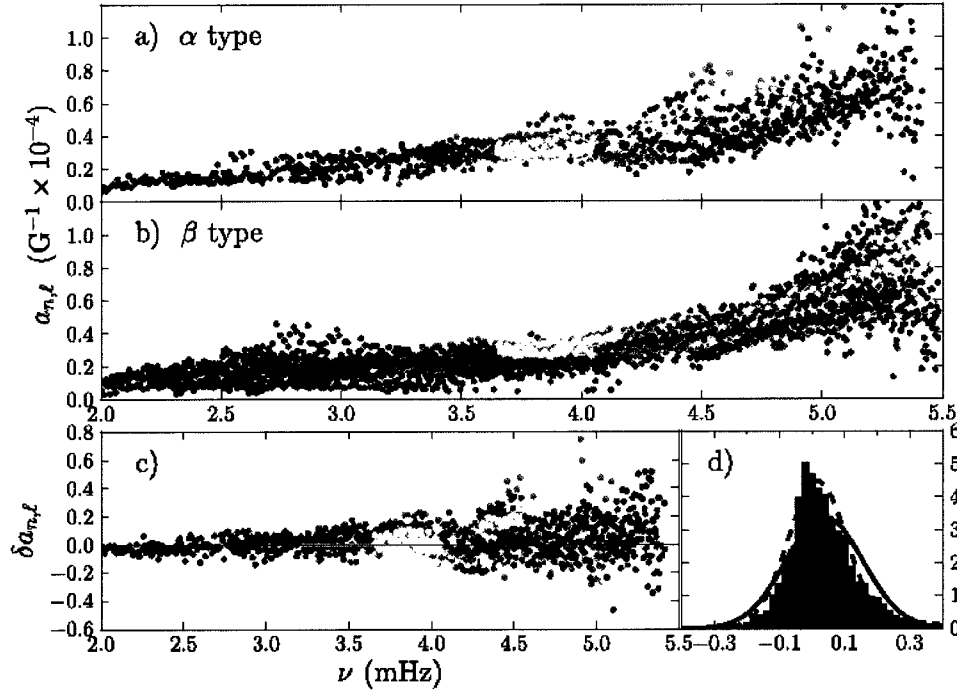


Fig. 5.8.— Differences in the slopes of individual mode frequency shifts with magnetic activity between α -type active regions and β -type active regions. Panels a) and b) show the slopes $a_{n,\ell}$ fit to the sample of α -type spots and β -type spots, respectively. Panel c) shows the differences $\delta a_{n,\ell}$ between the two sets of slopes. The differences are shown as a function of frequency up to $\nu = 5.5$ mHz. The sense of the difference is $\alpha - \beta$. Different colors are used for different radial orders n , and are the same as Figure 5.4. Panel d) shows a histogram of the differences from panel c). The solid line is the normal curve with the mean and standard deviation of the data; the dashed line shows the best fit gaussian.

magnitude for larger radial orders. At $\nu \sim 5.0$ mHz, the slopes approach zero, and in the higher order modes become positive. It appears that, above the acoustic cutoff frequency, mode amplitudes may be increased with magnetic fields, but the data do not allow us to explore this region of frequency space without difficulty.

The slopes of the mode widths in general behave in the opposite sense to the mode amplitudes, with positive slopes up to $\nu \sim 5.0$ mHz, and a maximal value at

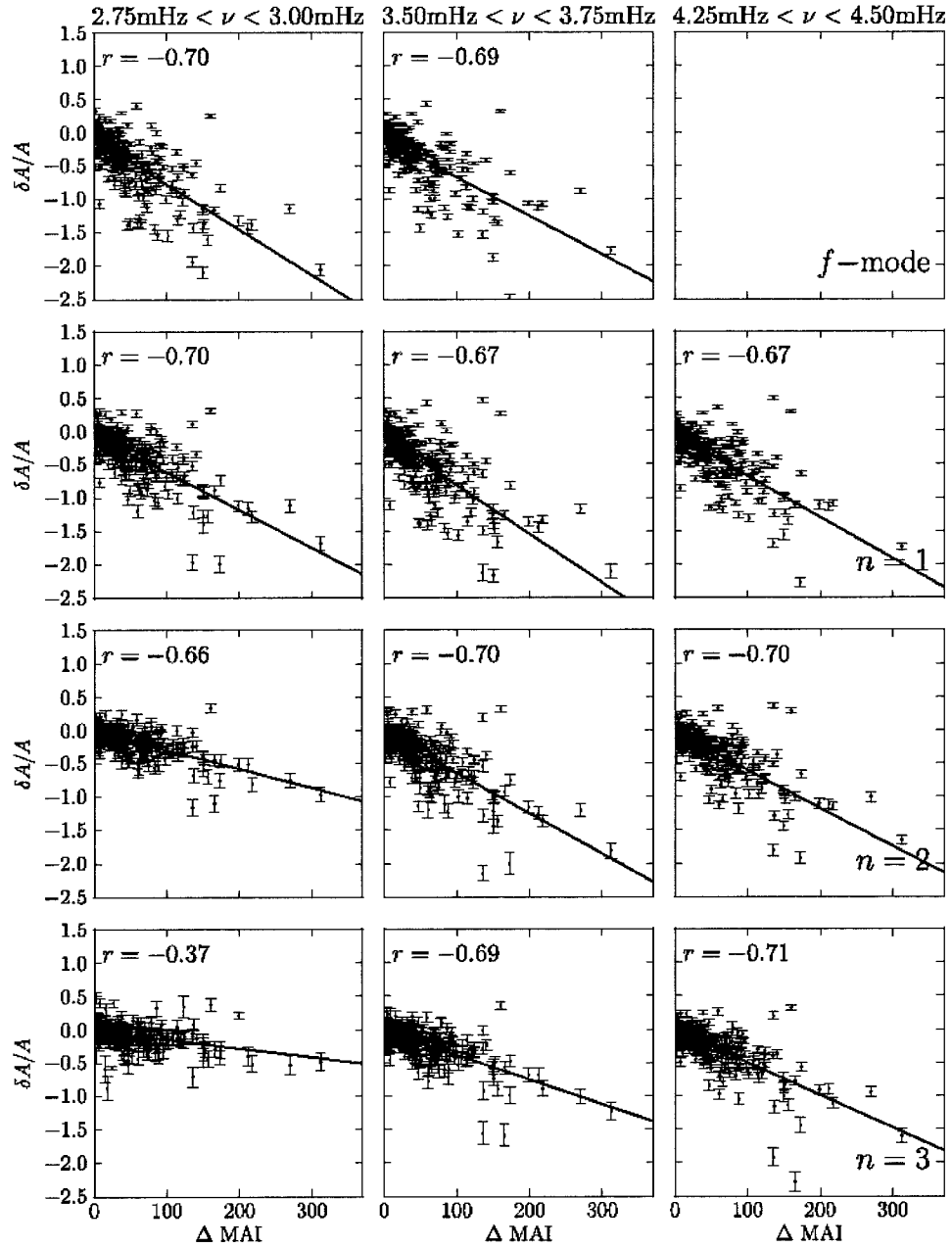


Fig. 5.9.— Averaged differences of the logarithm of the amplitudes in three different frequency bins are shown for the f -mode and the first three p -modes, as a function of the difference in MAI. As in Figure 5.3, the top right panel is blank because the f -mode does not extend that high in frequency.

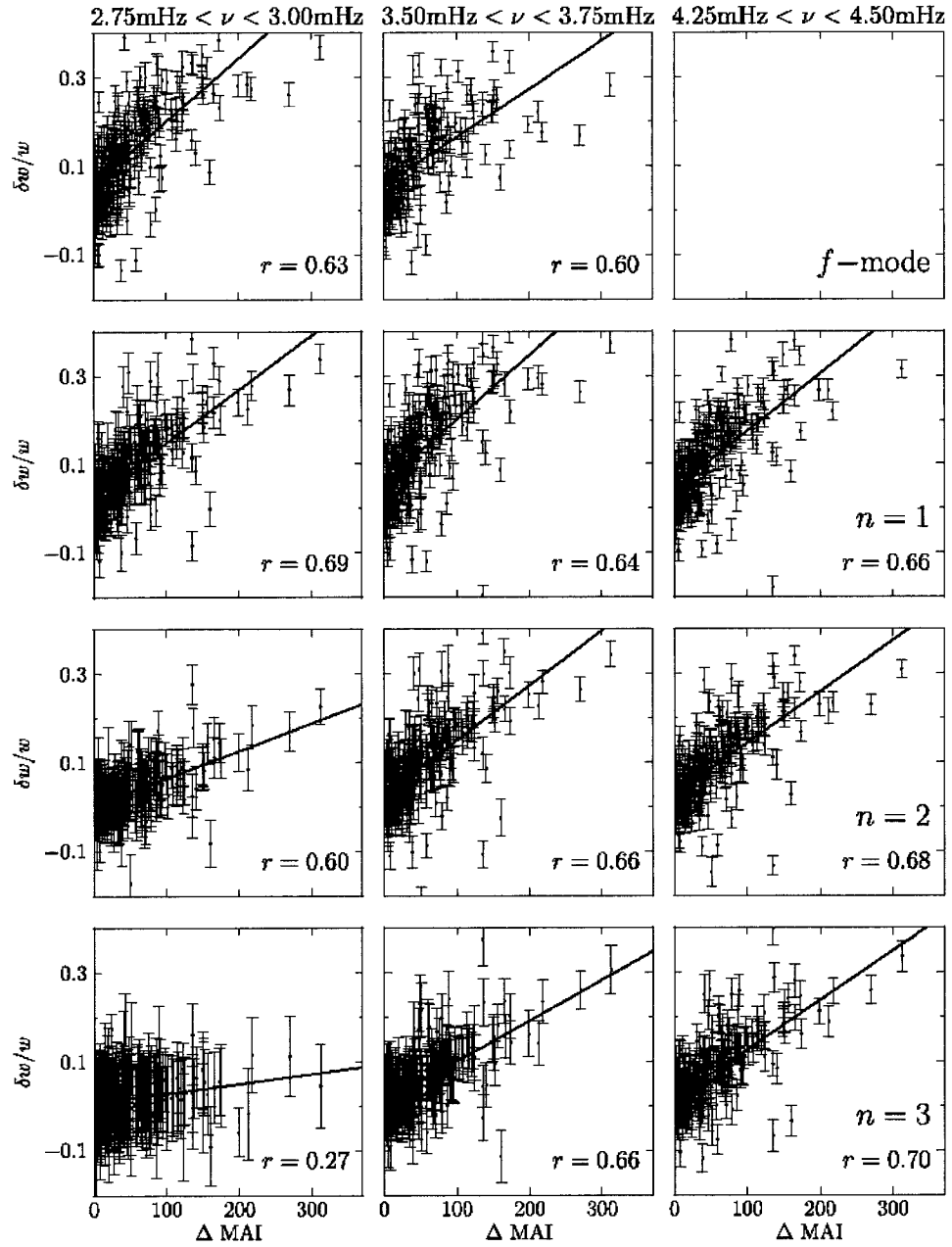


Fig. 5.10.— Averaged mode width differences in three different frequency bins are shown for the f -mode and the first three p -modes, as a function of the difference in MAI. As in Figure 5.3, the top right panel is blank because the f -mode does not extend that high in frequency.

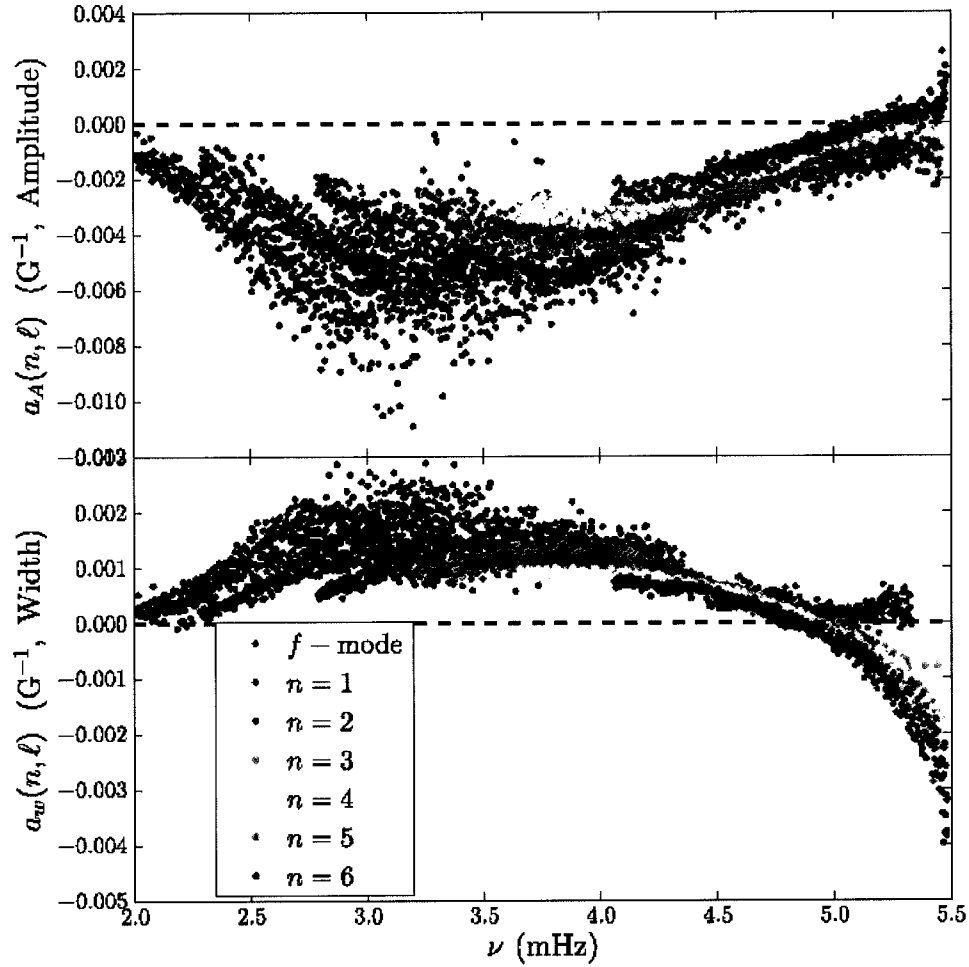


Fig. 5.11.— Slopes of individual mode amplitudes (top panel) and widths (bottom panel) with magnetic activity as a function of frequency.

$\nu \sim 3.0$ mHz. Above 5.0 mHz, the slopes are clearly negative, with the exception of the $n = 2$ mode, where the magnetic activity dependence appears to disappear. It is not clear why this order should behave differently from the other p -mode ridges. In Figure 5.12 we show how the slopes in amplitude and width vary with respect to each other. As expected, we see that, for positive width slopes, the correlation

between amplitude and width is linear. Interestingly, for negative width slopes, which corresponds to the modes with $\nu > 5.0$ mHz, the correlation changes.

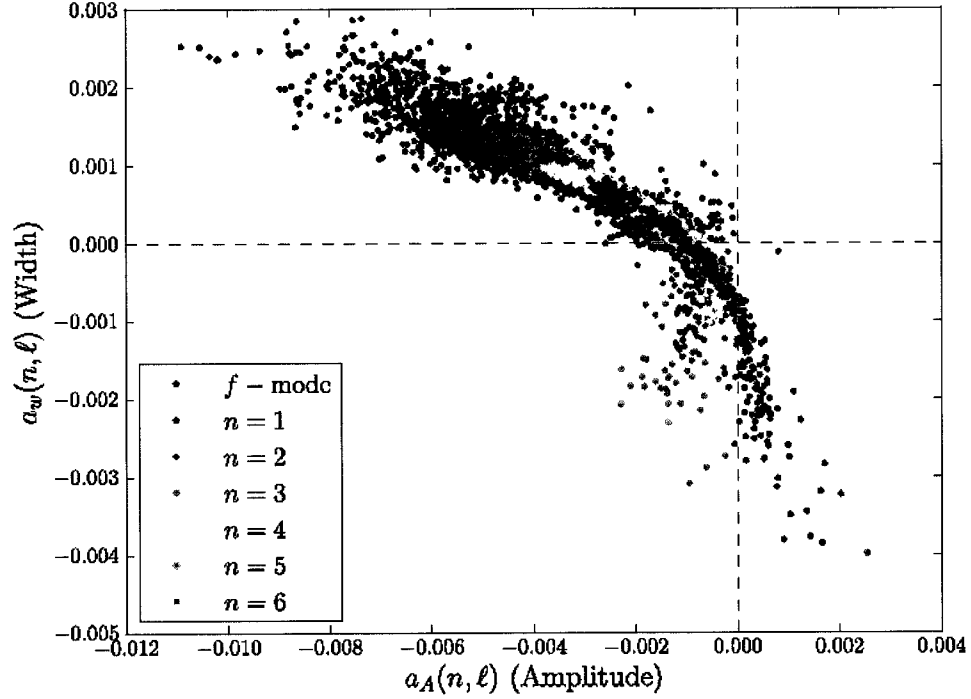


Fig. 5.12.— Slopes of mode widths as a function of frequency plotted as a function of the slopes of mode amplitudes.

We can compute the acoustic power in a given mode by integrating equation (5.1). The changes in mode acoustic power with magnetic activity are shown in Figure 5.13. As is already well-established, we find that power is suppressed in the presence of magnetic fields, with the largest suppression being between 3.0 mHz and 3.5 mHz. We do not see any evidence of power enhancement above the acoustic cutoff frequency.

Finally, in Figure 5.14 we plot the changes in the mode asymmetry S as a function of Δ MAI, shown for the same mode parameter averages as Figure 5.3. Though the uncertainties are comparatively larger than the other parameters studied here,

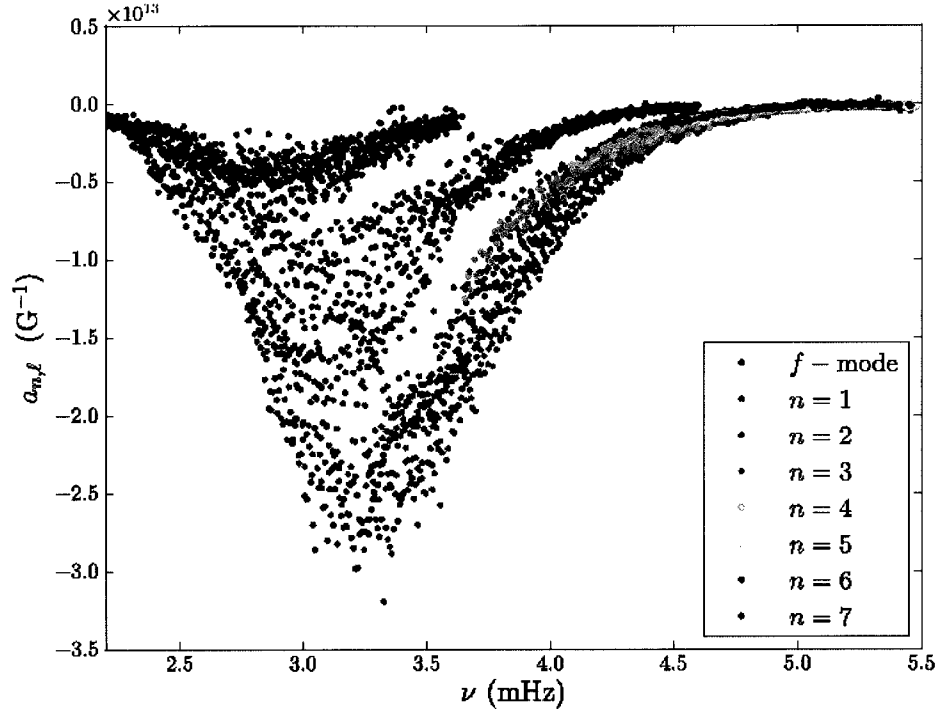


Fig. 5.13.— Changes in power in each individual mode with increasing MAI, plotted as a function of frequency.

we find that mode asymmetries increase in the presence of magnetic fields.

5.4 Discussion

It is by now well established that helioseismic frequencies below the acoustic cutoff frequency are enhanced in the presence of magnetic fields. In this work, we have measured mode frequencies for a large sample of active regions using ring diagram analysis. We find, consistent with most earlier work, that shifts in frequency are linearly correlated with the magnetic activity measured at the surface. These correlations hold for all mode sets and for the whole range of frequencies studied.

Both Howe et al. (2004) and Rabello-Soares et al. (2008) have presented fre-

quency shifts with ring diagrams at various levels of magnetic activity. Our results are generally quantitatively consistent with theirs, though we do not find any evidence of a quadratic dependence of the mode parameters on activity, as Howe et al. (2004) did. Rabello-Soares et al. (2008) find what appears to be a much cleaner relation with frequency than we do, in spite of the fact that they use the same frequency fitting technique and data from the same instrument. This is most likely due to the much smaller number of regions used in that study.

Our observations that mode amplitudes and widths are decreased and increased, respectively, are not novel (e.g., Lites et al. 1982; Title et al. 1992; Braun et al. 1992). Although attention has been paid to the effects that magnetic fields have on the acoustic cavity (Jain et al. 1996), the most common explanation for power suppression involves the complex interactions between purely acoustic modes and wave propagation in the presence of magnetic fields, where the modes can be damped (Cally 1995; Rosenthal & Julien 2000) or converted into other sorts of waves (e.g., Cally & Bogdan 1997; Crouch & Cally 2003, 2005; Shelyag et al. 2009; Felipe et al. 2010).

Our finding that the helioseismic frequencies of different active region types may be drawn from different statistical populations is novel. It implies that the surface geometry, not only strength, of the magnetic fields in an active region may determine the oscillation characteristics of the Sun.

It has been shown that the inclination of the magnetic fields can affect the amount of acoustic power absorption (e.g., Cally et al. 2003). Observational evidence for this has been found using helioseismic holography (Schunker et al. 2005, 2008) and time-distance analysis (Zhao & Kosovichev 2006). It is possible that we are seeing this effect averaged out over the much larger region sampled in ring diagram analysis.

Although we do find that the slopes $a_{n,\ell}$ are slightly different for the two different active region types, the fact that these differences appear to be simply a function of frequency implies that it is very unlikely to be due to changes in the thermal structure in the regions typically resolved in ring diagram structure inversions. In the region where the upper turning points of the modes are located, however, it is possible that a different thermal stratification in different sunspot types would give rise to a difference such as the one we have detected, since upper turning points are shallower with increasing frequency. The direct effects of magnetic fields also have an effect on the upper turning points, as was shown by Jain (2007) in the case of horizontal magnetic fields.

The errors in the measurement of the MAIs are small, but it is possible that small systematic errors arise from the fact that the calculation is restricted to the line-of-sight fields. Different surface field configurations could give rise to somewhat different systematic errors. It is difficult to estimate how large this effect could be at present, but continuously available high-resolution data becoming available from the Helioseismic and Magnetic Imager (HMI) on the Solar Dynamics Observatory (SDO) is allowing full vector inversions for magnetic fields. This will allow us to more accurately compute the total magnetic fields in active regions.

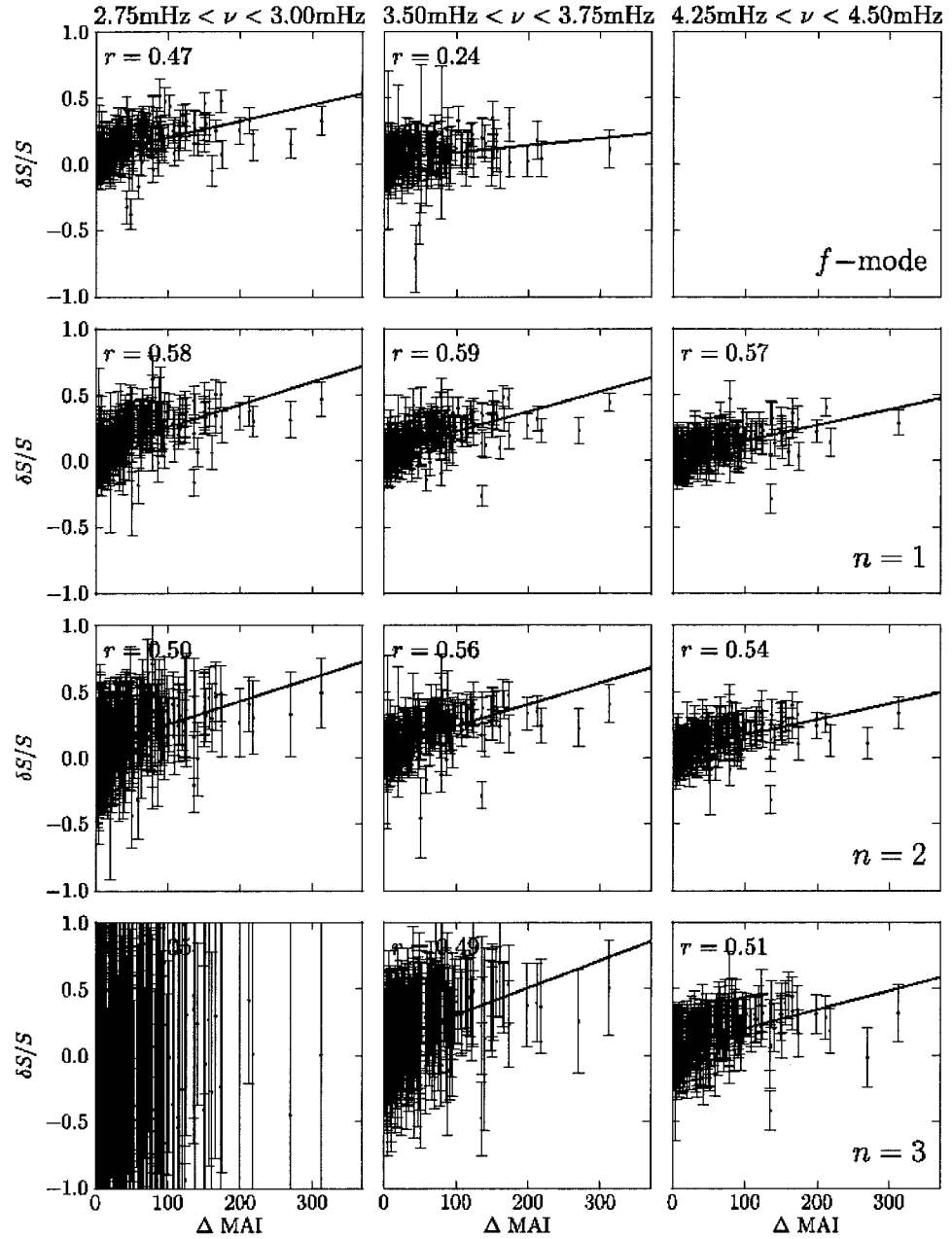


Fig. 5.14.— Averaged mode asymmetry differences in three different frequency bins are shown for the f -mode and the first three p -modes, as a function of the difference in MAI. As in Figure 5.3, the top right panel is blank because the f -mode does not extend that high in frequency.

Chapter 6

The Structure of Active Regions

6.1 Introduction

Understanding the subsurface structure of sunspots is one of the current major avenues of research in solar physics. Helioseismology provides a unique opportunity to determine the structure of sunspots empirically, but this determination involves substantial difficulties. In Chapter 5, we examined the changes to ring diagram power spectra in the presence of the strong magnetic fields found in active regions. In this chapter, we attempt to interpret these changes in terms of perturbations in the thermal structure of the Sun beneath active regions, using the same inversion techniques we applied to the global modes of the Sun in Chapter 3.

In previous works, inversions of ring diagram frequencies for structure have been performed on small numbers of rings (Basu et al. 2004; Bogart et al. 2008) to determine the changes in sound speed and adiabatic index. In these works, sound speed and adiabatic index were found to be enhanced in the layers between approximately $0.975R_{\odot}$ and $0.985R_{\odot}$, and depressed in the shallower layers between $0.99R_{\odot}$ to $0.998R_{\odot}$.

In this work, we extend this type of analysis to a much larger sample, with which we hope to say something statistically significant about the thermal structure beneath active regions. In Section 6.2, we discuss the ring diagrams in this sample and in particular the difficulties in the determination of errors. In Section 6.3, we discuss the inversion technique used. In Section 6.4, we present the results of inversions for sound speed and adiabatic index, and we discuss the results and difficulties in interpretation in Section 6.5.

6.2 Ring diagram frequencies and errors

In this chapter, we use ring diagram measurements from the same sample described in Chapter 5. Since small magnetic field strengths generally give rise to small frequency perturbations, we do not use the weakest regions in this chapter.

For the inversions in this work, we invert differences in temporal frequencies ν between two different observations of the Sun. The fit technique that we use, however, fits for *spatial* frequency at constant temporal frequency. For this reason, estimating the uncertainties in ν is not straightforward. Earlier works using this fit technique have estimated errors in frequency by taking the formal uncertainty in the fit mode width w_0 as the error in frequency. This is not strictly justified, but Basu et al. (1999) and subsequent authors found it to provide a reasonable estimate of the errors. For this work, we have explored the issue of uncertainties in the determinations of mode frequencies using Monte Carlo simulations of the errors in ring diagram power spectra. A comparison of errors from these Monte Carlo simulations for one ring with the errors in w_0 is shown in Figure 6.1. We find that, in general, the errors in the frequencies agree to within factors of a few with the formal uncertainties in w_0 , but that the errors in w_0 systematically

overestimate the actual errors in ν . In fact, the errors estimated from the Monte Carlo runs indicate that the actual uncertainties in ring frequency fits are relatively constant (at approximately $1 \mu\text{Hz}$) for most of the ridge. These uncertainties increase sharply at the edges of the fit ridges, where we generally reject the fits. Because repeating this Monte Carlo estimation for all the rings in this sample would be prohibitively expensive, we continue to use the errors in w_0 in the way previous authors have done, with the caveat that these errors may not be correctly estimated.

In addition to the errors in individual mode frequency measurements, correlations between different mode measurements need to be addressed. Fitting as we do at constant frequency, we are effectively oversampling the data, and thus we expect substantial error correlations between adjacent fits. Estimating these correlations directly from the fits is very difficult since each fit is formally independent. We explored the error correlations in the fits using Monte Carlo simulations. We find that the error correlations are indeed substantial between adjacent modes and that the oversampling is close to a factor of ten. Therefore, for this work we only use every tenth mode fit. Error correlations between modes primarily has the effect of causing underestimations of the errors in the inversion results. The inversion results themselves are not strongly susceptible to error correlations.

6.3 Inversions

Unlike in global mode analysis, we do not decompose our observation onto a spherical harmonic basis set. Rather than discrete modes, therefore, continuous ridges of power are observed. The fits we obtain to these power spectra, then, are not generally at integer values of ℓ . Nevertheless, we can interpret these power spectra

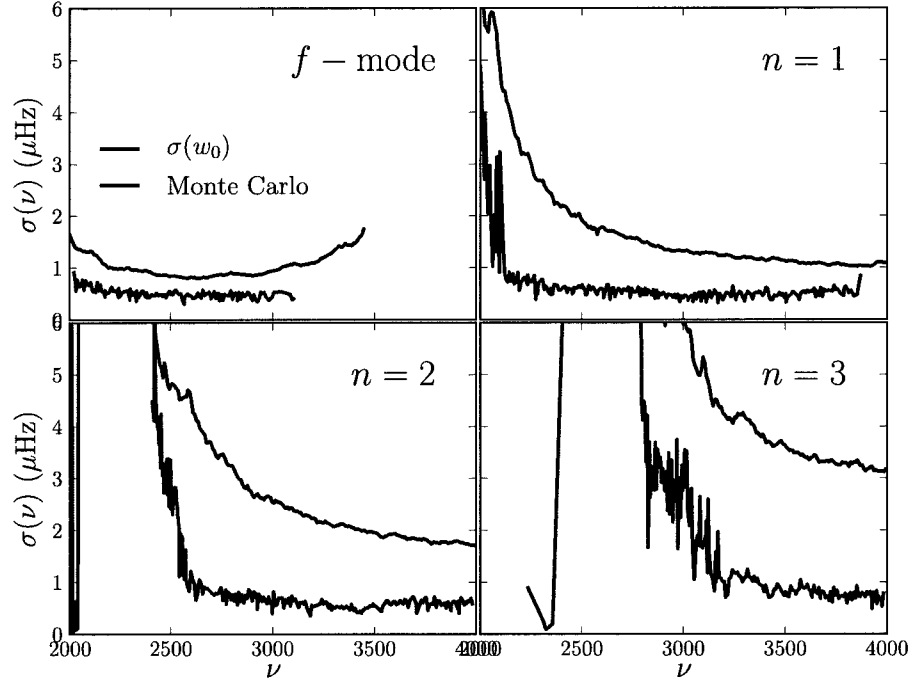


Fig. 6.1.— A comparison of the actual errors in frequencies inferred in a given ring (green), estimated using a Monte Carlo simulation, with errors in the mode width w_0 (blue). The comparisons are shown as a function of frequency for the f -mode and the first three p -modes.

in the same way we interpret global mode frequencies by interpolating our fits to integer ℓ values, and treating these modes as global standing waves.

As in global mode inversions, we perform a linear inversion of the measured frequency differences. We use Subtractive Optimally Localized Averages (SOLA, see 2.2.2). The inversions are performed on the differences in frequency between the active region ring diagram frequencies and the associated quiet region frequencies. Thus, we do not measure any absolute thermal properties of the Sun, only the difference between quiet and active Sun.

The principal effort in performing an inversion for structure from helioseismic data is the difficulty in choosing the appropriate inversion parameters. A thorough exploration of the parameter space was performed on a small subset of the rings, including comparisons to rings published in earlier works. We find that the inversion results are not strongly dependant on the choice of surface term, so long as the surface term is not suppressed entirely. We restrict ourselves to $\Lambda = 4$, therefore. In exploring the effects of the target kernel width, we find smaller values of $\Delta(r_0)$ tend to cause oscillatory solutions to many inversions. Since we have not found any particularly sharp features in our inversions, we use a fairly large value of $\Delta(r_0) = 0.055$, which suppresses some oscillatory behavior in certain inversions, and does not overly smooth actual structure in better inversions.

Finally, for the choices of the error suppression term μ and the trade-off parameter β , we have found that the values of these parameters for acceptable inversions in the rings we have examined carefully fall in a fairly narrow range. For the full sample, then, we run a batch of inversions for each region over the sample. Examining the inversions for each region can then be done fairly quickly and the best set of inversion parameters selected. We reject regions with unstable inversions — that is, regions whose inversion results are very strongly dependent on the choice

of inversion parameter. What remains comprises our sample of sound speed and adiabatic index inversions.

6.4 Results

Inversions for the difference in squared sound speed c^2 and adiabatic index Γ_1 were performed for all regions in the sample with $\Delta \text{MAI} \geq 40$ G. Figure 6.2 shows example sound speed inversions for four different rings with a range of active region strengths as a function of depth. Figure 6.3 shows inversions for adiabatic index for the same regions.

Figure 6.4 shows averages of the inverted sound speed for all regions in our sample for different depth ranges. For sound speed averaged between $0.975R_\odot$ and $0.985R_\odot$, sound speeds are generally enhanced in the presence of magnetic fields, while in the region from $0.99R_\odot$ to $0.998R_\odot$, sound speeds decrease. In both regions, the magnitude of the change tends to increase with magnetic field strength, although the relationship seems to be more of an envelope than a linear relation. Further, there seems to be some saturation of the effect at very high magnetic field strengths. The inversion results for the adiabatic index are shown over the same range of depths.

In Figure 6.5, we plot the boundary between the positive and negative perturbations as a function of ΔMAI . We compute this by interpolating between inversion points and finding the zero crossing. There is no obvious dependence of the boundary point on magnetic activity.

We have also inverted for the first adiabatic index, Γ_1 . In Figure 6.6, we show the same averages as Figure 6.4, but for the Γ_1 inversions. In general, Γ_1 is an easier quantity to invert for (in the sense that the inversions tend to be less sensitive to

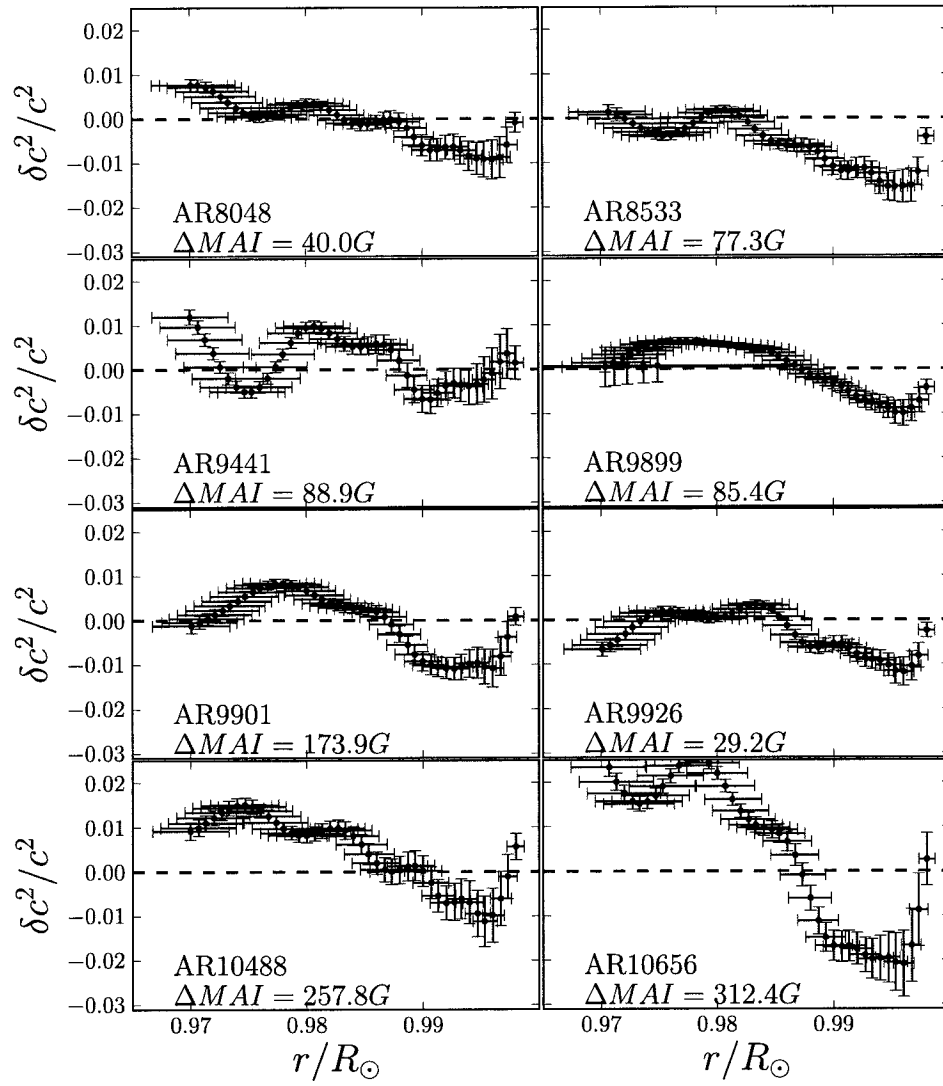


Fig. 6.2.— Examples of inversions for adiabatic sound speed squared c^2 for eight active regions. The sense of the inversions are active minus quiet. The plotted horizontal error bars are taken from the first and third quartile points of the inversion averaging kernels.

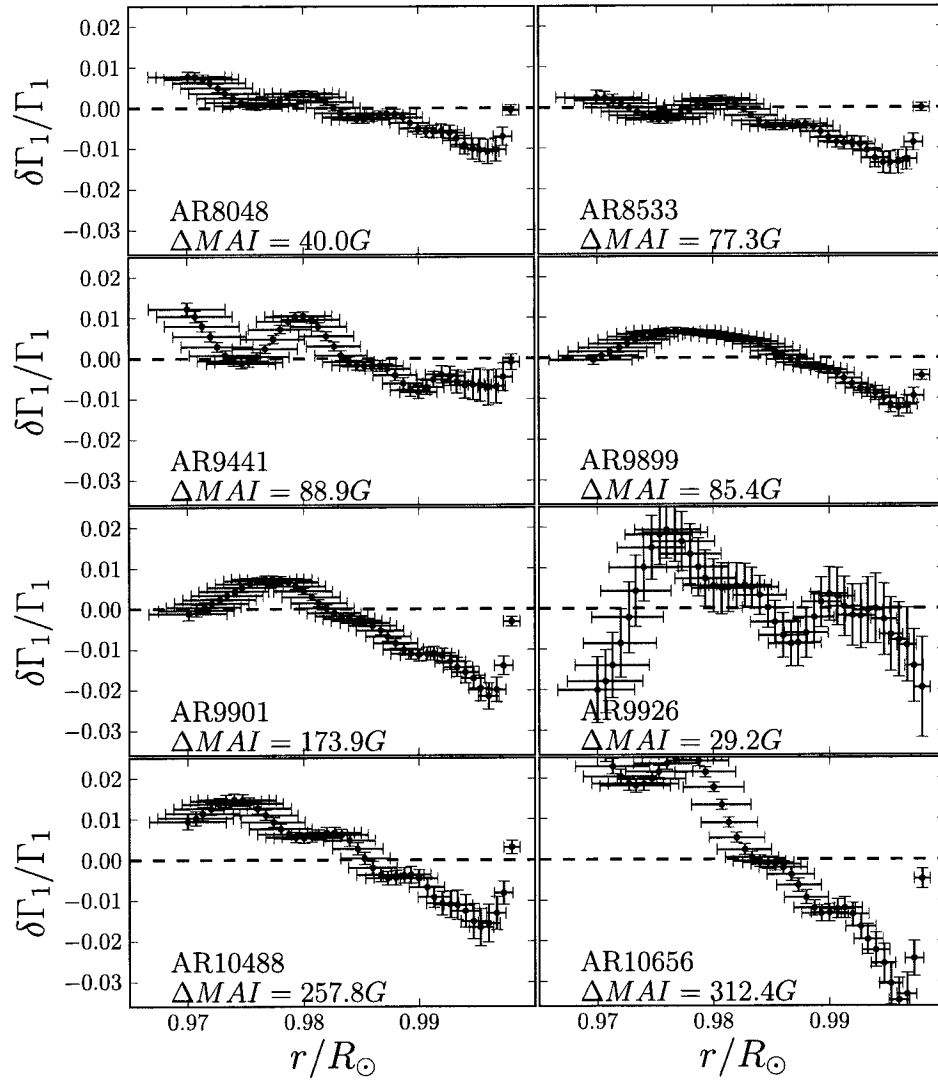


Fig. 6.3.— Examples of inversions for adiabatic index Γ_1 for eight active regions. The regions shown are the same as Figure 6.2.

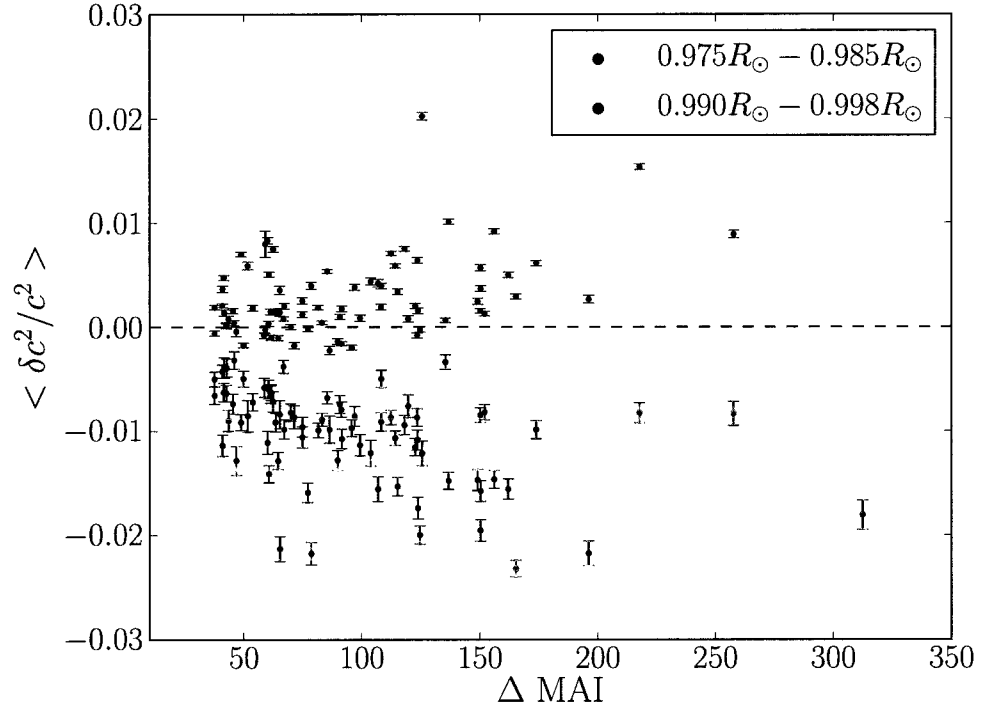


Fig. 6.4.— Averages of inversions for c^2 over two depth ranges are shown, plotted as a function of ΔMAI . Blue points are averages of inverted sound speed between $0.975R_\odot$ and $0.985R_\odot$; red points are averages of inverted sound speed between $0.990R_\odot$ and $0.998R_\odot$.

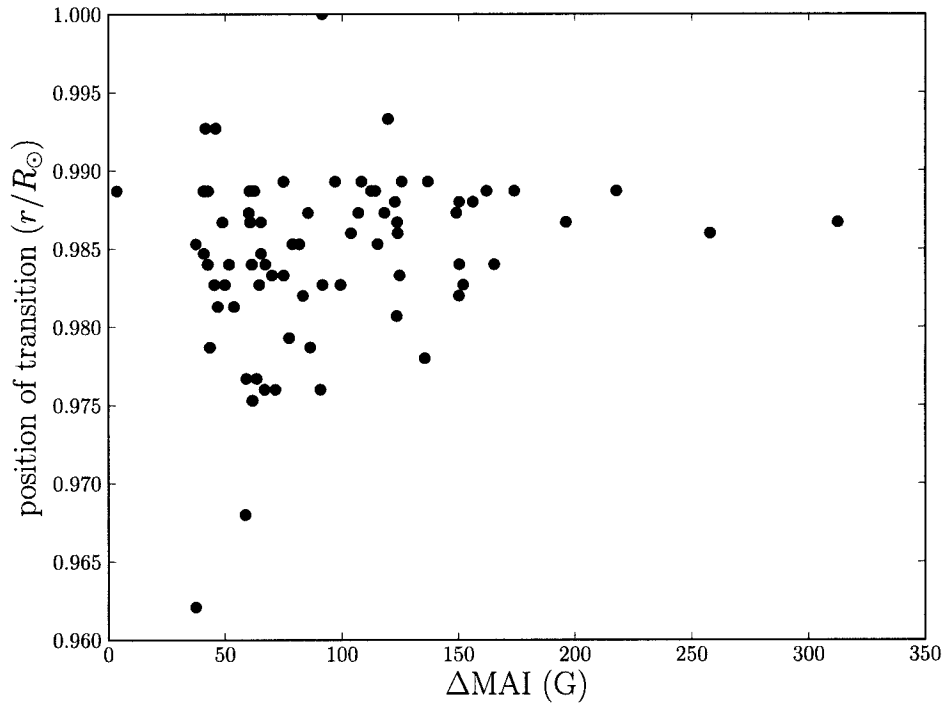


Fig. 6.5.— Position of transition, in fractional radius, between the negative (shallower) sound speed perturbations and the deeper (positive) perturbations in the sound speed inversions, plotted as a function of ΔMAI . These transition points are found by treating the inversion points as a continuous curve and finding the zero-crossing point.

the inversion parameters), and so we include a larger number of inversions for Γ_1 than we could for c^2 .

We find that, like the c^2 results, there is a depression in Γ_1 in the shallower layers that we invert (above $r = 0.99R_\odot$), and that, in many cases, there is a corresponding enhancement below approximately $r = 0.98R_\odot$, as was found by earlier works. We find that the deeper enhancement is, for most rings, much less pronounced than for the c^2 . For some regions, in fact, we do not see any positive perturbation at all, and in general we find only a weak correlation with magnetic activity.

In Figure 6.7, we plot the boundary between the positive and negative perturbations (for those regions where we detect both). As in the c^2 inversions, we do not find any systematic dependence on magnetic activity.

6.5 Discussion

Earlier works Basu et al. (2004); Bogart et al. (2008) have studied the structure of sunspots using ring diagrams, but have had much smaller sample sizes. In general, we find results consistent with these earlier works. We find that both sound speed and adiabatic index are enhanced in the layers between approximately $0.975R_\odot$ and $0.985R_\odot$, and are depressed in the shallower layers between $0.99R_\odot$ to $0.998R_\odot$. We do not extend our inversions beyond these regions, as the helioseismic data contains less information outside these layers, and getting reasonable inversions requires great care.

Bogart et al. (2008) found a linear correlation between magnitude of the sound speed change and strength of the active region. We find a similar relation, but with substantial scatter. Further, we find that the correlation appears to saturate at

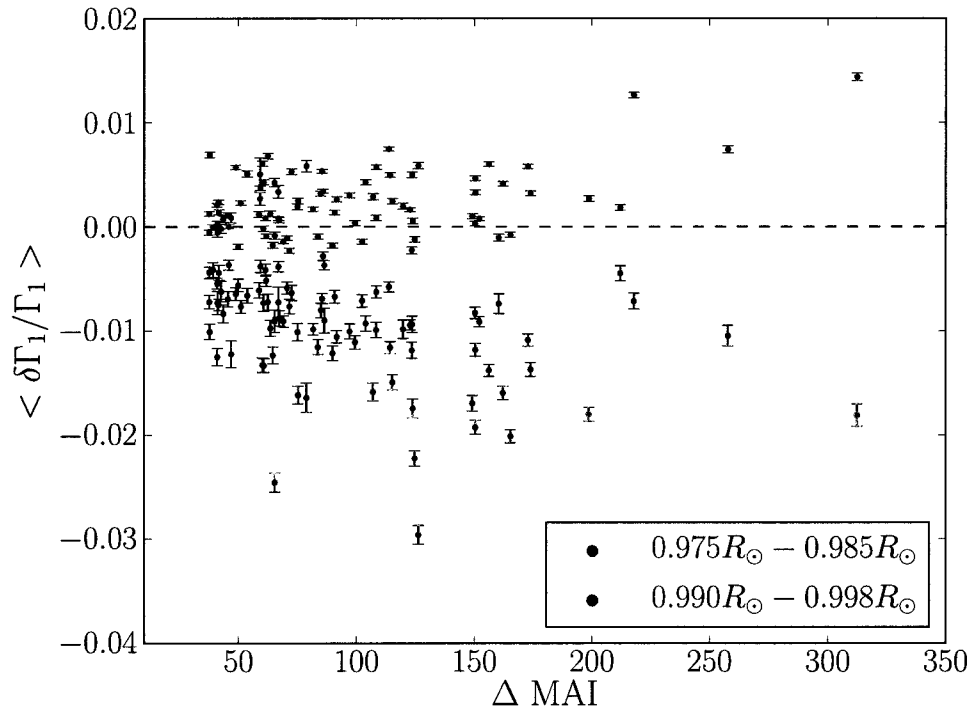


Fig. 6.6.— Averages of inversions for Γ_1 over two depth ranges are shown, plotted as a function of ΔMAI . Blue points are averages of inverted sound speed between $0.975R_\odot$ and $0.985R_\odot$; red points are averages of inverted sound speed between $0.99R_\odot$ and $0.998R_\odot$.

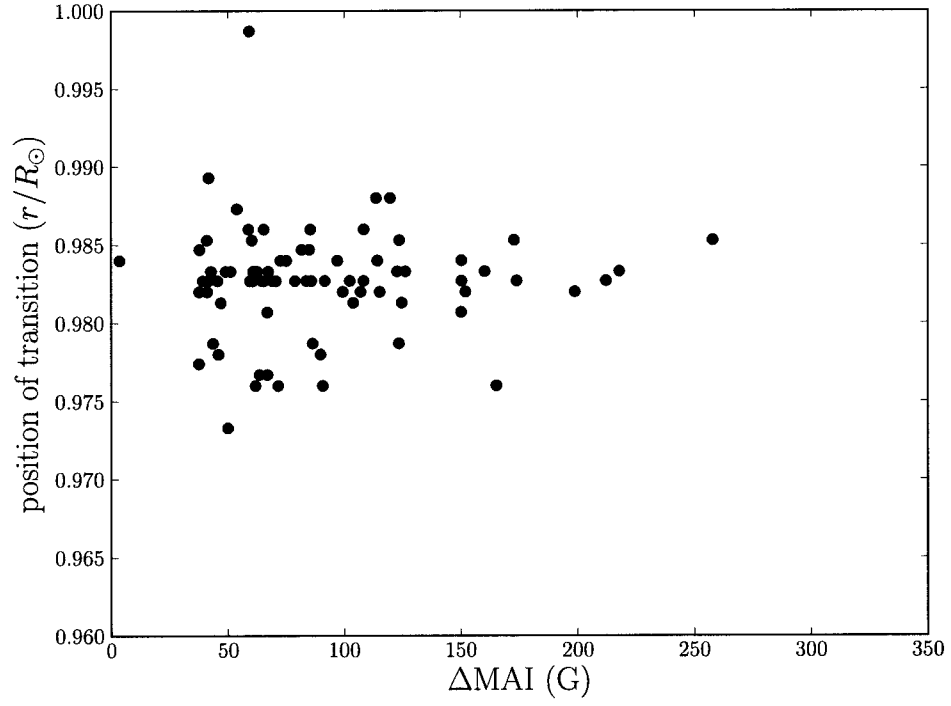


Fig. 6.7.— Position of transition, in fractional radius, between the negative (shallower) adiabatic index perturbations and the deeper (positive) perturbations in the sound speed inversions, plotted as a function of ΔMAI . These transition points are found by treating the inversion points as a continuous curve and finding the zero-crossing point.

high field strengths. This effect is pronounced in the Γ_1 inversions for the shallow negative perturbation. We find that the positive perturbation in Γ_1 is much weaker than in c^2 , and that the correlation with magnetic activity is much less significant.

Bogart et al. (2008) also reported that the depths of the positive perturbations in Γ_1 were deeper than those in the c^2 inversions. Comparing Figures 6.5 and 6.7, we find that this is true, although the scatter in the c^2 boundaries is larger than for the Γ_1 boundaries.

The two-layer structure in sound speed can be most simply interpreted as the effect of placing a cool ‘cap’ on the convective upflow at the surface of the Sun. This has the effect of lowering the temperature and hence the sound speed near the surface. Below this, hot material being brought up convectively from deeper layers piles up against the magnetic barrier, causing an increase in temperature.

The first adiabatic index Γ_1 is determined by the equation of state, and remains very close to the ideal gas value of $5/3$ except in ionization zones. A change in Γ_1 could be caused by a change in the equation of state itself, though this is unlikely as it would require an extremely strong magnetic field. Alternatively, a change in the thermal structure could cause the ionization zones to shift. In the present case, the second Helium ionization zone (Basu & Mandel 2004) could be responsible for the shifts we see. Moving the Helium ionization zone upwards in the presence of magnetic fields would be consistent with our measurements of Γ_1 .

The physical interpretation of these results is problematic, however. Basu et al. (2004) concluded that the changes they inferred in c^2 and in Γ_1 could not be explained by thermal perturbations alone. This is not surprising, since active regions are distinguished by their strong surface magnetic fields — it is expected that the layers beneath the surface are also characterized by the presence of strong magnetic fields. If this is the case, then the waves which we interpret as purely

acoustic modes in fact have a magnetic component to their propagation, which vastly increases the complexity of the problem.

Lin et al. (2009) supposed that magnetic fields in these layers primarily influenced the helioseismic modes through the influence of magnetic pressure:

$$P_{\text{mag}} = \frac{B^2}{8\pi}, \quad (6.1)$$

so that the wave speed could be given by

$$c^2 = \Gamma_1 \frac{P_{\text{tot}}}{\rho}, \quad (6.2)$$

where $P_{\text{tot}} = P_{\text{gas}} + P_{\text{mag}}$ is the total pressure. Under this approximation, they used 1-dimensional models to relate the changes in c^2 and Γ_1 inferred from ring diagram analysis to magnetic perturbations.

It is also useful to compare ring diagram results with other local helioseismic measurements of the subsurface sound speed. In particular, time-distance helioseismology has been used to measure the wave speed perturbation below active regions (e.g. Kosovichev et al. 2000), and it was in general believed that time-distance results were in qualitative agreement with ring diagram results. Recent work, however, directly comparing ring diagram and time-distance analysis (Gizon et al. 2009; Moradi et al. 2010) found striking disagreement between the two techniques. It is still not clear at the time of this writing how this discrepancy can be resolved, but it is clear that the presence of magnetic fields, which affect both the data measurements and the data analysis, need to be taken into account before further progress in the helioseismology of active regions can be made.

Chapter 7

Conclusions

In this thesis, we have used the techniques of helioseismology to explore the signatures of solar activity in the interior over the course of solar cycle 23. Understanding the underlying mechanisms that drive solar activity is an important problem, and we summarize here the progress that we have made in this area.

We have found that the interior of the Sun changed slightly but significantly over the course of the last solar cycle. Chapter 3 describes a change, which we interpreted as a change in the sound speed, at the base of the convection zone which was tightly correlated with surface activity. We have also attempted to measure the magnetic fields of the solar interior directly — Chapter 4 describes the axisymmetric magnetic field configuration that can best explain the helioseismic splitting coefficients measured by the MDI instrument. We find that this is predominantly a toroidal field in the very shallow layers of the Sun, with a small poloidal component. The signal-to-noise deeper in the convection zone is too small to detect magnetic fields that could be associated with the changes we detected in Chapter 3.

Examining the near-surface layers in more detail, we turn to the effects of active

regions on the solar structure beneath them. Examining a large sample of active regions in Chapter 5, we find, as other authors have before us, that helioseismic frequencies increase in active regions, while power is suppressed. The novel result that we find is that the surface geometry of the magnetic fields, for which we use the sunspot classifications as a proxy, appears to have some effect on the frequency changes with magnetic field strength.

The sound speed of structure beneath active regions has been found to be a two-layer structure (Basu et al. 2004). We examine large number of regions and confirm this, finding that in there is a shallow layer of sound speed decrease relative to the quiet Sun, and below this a region of enhanced sound speed. The magnitudes of these perturbations has in the past been found to increase with surface field strength. We find that there is a great deal of scatter in the perturbation magnitudes, but that they appear to be bounded by an envelope which is a linear function of surface field strength. The depth at which the negative perturbation becomes positive has a significant amount of scatter but we do not find any pattern in the differences.

The adiabatic index Γ_1 shows a similar structure as the sound speed, though here we do not find that the positive perturbation below is as strong as the sound speed perturbation, and in many regions is not found at all. The shallow negative perturbation is, like the sound speed results, bound by an envelope which is a function of activity, but the deeper layer does not show much correlation with activity. The negative perturbation in Γ_1 is also found to penetrate somewhat deeper than the equivalent sound speed perturbation.

While we can draw no definitive conclusions about the solar dynamo and the emergence of active regions from this work, we can point out a few tentative conclusions. We have found some evidence that activity-related structure changes

occur at the base of the convection zone or in the tachocline — this is in support of an interface dynamo model. The tight correlation between surface activity and the similar dependence on latitude may be evidence that the flux tubes that emerge to form active regions originate at the base of the convection zone. Unfortunately, current helioseismic data have yet to detect signatures of this emergent flux.

In a related vein, we have found additional evidence to support the picture of sunspots as relatively deeply penetrating phenomena, rather than the shallow features that are often presented in numerical simulations. These results are not currently confirmed by other helioseismic techniques (see Gizon et al. 2009) and so must be interpreted with care, but the consistency of these measurements over a large number of active regions lays to rest concerns about the effects of the numerical stability of these inversions on this result.

Interpretation of these results remains an unsolved problem. In particular, it remains unclear how the local phenomena (active regions) connect to the global phenomena (the global-scale magnetic fields and the solar dynamo). Some further progress on these problems will be made simply by virtue of the better data that is becoming available from the Helioseismic and Magnetic Imager (HMI) on the Solar Dynamics Observatory (SDO) spacecraft. HMI is an MDI-like instrument, with better resolution and a much greater telemetry bandwidth. This improved data will allow us to see the helioseismic signatures of solar cycle 24 with much greater precision than we could cycle 23.

The future work in this field, whatever the quality of the data, will necessarily involve a detailed accounting of the effects of magnetic fields on the helioseismic wave propagation. Our work in Chapter 4 is an attempt to do that, but the formalism used is limited by its restriction to axisymmetric fields — understanding the measurements in active regions clearly requires the relaxation of those assump-

tions.

We have shown, then, that changes in thermal structure throughout the solar convection zone do occur over time-scales relevant to the solar activity cycle. We have shown further that these changes are highly correlated in time with activity observed on the solar surface and in the atmosphere. We have presented evidence that individual active regions affect the solar structure down to a depth of at least 2% of the solar radius, and that the changes in structure are to a certain extent correlated with the strength of the magnetic fields at the surface.

Appendix A

Principal Component Analysis

We give a brief description of the Principal Component Analysis technique that follows the one found in Kendall (1980). This technique assumes that we begin with a set of observations, each one consisting of a set of data points (for example, a set of spectra of different objects, or a set of images, or, as in this paper, sets of mode frequency measurements at different points in time). Assume we have m observations, each with n data points. The m vectors \mathbf{x}_i each contain the n data points x_{ij} , measured relative to the mean \bar{x}_j . We wish to find a new set of vectors \mathbf{c}_i that are linearly dependent on \mathbf{x}_i , and uncorrelated with each other. In addition, we require that they have stationary values of their variance. This condition is imposed to ensure that most of the variance is accounted for in as few vectors \mathbf{c}_i as possible. Alternatively, this condition can be viewed geometrically as a rotation of the basis vectors such that the variance of the data with respect to each basis vector is maximal. This is most easily understood in the case of a two dimensional data set, where PCA is equivalent to a linear fit to the data, and the rotation sets one basis vector parallel to that fit. The vectors \mathbf{c}_i will be given by

a linear combination of the original observations:

$$\mathbf{c}_i = \sum_{j=1}^n \xi_{ji} \mathbf{x}_j. \quad (\text{A.1})$$

The vectors ξ_j will form a new basis set for the observations. The variance of \mathbf{c}_i is given by

$$\text{var } \mathbf{c}_i = \sum_{j=1}^n \sum_{k=1}^n \xi_{ji} \xi_{ki} e_{jk}, \quad (\text{A.2})$$

where e_{jk} is the covariance between x_j and x_k . The covariance matrix is given by

$$\mathbf{E} = \frac{1}{n} \mathbf{X} \mathbf{X}^T, \quad (\text{A.3})$$

where \mathbf{X} is the matrix $(\mathbf{x}_1, \mathbf{x}_2, \dots, \mathbf{x}_m)$. In order to get unique solutions for the values of ξ_{ji} , we impose a normalization condition:

$$\sum_{i=1}^m \xi_{ji}^2 = 1. \quad (\text{A.4})$$

Finding the stationary values of $\text{var } \mathbf{c}_i$ (eq. A.2) with the condition A.4 is equivalent to finding the stationary values of:

$$\sum_{j=1}^m \sum_{k=1}^m \xi_{ij} \xi_{ik} e_{jk} - \lambda \left(\sum_{j=1}^m \xi_{ij}^2 - 1 \right), \quad (\text{A.5})$$

where λ is some constant. To find the stationary values, we differentiate A.5 by ξ_{ij} and find the roots of the equation:

$$\sum_{k=1}^m \xi_{ik} e_{jk} - \lambda \xi_{ij} = 0. \quad (\text{A.6})$$

This is an eigenvalue problem — the vector $\boldsymbol{\xi}_j$ is an eigenvector of \mathbf{E} and λ is the corresponding eigenvalue. The eigenvectors form an orthonormal basis set and are called the ‘principal components’ of the data set. When they are ordered by decreasing eigenvalue λ , the first principal component will have the largest possible variance, the second the second largest variance, and so on. In our work, we use the singular value decomposition of the covariance matrix to get the eigenvalues and vectors. The vectors \mathbf{c}_i are the scaling coefficients for the principal components.

The PCA technique has several known weaknesses. The first is that its simplest implementation requires a completely filled covariance matrix — in other words there can be no missing data in \mathbf{X} . This is a problem for us since not all modes are identified in each different observation epoch. There are generalizations of the technique which allow for large quantities of missing data. In our case, however, the modes in which we are interested tend to be identified in most of the mode sets, so we can simply interpolate the missing modes from the existing frequency measurements without any significant effect on the results. We do not, therefore, use a more specialized technique.

A second problem with PCA is its sensitivity to outliers. One often-quoted example shows a PCA decomposition where the correlation coefficient between the first two components with one outlier removed is 0.99 (e.g., Huber 1981). There are available routines for making PCA more robust, but in our case, because the dimensionality of the problem is relatively small, we can instead empirically test the sensitivity of the data set to outliers. Monte Carlo tests show that our data set is not prone to errors in the PCA due to outliers.

Principal Component Analysis has been used in a wide variety of astronomical contexts (see references in F. Murtagh & A. Heck 1987, Chapter2). In solar physics, PCA has been used for, among other things, the inversion of Stokes profiles (e.g.,

Eydenberg et al. 2005; Ramírez Vélez et al. 2006), in detecting structures in coronal activity (e.g., Cadavid et al. 2008), and in helioseismic rotation inversions (e.g., Eff-Darwich et al. 2004).

Appendix B

Table B.1.: The sample of active regions used in this work

| NOAA number | Carrington rotation | latitude | longitude | comparison longitude | Δ MAI |
|----------------|------------------------|----------|-----------|-------------------------|--------------|
| 7967 | 1910 | 35N | 331 | 305 | 0.38 |
| 7968 | 1910 | 2N | 294 | 269 | 5.28 |
| 7971 | 1910 | 7S | 257 | 302 | 8.19 |
| 7972 | 1910 | 27N | 104 | 59 | 9.04 |
| 7974 | 1910 | 9N | 73 | 83 | 3.16 |
| 7977 | 1911 | 3N | 295 | 276 | 86.42 |
| 7978 | 1911 | 10S | 253 | 303 | 59.10 |
| 8038 | 1922 | 20N | 144 | 169 | 5.55 |
| 8046 | 1923 | 26S | 274 | 209 | 2.38 |
| 8047 | 1923 | 26N | 208 | 258 | 45.99 |
| 8048 | 1923 | 28S | 187 | 167 | 45.44 |
| 8049 | 1923 | 26S | 225 | 240 | 7.51 |
| 8050 | 1923 | 28N | 69 | 114 | 10.96 |
| 8051 | 1923 | 21N | 132 | 107 | 3.86 |
| 8052 | 1923 | 17N | 28 | 53 | 43.16 |
| 8053 | 1924 | 26S | 317 | 342 | 9.48 |
| 8188 | 1934 | 29N | 198 | 158 | 19.78 |
| 8189 | 1934 | 26S | 258 | 229 | 51.30 |
| 8190 | 1934 | 20S | 141 | 176 | 78.71 |
| 8191 | 1934 | 20S | 118 | 188 | 4.79 |
| 8509 | 1948 | 12N | 267 | 227 | 14.86 |
| 8510 | 1948 | 34S | 269 | 234 | 33.61 |
| 8511 | 1948 | 16S | 261 | 241 | 42.69 |
| 8512 | 1948 | 26S | 249 | 279 | 28.78 |

Continued on next page

Table B.1 – continued from previous page

| NOAA number | Carrington rotation | latitude | longitude | comparison longitude | Δ MAI |
|----------------|------------------------|----------|-----------|-------------------------|--------------|
| 8513 | 1948 | 17S | 233 | 183 | 49.18 |
| 8514 | 1948 | 32S | 234 | 189 | 43.19 |
| 8515 | 1948 | 16S | 210 | 280 | 6.30 |
| 8516 | 1948 | 19S | 151 | 166 | 15.29 |
| 8517 | 1948 | 22N | 221 | 176 | 16.11 |
| 8518 | 1948 | 14S | 107 | 162 | 85.22 |
| 8520 | 1948 | 19N | 137 | 82 | 7.98 |
| 8521 | 1948 | 33N | 162 | 102 | 0.92 |
| 8522 | 1948 | 16N | 36 | 16 | 72.44 |
| 8523 | 1948 | 31N | 38 | 60 | 32.84 |
| 8524 | 1948 | 21N | 36 | 16 | 47.19 |
| 8528 | 1949 | 14S | 284 | 264 | 13.06 |
| 8529 | 1949 | 13S | 327 | 347 | 18.77 |
| 8530 | 1949 | 15N | 267 | 332 | 10.99 |
| 8531 | 1949 | 19N | 248 | 223 | 38.58 |
| 8532 | 1949 | 40S | 296 | 356 | 3.68 |
| 8533 | 1949 | 3N | 223 | 208 | 64.69 |
| 8534 | 1949 | 17S | 223 | 203 | 61.42 |
| 8535 | 1949 | 21N | 219 | 269 | 62.46 |
| 8536 | 1949 | 23S | 237 | 187 | 40.94 |
| 8539 | 1949 | 13N | 238 | 218 | 91.45 |
| 8540 | 1949 | 28S | 189 | 134 | 14.56 |
| 8541 | 1949 | 21N | 196 | 151 | 65.33 |
| 8542 | 1949 | 19S | 144 | 159 | 41.71 |
| 8543 | 1949 | 6N | 148 | 88 | 7.37 |
| 8544 | 1949 | 20S | 117 | 67 | 97.89 |
| 8545 | 1949 | 36N | 102 | 127 | 60.48 |
| 8547 | 1949 | 22N | 175 | 130 | 15.36 |
| 8548 | 1949 | 20S | 90 | 50 | 77.33 |
| 9017 | 1963 | 13S | 174 | 114 | 198.72 |
| 9021 | 1963 | 3N | 185 | 195 | 11.95 |
| 9027 | 1963 | 22N | 146 | 111 | 17.88 |
| 9045 | 1964 | 15S | 313 | 328 | 9.61 |
| 9046 | 1964 | 19N | 258 | 213 | 60.70 |
| 9047 | 1964 | 28S | 285 | 320 | 20.19 |
| 9048 | 1964 | 7N | 331 | 356 | 3.57 |
| 9049 | 1964 | 36S | 247 | 207 | 28.97 |
| 9050 | 1964 | 10S | 298 | 323 | 3.88 |
| 9051 | 1964 | 15N | 220 | 270 | 50.08 |
| 9052 | 1964 | 27S | 297 | 282 | 27.25 |

Continued on next page

Table B.1 – continued from previous page

| NOAA number | Carrington rotation | latitude | longitude | comparison longitude | Δ MAI |
|----------------|------------------------|----------|-----------|-------------------------|--------------|
| 9053 | 1964 | 4N | 229 | 239 | 0.72 |
| 9054 | 1964 | 12N | 195 | 170 | 108.33 |
| 9055 | 1964 | 20N | 178 | 228 | 34.79 |
| 9056 | 1964 | 13S | 181 | 161 | 2.90 |
| 9057 | 1964 | 14N | 163 | 98 | 7.94 |
| 9058 | 1964 | 13S | 238 | 223 | 12.54 |
| 9059 | 1964 | 15N | 188 | 238 | 33.84 |
| 9060 | 1964 | 33S | 148 | 203 | 7.61 |
| 9061 | 1964 | 13S | 138 | 178 | 63.49 |
| 9062 | 1964 | 16S | 117 | 77 | 150.33 |
| 9065 | 1964 | 22N | 70 | 80 | 11.12 |
| 9066 | 1964 | 12N | 60 | 120 | 68.68 |
| 9067 | 1964 | 19S | 69 | 49 | 123.63 |
| 9071 | 1964 | 22N | 91 | 41 | 6.51 |
| 9131 | 1966 | 14N | 191 | 156 | 71.49 |
| 9132 | 1966 | 20N | 201 | 171 | 18.05 |
| 9139 | 1966 | 9S | 149 | 114 | 66.98 |
| 9381 | 1974 | 17S | 323 | 268 | 33.65 |
| 9384 | 1974 | 13N | 330 | 10 | 32.56 |
| 9385 | 1974 | 11S | 255 | 240 | 37.91 |
| 9386 | 1974 | 4N | 263 | 203 | 22.69 |
| 9387 | 1974 | 8N | 218 | 193 | 24.52 |
| 9390 | 1974 | 14N | 186 | 146 | 135.68 |
| 9391 | 1974 | 4S | 264 | 254 | 23.97 |
| 9392 | 1974 | 18N | 265 | 230 | 1.86 |
| 9393 | 1974 | 17N | 157 | 207 | 135.67 |
| 9394 | 1974 | 8N | 156 | 146 | 140.64 |
| 9395 | 1974 | 12S | 153 | 128 | 88.27 |
| 9396 | 1974 | 6S | 213 | 153 | 17.49 |
| 9397 | 1974 | 8S | 132 | 192 | 93.15 |
| 9398 | 1974 | 20N | 208 | 163 | 42.62 |
| 9399 | 1974 | 29S | 204 | 259 | 4.39 |
| 9400 | 1974 | 10N | 166 | 221 | 34.92 |
| 9401 | 1974 | 22N | 133 | 158 | 160.33 |
| 9402 | 1974 | 17N | 180 | 230 | 49.93 |
| 9403 | 1974 | 14S | 118 | 83 | 135.51 |
| 9404 | 1974 | 4S | 102 | 152 | 53.78 |
| 9405 | 1974 | 13S | 171 | 186 | 20.94 |
| 9406 | 1974 | 26N | 86 | 46 | 15.27 |
| 9407 | 1974 | 11N | 85 | 145 | 5.84 |

Continued on next page

Table B.1 – continued from previous page

| NOAA number | Carrington rotation | latitude | longitude | comparison longitude | Δ MAI |
|----------------|------------------------|----------|-----------|-------------------------|--------------|
| 9408 | 1974 | 9S | 116 | 81 | 124.69 |
| 9410 | 1974 | 36S | 81 | 56 | 35.43 |
| 9411 | 1974 | 7N | 86 | 51 | 66.86 |
| 9413 | 1974 | 10N | 115 | 100 | 28.30 |
| 9416 | 1974 | 17N | 90 | 80 | 27.21 |
| 9419 | 1974 | 8N | 76 | 46 | 66.82 |
| 9426 | 1975 | 8S | 287 | 302 | 19.83 |
| 9427 | 1975 | 7S | 338 | 3 | 75.58 |
| 9429 | 1975 | 8N | 234 | 214 | 81.68 |
| 9431 | 1975 | 10S | 197 | 162 | 58.69 |
| 9432 | 1975 | 8N | 214 | 229 | 78.59 |
| 9433 | 1975 | 17N | 157 | 202 | 165.34 |
| 9434 | 1975 | 18N | 236 | 271 | 5.55 |
| 9435 | 1975 | 20S | 193 | 158 | 108.39 |
| 9436 | 1975 | 10S | 126 | 171 | 26.85 |
| 9437 | 1975 | 9N | 120 | 140 | 22.70 |
| 9438 | 1975 | 12S | 147 | 112 | 79.30 |
| 9440 | 1975 | 7N | 105 | 80 | 78.76 |
| 9441 | 1975 | 6N | 84 | 124 | 77.88 |
| 9442 | 1975 | 27N | 71 | 26 | 41.03 |
| 9444 | 1975 | 10S | 37 | 2 | 40.42 |
| 9445 | 1975 | 24N | 31 | 51 | 87.93 |
| 9446 | 1975 | 5S | 111 | 166 | 12.89 |
| 9447 | 1975 | 11N | 53 | 23 | 32.08 |
| 9450 | 1975 | 2S | 37 | 22 | 5.71 |
| 9454 | 1976 | 13N | 231 | 256 | 115.26 |
| 9460 | 1976 | 24S | 193 | 243 | 4.28 |
| 9461 | 1976 | 20N | 161 | 216 | 102.40 |
| 9777 | 1985 | 6S | 270 | 220 | 23.92 |
| 9778 | 1985 | 15S | 262 | 222 | 99.38 |
| 9779 | 1985 | 28N | 266 | 246 | 69.40 |
| 9781 | 1985 | 4S | 230 | 175 | 38.83 |
| 9782 | 1985 | 7N | 222 | 272 | 150.23 |
| 9784 | 1985 | 29S | 209 | 189 | 14.02 |
| 9786 | 1985 | 25S | 221 | 211 | 26.70 |
| 9787 | 1985 | 7S | 130 | 185 | 172.83 |
| 9788 | 1985 | 17N | 151 | 141 | 64.72 |
| 9789 | 1985 | 19N | 191 | 251 | 27.67 |
| 9790 | 1985 | 27N | 164 | 134 | 15.00 |
| 9791 | 1985 | 2S | 196 | 136 | 34.66 |

Continued on next page

Table B.1 – continued from previous page

| NOAA number | Carrington rotation | latitude | longitude | comparison longitude | Δ MAI |
|----------------|------------------------|----------|-----------|-------------------------|--------------|
| 9792 | 1985 | 0 | 151 | 121 | 18.59 |
| 9793 | 1985 | 14S | 146 | 186 | 70.50 |
| 9794 | 1985 | 12N | 113 | 158 | 23.90 |
| 9796 | 1985 | 9N | 118 | 168 | 27.54 |
| 9797 | 1985 | 17S | 107 | 152 | 10.10 |
| 9798 | 1985 | 2S | 95 | 80 | 25.77 |
| 9799 | 1985 | 23S | 80 | 40 | 41.10 |
| 9829 | 1986 | 7S | 129 | 84 | 73.85 |
| 9830 | 1986 | 19S | 136 | 161 | 212.03 |
| 9832 | 1986 | 7S | 130 | 90 | 44.80 |
| 9833 | 1986 | 11N | 157 | 127 | 72.61 |
| 9834 | 1986 | 3N | 88 | 73 | 19.76 |
| 9836 | 1986 | 2S | 154 | 94 | 32.81 |
| 9837 | 1986 | 9N | 56 | 61 | 29.21 |
| 9838 | 1986 | 5N | 133 | 73 | 9.00 |
| 9839 | 1986 | 17S | 108 | 113 | 14.42 |
| 9842 | 1986 | 18S | 97 | 132 | 95.44 |
| 9844 | 1986 | 22N | 56 | 86 | 85.83 |
| 9854 | 1987 | 10N | 353 | 23 | 9.59 |
| 9874 | 1987 | 17N | 109 | 94 | 28.33 |
| 9875 | 1987 | 20S | 72 | 62 | 26.17 |
| 9881 | 1987 | 3S | 100 | 90 | 21.99 |
| 9889 | 1988 | 16S | 287 | 332 | 152.05 |
| 9891 | 1988 | 8S | 316 | 331 | 34.83 |
| 9892 | 1988 | 5N | 246 | 301 | 48.90 |
| 9893 | 1988 | 18N | 215 | 240 | 150.37 |
| 9894 | 1988 | 15N | 277 | 307 | 34.74 |
| 9895 | 1988 | 6N | 205 | 145 | 39.81 |
| 9896 | 1988 | 10S | 194 | 244 | 43.54 |
| 9897 | 1988 | 1S | 259 | 279 | 18.44 |
| 9898 | 1988 | 18S | 190 | 215 | 29.60 |
| 9899 | 1988 | 18N | 181 | 236 | 85.42 |
| 9900 | 1988 | 28S | 232 | 192 | 60.54 |
| 9901 | 1988 | 20N | 204 | 264 | 173.94 |
| 9902 | 1988 | 12N | 162 | 192 | 83.67 |
| 9903 | 1988 | 17N | 151 | 176 | 47.03 |
| 9904 | 1988 | 15S | 221 | 191 | 39.55 |
| 9905 | 1988 | 15S | 202 | 237 | 19.60 |
| 9906 | 1988 | 14S | 149 | 209 | 217.77 |
| 9907 | 1988 | 3S | 116 | 171 | 119.72 |

Continued on next page

Table B.1 – continued from previous page

| NOAA number | Carrington rotation | latitude | longitude | comparison longitude | Δ MAI |
|----------------|------------------------|----------|-----------|-------------------------|--------------|
| 9909 | 1988 | 8N | 80 | 135 | 69.78 |
| 9910 | 1988 | 20S | 89 | 109 | 51.08 |
| 9911 | 1988 | 13S | 73 | 58 | 28.87 |
| 9912 | 1988 | 10N | 68 | 108 | 114.25 |
| 9913 | 1988 | 15S | 61 | 6 | 70.08 |
| 9914 | 1988 | 4N | 14 | 359 | 107.02 |
| 9915 | 1988 | 11N | 3 | 33 | 116.19 |
| 9918 | 1988 | 6N | 44 | 59 | 1.81 |
| 9920 | 1988 | 22S | 31 | 51 | 37.58 |
| 9924 | 1988 | 15S | 27 | 327 | 21.72 |
| 9925 | 1988 | 14S | 41 | 81 | 15.82 |
| 9926 | 1989 | 13N | 313 | 293 | 39.00 |
| 9927 | 1989 | 26S | 237 | 177 | 20.31 |
| 9928 | 1989 | 18N | 236 | 286 | 57.57 |
| 9929 | 1989 | 22N | 284 | 244 | 35.21 |
| 9930 | 1989 | 12N | 302 | 272 | 57.88 |
| 9931 | 1989 | 15N | 268 | 283 | 12.54 |
| 9932 | 1989 | 27S | 224 | 164 | 7.88 |
| 9933 | 1989 | 17N | 219 | 184 | 46.73 |
| 9934 | 1989 | 16S | 210 | 170 | 136.85 |
| 9935 | 1989 | 18S | 240 | 230 | 24.36 |
| 9936 | 1989 | 16S | 232 | 267 | 37.81 |
| 9937 | 1989 | 8S | 189 | 219 | 91.67 |
| 9938 | 1989 | 5S | 186 | 216 | 25.44 |
| 9939 | 1989 | 18N | 178 | 173 | 5.90 |
| 9940 | 1989 | 16N | 177 | 167 | 39.38 |
| 9941 | 1989 | 22S | 222 | 192 | 63.64 |
| 9942 | 1989 | 21N | 195 | 135 | 69.67 |
| 9943 | 1989 | 10S | 169 | 179 | 19.11 |
| 9944 | 1989 | 8N | 170 | 155 | 11.31 |
| 9945 | 1989 | 3S | 139 | 199 | 113.74 |
| 9946 | 1989 | 6S | 128 | 178 | 90.79 |
| 9948 | 1989 | 21S | 88 | 108 | 122.71 |
| 9949 | 1989 | 16S | 160 | 125 | 37.71 |
| 9950 | 1989 | 5S | 109 | 64 | 67.19 |
| 9952 | 1989 | 15S | 148 | 133 | 30.83 |
| 9956 | 1989 | 8S | 89 | 104 | 50.93 |
| 9970 | 1990 | 5N | 260 | 235 | 78.39 |
| 9971 | 1990 | 21N | 287 | 252 | 36.48 |
| 9976 | 1990 | 10S | 260 | 295 | 10.49 |

Continued on next page

Table B.1 – continued from previous page

| NOAA number | Carrington rotation | latitude | longitude | comparison longitude | Δ MAI |
|----------------|------------------------|----------|-----------|-------------------------|--------------|
| 10276 | 1999 | 13S | 161 | 216 | 89.86 |
| 10277 | 1999 | 18S | 136 | 171 | 11.08 |
| 10279 | 1999 | 12S | 190 | 195 | 1.64 |
| 10284 | 1999 | 12N | 169 | 189 | 1.97 |
| 10286 | 1999 | 12S | 143 | 213 | 9.49 |
| 10487 | 2009 | 12N | 260 | 195 | 10.76 |
| 10488 | 2009 | 8N | 290 | 315 | 269.89 |
| 10489 | 2009 | 12S | 302 | 283 | 51.71 |
| 10490 | 2009 | 11S | 260 | 290 | 88.92 |
| 10491 | 2009 | 6S | 293 | 278 | 46.20 |
| 10493 | 2009 | 9N | 278 | 256 | 72.43 |
| 10494 | 2009 | 23S | 263 | 313 | 9.27 |
| 10498 | 2009 | 3S | 173 | 163 | 6.89 |
| 10499 | 2009 | 16S | 173 | 153 | 49.40 |
| 10641 | 2018 | 14N | 176 | 196 | 18.17 |
| 10643 | 2018 | 8S | 177 | 137 | 6.95 |
| 10645 | 2018 | 11N | 160 | 170 | 7.07 |
| 10654 | 2019 | 7N | 266 | 231 | 34.60 |
| 10655 | 2019 | 9S | 181 | 121 | 75.22 |
| 10656 | 2019 | 14S | 82 | 142 | 312.38 |
| 10657 | 2019 | 10N | 74 | 89 | 24.61 |
| 10791 | 2032 | 13N | 159 | 169 | 0.13 |
| 10792 | 2032 | 11N | 56 | 41 | 149.10 |
| 10793 | 2032 | 13N | 115 | 60 | 30.59 |
| 10796 | 2032 | 7S | 46 | 71 | 5.28 |
| 10800 | 2033 | 16N | 157 | 137 | 123.87 |
| 10870 | 2042 | 7S | 337 | 327 | 13.40 |
| 10871 | 2042 | 6S | 309 | 334 | 58.13 |
| 10872 | 2042 | 7S | 276 | 217 | 6.50 |
| 10873 | 2042 | 3S | 299 | 349 | 27.73 |
| 10874 | 2042 | 0 | 239 | 259 | 30.53 |
| 10875 | 2042 | 10S | 114 | 79 | 165.70 |
| 10876 | 2042 | 15S | 82 | 112 | 95.15 |
| 10877 | 2042 | 5S | 81 | 141 | 3.16 |
| 10978 | 2064 | 8S | 223 | 198 | 156.17 |
| 10980 | 2065 | 7S | 237 | 267 | 47.48 |
| 10981 | 2065 | 27N | 245 | 290 | 8.85 |
| 10987 | 2068 | 7S | 260 | 305 | 76.79 |
| 10988 | 2068 | 7S | 237 | 257 | 1.99 |
| 10989 | 2068 | 11S | 205 | 195 | 40.43 |

REFERENCES

- Aerts, C., Christensen-Dalsgaard, J., & Kurtz, D. W., **2010**, *Asteroseismology*, Dordrecht: Springer
- Ahmad, Q. R., Allen, R. C., Andersen, T. C., et al., **2001**, “Measurement of the Rate of $\nu_e + d \rightarrow p + p + e^-$ Interactions Produced by 8B Solar Neutrinos at the Sudbury Neutrino Observatory,” *Physical Review Letters*, 87, 7, 071,301
- Anguera Gubau, M., Palle, P. L., Perez Hernandez, F., et al., **1992**, “The low L solar p-mode spectrum at maximum and minimum solar activity,” *A&A*, 255, 363–372
- Antia, H. M., **1995**, “Effects of surface layers on helioseismic inversion,” *MNRAS*, 274, 499–503
- Antia, H. M., **1996**, “Nonasymptotic helioseismic inversion: iterated seismic solar model.” *A&A*, 307, 609–623
- Antia, H. M., **2002**, *Numerical Methods for Scientists and Engineers*, Basel: Birkhäuser, 2nd edition
- Antia, H. M. & Basu, S., **1994**, “Nonasymptotic helioseismic inversion for solar structure.” *A&AS*, 107, 421–444
- Antia, H. M. & Basu, S., **2000**, “Temporal Variations of the Rotation Rate in the Solar Interior,” *ApJ*, 541, 442–448
- Antia, H. M. & Basu, S., **2001**, “Temporal Variations of the Solar Rotation Rate at High Latitudes,” *ApJ*, 559, L67–L70

- Antia, H. M., Basu, S., & Chitre, S. M., **2008**, “Solar Rotation Rate and Its Gradients During Cycle 23,” *ApJ*, 681, 680–692
- Antia, H. M., Basu, S., Hill, F., et al., **2001a**, “Solar-cycle variation of the sound-speed asphericity from GONG and MDI data 1995-2000,” *MNRAS*, 327, 1029–1040
- Antia, H. M., Basu, S., Hill, F., et al., **2001b**, “Studying asphericity in the solar sound speed from MDI and GONG data,” in A. Wilson & P. L. Pallé, ed., “SOHO 10/GONG 2000 Workshop: Helio- and Asteroseismology at the Dawn of the Millennium,” volume 464 of *ESA Special Publication*, 45–50
- Antia, H. M., Chitre, S. M., & Thompson, M. J., **2000**, “The Sun’s acoustic asphericity and magnetic fields in the solar convection zone,” *A&A*, 360, 335–344
- Bachmann, K. T. & Brown, T. M., **1993**, “P-mode frequency variation in relation to global solar activity,” *ApJ*, 411, L45–L48
- Backus, G. & Gilbert, F., **1968**, “The Resolving Power of Gross Earth Data,” *Geophysical Journal International*, 16, 169–205
- Backus, G. E. & Gilbert, J. F., **1967**, “Numerical Applications of a Formalism for Geophysical Inverse Problems,” *Geophysical Journal International*, 13, 247–276
- Bahcall, J. N., **1989**, *Neutrino astrophysics*, Cambridge and New York: Cambridge University Press
- Bahcall, J. N., Basu, S., & Pinsonneault, M. H., **1998**, “How uncertain are solar neutrino predictions?” *Physics Letters B*, 433, 1–8

- Bahcall, J. N., Pinsonneault, M. H., Basu, S., et al., **1997**, “Are Standard Solar Models Reliable?” *Physical Review Letters*, 78, 171–174
- Baldner, C. S. & Basu, S., **2008**, “Solar Cycle Related Changes at the Base of the Convection Zone,” *ApJ*, 686, 1349–1361
- Baldner, C. S., Larson, T. P., & Basu, S., **2009**, “Solar-Cycle Related Changes at the Base of the Convection Zone,” in M. Dikpati, T. Arentoft, I. González Hernández, C. Lindsey, & F. Hill, ed., “Solar-Stellar Dynamos as Revealed by Helio- and Asteroseismology: GONG 2008/SOHO 21,” volume 416 of *Astronomical Society of the Pacific Conference Series*, 477
- Balmforth, N. J., **1992**, “Solar pulsational stability. I - Pulsation-mode thermodynamics.” *MNRAS*, 255, 603–649
- Balmforth, N. J., Gough, D. O., & Merryfield, W. J., **1996**, “Structural changes to the Sun through the solar cycle,” *MNRAS*, 278, 437–448
- Basu, S., **1997**, “Seismology of the base of the solar convection zone,” *MNRAS*, 288, 572–584
- Basu, S., **2002**, “What does helioseismology tell us about solar cycle related structural changes in the Sun?” in A. Wilson, ed., “From Solar Min to Max: Half a Solar Cycle with SOHO,” volume 508 of *ESA Special Publication*, 7–14
- Basu, S. & Antia, H. M., **2000**, “Possible solar cycle variations in the convection zone,” *Sol. Phys.*, 192, 449–458
- Basu, S. & Antia, H. M., **2001**, “A study of temporal variations of the tachocline,” in A. Wilson & P. L. Pallé, ed., “SOHO 10/GONG 2000 Workshop: Helio-

and Asteroseismology at the Dawn of the Millennium,” volume 464 of *ESA Special Publication*, 297–300

Basu, S. & Antia, H. M., **2006**, “Temporal variations of solar rotation during solar cycle 23,” in “Proceedings of SOHO 18/GONG 2006/HELAS I, Beyond the spherical Sun,” volume 624 of *ESA Special Publication*, 128

Basu, S., Antia, H. M., & Bogart, R. S., **2004**, “Ring-Diagram Analysis of the Structure of Solar Active Regions,” *ApJ*, 610, 1157–1168

Basu, S., Antia, H. M., & Bogart, R. S., **2007**, “Structure of the Near-Surface Layers of the Sun: Asphericity and Time Variation,” *ApJ*, 654, 1146–1165

Basu, S., Antia, H. M., & Narasimha, D., **1994**, “Helioseismic measurement of the extent of overshoot below the solar convection zone,” *MNRAS*, 267, 209

Basu, S., Antia, H. M., & Tripathy, S. C., **1999**, “Ring Diagram Analysis of Near-Surface Flows in the Sun,” *ApJ*, 512, 458–470

Basu, S. & Mandel, A., **2004**, “Does Solar Structure Vary with Solar Magnetic Activity?” *ApJ*, 617, L155–L158

Basu, S. & Thompson, M. J., **1996**, “On constructing seismic models of the Sun.” *A&A*, 305, 631

Bogart, R. S., Basu, S., Rabello-Soares, M. C., et al., **2008**, “Probing the Subsurface Structures of Active Regions with Ring-Diagram Analysis,” *Sol. Phys.*, 251, 439–451

Brandenburg, A., **2005**, “The Case for a Distributed Solar Dynamo Shaped by Near-Surface Shear,” *ApJ*, 625, 539–547

- Brandenburg, A. & Subramanian, K., **2005**, “Astrophysical magnetic fields and nonlinear dynamo theory,” *Phys. Rep.*, 417, 1–209
- Braun, D. C., Duvall, T. L., Jr., & Labonte, B. J., **1987**, “Acoustic absorption by sunspots,” *ApJ*, 319, L27–L31
- Braun, D. C., Duvall, T. L., Jr., Labonte, B. J., et al., **1992**, “Scattering of p-modes by a sunspot,” *ApJ*, 391, L113–L116
- Brodsky, M. & Vorontsov, S. V., **1993**, “Asymptotic theory of intermediate- and high-degree solar acoustic oscillations,” *ApJ*, 409, 455–464
- Brown, B. P., Browning, M. K., Brun, A. S., et al., **2007**, “Strong Dynamo Action in Rapidly Rotating Suns,” in R. J. Stancliffe, G. Houdek, R. G. Martin, & C. A. Tout, ed., “Unsolved Problems in Stellar Physics: A Conference in Honor of Douglas Gough,” volume 948 of *American Institute of Physics Conference Series*, 271–278
- Brown, B. P., Browning, M. K., Brun, A. S., et al., **2010**, “Persistent Magnetic Wreaths in a Rapidly Rotating Sun,” *ApJ*, 711, 424–438
- Brown, T. M., **1985**, “Solar rotation as a function of depth and latitude,” *Nature*, 317, 591–594
- Brown, T. M., Christensen-Dalsgaard, J., Dziembowski, W. A., et al., **1989**, “Inferring the sun’s internal angular velocity from observed p-mode frequency splittings,” *ApJ*, 343, 526–546
- Cadavid, A. C., Lawrence, J. K., & Ruzmaikin, A., **2008**, “Principal Components and Independent Component Analysis of Solar and Space Data,” *Sol. Phys.*, 248, 247–261

- Cally, P. S., **1995**, “Effects of Weak-to-Moderate Vertical Magnetic Fields on Solar f- and p-Modes,” *ApJ*, 451, 372
- Cally, P. S. & Bogdan, T. J., **1997**, “Simulation of f- and p-Mode Interactions with a Stratified Magnetic Field Concentration,” *ApJ*, 486, L67+
- Cally, P. S., Crouch, A. D., & Braun, D. C., **2003**, “Probing sunspot magnetic fields with p-mode absorption and phase shift data,” *MNRAS*, 346, 381–389
- Chandrasekhar, S., **1964**, “A General Variational Principle Governing the Radial and the Non-Radial Oscillations of Gaseous Masses.” *ApJ*, 139, 664
- Chaplin, W. J., **2006**, *Music of the Sun: The Story of Helioseismology*, Oxford: Oneworld Publications
- Chaplin, W. J., Elsworth, Y., Isaak, G. R., et al., **2001**, “Probing the solar cycle: a comparative and complementary analysis of GONG BiSON and VIRGO/LOI eigenfrequency shifts,” in A. Wilson & P. L. Pallé, ed., “SOHO 10/GONG 2000 Workshop: Helio- and Asteroseismology at the Dawn of the Millennium,” volume 464 of *ESA Special Publication*, 83–86
- Chaplin, W. J., Elsworth, Y., Miller, B. A., et al., **2007**, “Solar p-Mode Frequencies over Three Solar Cycles,” *ApJ*, 659, 1749–1760
- Charbonneau, P., **2010**, “Dynamo Models of the Solar Cycle,” *Living Reviews in Solar Physics*, 7, 3
- Charbonneau, P. & MacGregor, K., **1996**, “On the generation of equipartition-strength magnetic fields by turbulent hydromagnetic dynamos,” *Astrophys. J. Lett.*, 473, L59–L62

- Chou, D.-Y. & Serebryanskiy, A., **2002**, “Searching for the Signature of the Magnetic Fields at the Base of the Solar Convection Zone with Solar Cycle Variations of p-Mode Travel Time,” *ApJ*, 578, L157–L160
- Chou, D.-Y. & Serebryanskiy, A., **2005**, “In Search of the Solar Cycle Variations of p-Mode Frequencies Generated by Perturbations in the Solar Interior,” *ApJ*, 624, 420–427
- Chou, D.-Y., Serebryanskiy, A., & Sun, M.-T., **2003**, “Probing Solar Subsurface Magnetic Fields,” *Space Sci. Rev.*, 107, 35–42
- Chou, D.-Y., Sun, M.-T., Huang, T.-Y., et al., **1995**, “Taiwan Oscillation Network,” *Sol. Phys.*, 160, 237–243
- Christensen-Dalsgaard, J., **1981**, “The effect of non-adiabaticity on avoided crossings of non-radial stellar oscillations,” *MNRAS*, 194, 229–250
- Christensen-Dalsgaard, J., **2002**, “Helioseismology,” *Reviews of Modern Physics*, 74, 1073–1129
- Christensen-Dalsgaard, J. & Berthomieu, G., **1991**, *Theory of solar oscillations*, Tucson: University of Arizona Press, 401–478
- Christensen-Dalsgaard, J., Duvall, T. L., Jr., Gough, D. O., et al., **1985**, “Speed of sound in the solar interior,” *Nature*, 315, 378–382
- Christensen-Dalsgaard, J. & Gough, D. O., **1976**, “Towards a heliological inverse problem,” *Nature*, 259, 89–92
- Christensen-Dalsgaard, J. & Gough, D. O., **1982**, “On the interpretation of five-minute oscillations in solar spectrum line shifts,” *MNRAS*, 198, 141–171

- Christensen-Dalsgaard, J., Gough, D. O., & Thompson, M. J., **1991**, “The depth of the solar convection zone,” *ApJ*, 378, 413–437
- Christensen-Dalsgaard, J., Proffitt, C. R., & Thompson, M. J., **1993**, “Effects of diffusion on solar models and their oscillation frequencies,” *ApJ*, 403, L75–L78
- Christensen-Dalsgaard, J. & Schou, J., **1988**, “Differential rotation in the solar interior,” in E. J. Rolfe, ed., “Seismology of the Sun and Sun-Like Stars,” volume 286 of *ESA Special Publication*, 149–153
- Clark, D. H. & Stephenson, F. R., **1978**, “An Interpretation of the Pre-Telescopic Sunspot Records from the Orient,” *QJRAS*, 19, 387
- Claverie, A., Isaak, G. R., McLeod, C. P., et al., **1979**, “Solar structure from global studies of the 5-minute oscillation,” *Nature*, 282, 591–594
- Claverie, A., Isaak, G. R., McLeod, C. P., et al., **1984**, “Continuous observation of solar oscillations from two suitably spaced ground stations,” *Mem. Soc. Astron. Italiana*, 55, 63–66
- Cowling, T. G., **1933**, “The magnetic field of sunspots,” *MNRAS*, 94, 39–48
- Crouch, A. D. & Cally, P. S., **2003**, “Mode Conversion of Solar p Modes in non-Vertical Magnetic Fields - i. two-Dimensional Model,” *Sol. Phys.*, 214, 201–226
- Crouch, A. D. & Cally, P. S., **2005**, “Mode Conversion of Solar p-Modes in Non-Vertical Magnetic Fields,” *Sol. Phys.*, 227, 1–26
- Deubner, F.-L., **1975**, “Observations of low wavenumber nonradial eigenmodes of the sun,” *A&A*, 44, 371–375

- Dikpati, M., **2006**, “The importance of the solar tachocline,” *Advances in Space Research*, 38, 839–844
- D’Silva, S. & Choudhuri, A. R., **1993**, “A theoretical model for tilts of bipolar magnetic regions,” *A&A*, 272, 621
- Durney, B. R., Hill, F., & Goode, P. R., **1988**, “On the Expansion of the Rotational Eigenfrequencies in Legendre Polynomials,” *ApJ*, 326, 486
- Duvall, T. L., Jr., Dziembowski, W. A., Goode, P. R., et al., **1984**, “Internal rotation of the sun,” *Nature*, 310, 22–25
- Duvall, T. L., Jr. & Harvey, J. W., **1983**, “Observations of solar oscillations of low and intermediate degree,” *Nature*, 302, 24–27
- Duvall, T. L., Jr. & Harvey, J. W., **1984**, “Rotational frequency splitting of solar oscillations,” *Nature*, 310, 19–22
- Duvall, T. L., Jr., Harvey, J. W., & Pomerantz, M. A., **1986**, “Latitude and depth variation of solar rotation,” *Nature*, 321, 500
- Duvall, T. L., Jr., Jefferies, S. M., Harvey, J. W., et al., **1993**, “Time-distance helioseismology,” *Nature*, 362, 430–432
- Dziembowski, W. & Goode, P. R., **1984**, “Simple asymptotic estimates of the fine structure in the spectrum of solar oscillations due to rotation and magnetism,” *Mem. Soc. Astron. Italiana*, 55, 185–213
- Dziembowski, W. & Goode, P. R., **1988**, “The Magnetic Field Inside the Sun,” in J. Christensen-Dalsgaard & S. Frandsen, ed., “Advances in Helio- and Asteroseismology,” volume 123 of *IAU Symposium*, 171

- Dziembowski, W. A. & Goode, P. R., **1991**, *The internal rotation and magnetism of the sun from its oscillations*, Tuscon: University of Arizona Press, 501–518
- Dziembowski, W. A. & Goode, P. R., **2005**, “Sources of Oscillation Frequency Increase with Rising Solar Activity,” *ApJ*, 625, 548–555
- Dziembowski, W. A., Goode, P. R., di Mauro, M. P., et al., **1998**, “Solar Cycle Onset Seen in SOHO Michelson Doppler Imager Seismic Data,” *ApJ*, 509, 456–460
- Dziembowski, W. A., Goode, P. R., Kosovichev, A. G., et al., **2000**, “Signatures of the Rise of Cycle 23,” *ApJ*, 537, 1026–1038
- Dziembowski, W. A., Goode, P. R., & Libbrecht, K. G., **1989**, “The radial gradient in the sun’s rotation,” *ApJ*, 337, L53–L57
- Dziembowski, W. A., Goode, P. R., & Schou, J., **2001**, “Does the Sun Shrink with Increasing Magnetic Activity?” *ApJ*, 553, 897–904
- Dziembowski, W. A., Pamyatnykh, A. A., & Sienkiewicz, R., **1990**, “Solar model from helioseismology and the neutrino flux problem,” *MNRAS*, 244, 542–550
- Eff-Darwich, A., Korzennik, S. G., Jiménez-Reyes, S., et al., **2004**, “PCA Inversions for the Rotation of the Solar Radiative Interior,” in D. Danesy, ed., “SOHO 14 Helio- and Asteroseismology: Towards a Golden Future,” volume 559 of *ESA Special Publication*, 420
- Eff-Darwich, A., Korzennik, S. G., Jiménez-Reyes, S. J., et al., **2002**, “An Upper

- Limit on the Temporal Variations of the Solar Interior Stratification,” *ApJ*, 580, 574–578
- Elsworth, Y., Howe, R., Isaak, G. R., et al., **1990**, “Variation of low-order acoustic solar oscillations over the solar cycle,” *Nature*, 345, 322–324
- Elsworth, Y., Howe, R., Isaak, G. R., et al., **1994**, “Solar p-mode frequencies and their dependence on solar activity recent results from the BISON network,” *ApJ*, 434, 801–806
- Evans, J. W. & Michard, R., **1962**, “Observational Study of Macroscopic Inhomogeneities in the Solar Atmosphere. III. Vertical Oscillatory Motions in the Solar Photosphere.” *ApJ*, 136, 493
- Eydenberg, M. S., Balasubramaniam, K. S., & López Ariste, A., **2005**, “PCA-Interpolation Methods for Inversion of Solar Stokes Profiles. I. Inversion of Photospheric Profiles,” *ApJ*, 619, 1167–1188
- F. Murtagh & A. Heck, ed., **1987**, *Multivariate Data Analysis*, volume 131 of *Astrophysics and Space Science Library*
- Felipe, T., Khomenko, E., & Collados, M., **2010**, “Magneto-acoustic Waves in Sunspots: First Results From a New Three-dimensional Nonlinear Magnetohydrodynamic Code,” *ApJ*, 719, 357–377
- Fossat, E., **1995**, “IRIS Status Report,” in R. K. Ulrich, E. J. Rhodes Jr., & W. Dappen, ed., “GONG 1994. Helio- and Astro-Seismology from the Earth and Space,” volume 76 of *Astronomical Society of the Pacific Conference Series*, 387

- Fröhlich, C., Romero, J., Roth, H., et al., **1995**, “VIRGO: Experiment for Helioseismology and Solar Irradiance Monitoring,” *Sol. Phys.*, 162, 101–128
- Gabriel, A. H., Grec, G., Charra, J., et al., **1995**, “Global Oscillations at Low Frequency from the SOHO Mission (GOLF),” *Sol. Phys.*, 162, 61–99
- Gizon, L. & Birch, A. C., **2005**, “Local Helioseismology,” *Living Reviews in Solar Physics*, 2, 6
- Gizon, L., Schunker, H., Baldner, C. S., et al., **2009**, “Helioseismology of Sunspots: A Case Study of NOAA Region 9787,” *Space Sci. Rev.*, 144, 249–273
- Goldreich, P., Murray, N., Willette, G., et al., **1991**, “Implications of solar p-mode frequency shifts,” *ApJ*, 370, 752–762
- Goode, P. R. & Dziembowski, W. A., **1993**, “Seismic Limits on the Sun’s Internal Toroidal Field,” in T. M. Brown, ed., “GONG 1992. Seismic Investigation of the Sun and Stars,” volume 42 of *Astronomical Society of the Pacific Conference Series*, 229
- Gough, D., **1985**, “Inverting helioseismic data,” *Sol. Phys.*, 100, 65–99
- Gough, D. O., **1990**, “Comments on Helioseismic Inference,” in Y. Osaki & H. Shibahashi, ed., “Progress of Seismology of the Sun and Stars,” volume 367 of *Lecture Notes in Physics, Berlin Springer Verlag*, 283
- Gough, D. O., **2002**, “How is solar activity influencing the structure of the Sun,” in A. Wilson, ed., “From Solar Min to Max: Half a Solar Cycle with SOHO,” volume 508 of *ESA Special Publication*, 577–592
- Gough, D. O. & Thompson, M. J., **1990**, “The effect of rotation and a buried magnetic field on stellar oscillations,” *MNRAS*, 242, 25–55

- Grec, G., Fossat, E., & Pomerantz, M., **1980**, “Solar oscillations - Full disk observations from the geographic South Pole,” *Nature*, 288, 541–544
- Guenther, D. B., **1994**, “Nonadiabatic nonradial p-mode frequencies of the standard solar model, with and without helium diffusion,” *ApJ*, 422, 400–411
- Guzik, J. A. & Cox, A. N., **1992**, “On the sensitivity of high-degree p-mode frequencies to the solar convection zone helium abundance,” *ApJ*, 386, 729–733
- Haber, D. A., Hindman, B. W., Toomre, J., et al., **1999**, “Solar Shear Flows Deduced From Helioseismic Dense-Pack Samplings of Ring Diagrams,” in “SOHO-9 Workshop on Helioseismic Diagnostics of Solar Convection and Activity,” volume 9, 62
- Haber, D. A., Hindman, B. W., Toomre, J., et al., **2000**, “Solar shear flows deduced from helioseismic dense-pack samplings of ring diagrams,” *Sol. Phys.*, 192, 335–350
- Hale, G. E., **1908**, “On the Probable Existence of a Magnetic Field in Sun-Spots,” *ApJ*, 28, 315
- Hale, G. E., Ellerman, F., Nicholson, S. B., et al., **1919**, “The Magnetic Polarity of Sun-Spots,” *ApJ*, 49, 153
- Hale, G. E. & Nicholson, S. B., **1925**, “The Law of Sun-Spot Polarity,” *ApJ*, 62, 270
- Harvey, J. W., Branston, D., Henney, C. J., et al., **2007**, “Seething Horizontal Magnetic Fields in the Quiet Solar Photosphere,” *ApJ*, 659, L177–L180

- Harvey, J. W., Hill, F., Hubbard, R. P., et al., **1996**, “The Global Oscillation Network Group (GONG) Project,” *Science*, 272, 1284–1286
- Hill, F., **1988**, “Rings and trumpets - Three-dimensional power spectra of solar oscillations,” *ApJ*, 333, 996–1013
- Hill, F., Stark, P. B., Stebbins, R. T., et al., **1996**, “The Solar Acoustic Spectrum and Eigenmode Parameters,” *Science*, 272, 1292–1295
- Howe, R., **2009**, “Solar Interior Rotation and its Variation,” *Living Reviews in Solar Physics*, 6, 1
- Howe, R., Christensen-Dalsgaard, J., Hill, F., et al., **2000**, “Dynamic Variations at the Base of the Solar Convection Zone,” *Science*, 287, 2456–2460
- Howe, R., Christensen-Dalsgaard, J., Hill, F., et al., **2005**, “Solar Convection-Zone Dynamics, 1995-2004,” *ApJ*, 634, 1405–1415
- Howe, R., Haber, D. A., Hindman, B. W., et al., **2008**, “Helioseismic Frequency Shifts in Active Regions,” in R. Howe, R. W. Komm, K. S. Balasubramanian, & G. J. D. Petrie, ed., “Subsurface and Atmospheric Influences on Solar Activity,” volume 383 of *Astronomical Society of the Pacific Conference Series*, 305
- Howe, R., Komm, R., & Hill, F., **1999a**, “Solar Cycle Changes in GONG P-Mode Frequencies, 1995-1998,” *ApJ*, 524, 1084–1095
- Howe, R., Komm, R., & Hill, F., **1999b**, “Solar Cycle Changes in GONG P-Mode Frequencies, 1995-1998,” *ApJ*, 524, 1084–1095
- Howe, R., Komm, R. W., & Hill, F., **2002**, “Localizing the Solar Cycle Frequency Shifts in Global p-Modes,” *ApJ*, 580, 1172–1187

- Howe, R., Komm, R. W., Hill, F., et al., **2004**, “Activity-related Changes in Local Solar Acoustic Mode Parameters from Michelson Doppler Imager and Global Oscillations Network Group,” *ApJ*, 608, 562–579
- Howe, R., Rempel, M., Christensen-Dalsgaard, J., et al., **2006**, “Solar Convection Zone Dynamics: How Sensitive Are Inversions to Subtle Dynamo Features?” *ApJ*, 649, 1155–1168
- Howe, R., Tripathy, S., González Hernández, I., et al., **2011**, “Ring-diagram parameter comparisons for GONG, MDI and HMI,” *Journal of Physics Conference Series*, 271, 1, 012,015
- Hoyt, D. V. & Schatten, K. H., **1997**, *The role of the sun in climate change*, New York : Oxford University Press
- Huber, P. J., **1981**, *Robust Statistics*, New York, NY: Wiley
- Iben, I., Jr. & Mahaffy, J., **1976**, “On the sun’s acoustical spectrum,” *ApJ*, 209, L39–L43
- Isaak, G. R., **1982**, “Is the Sun an oblique magnetic rotator?” *Nature*, 296, 130–131
- Jain, R., **2007**, “Effects of Horizontal Magnetic Fields on Acoustic Travel Times,” *ApJ*, 656, 610–614
- Jain, R., Hindman, B. W., & Zweibel, E. G., **1996**, “The Influence of Magnetism on p-Mode Surface Amplitudes,” *ApJ*, 464, 476
- Jimenez-Reyes, S. J., Regulo, C., Palte, P. L., et al., **1998**, “Solar activity cycle frequency shifts of low-degree p-modes,” *A&A*, 329, 1119–1124

- Kendall, M., **1980**, *Multivariate Analysis*, New York, NY: Macmillan Publishing Co, 2nd edition
- Korzennik, S. G., Rabello-Soares, M. C., & Schou, J., **2004**, “On the Determination of Michelson Doppler Imager High-Degree Mode Frequencies,” *ApJ*, 602, 481–516
- Kosovichev, A. G., **1988**, “The determination of the angular velocity of the sun’s inner rotation using helioseismological data,” *Pis ma Astronomicheskii Zhurnal*, 14, 344–352
- Kosovichev, A. G., Duvall, T. L. , Jr., & Scherrer, P. H., **2000**, “Time-Distance Inversion Methods and Results - (Invited Review),” *Sol. Phys.*, 192, 159–176
- Kuhn, J. R., **1988**, “Helioseismological splitting measurements and the nonspherical solar temperature structure,” *ApJ*, 331, L131–L134
- Larson, T. P. & Schou, J., **2008**, “Improvements in global mode analysis,” *Journal of Physics Conference Series*, 118, 1, 012,083
- Leibacher, J. W. & Stein, R. F., **1971**, “A New Description of the Solar Five-Minute Oscillation,” *Astrophys. Lett.*, 7, 191–192
- Leighton, R. B., Noyes, R. W., & Simon, G. W., **1962**, “Velocity Fields in the Solar Atmosphere. I. Preliminary Report.” *ApJ*, 135, 474
- Li, L. H., Basu, S., Sofia, S., et al., **2003**, “Global Parameter and Helioseismic Tests of Solar Variability Models,” *ApJ*, 591, 1267–1284
- Libbrecht, K. G., **1989**, “Solar p-mode frequency splittings,” *ApJ*, 336, 1092–1097

- Libbrecht, K. G. & Woodard, M. F., **1990**, “Solar-cycle effects on solar oscillation frequencies,” *Nature*, 345, 779–782
- Lin, C.-H., Basu, S., & Li, L., **2009**, “Interpreting Helioseismic Structure Inversion Results of Solar Active Regions,” *Sol. Phys.*, 257, 37–60
- Lindsey, C. & Braun, D. C., **1990**, “Helioseismic imaging of sunspots at their antipodes,” *Sol. Phys.*, 126, 101–115
- Lites, B., Socas-Navarro, H., Kubo, M., et al., **2007**, “Hinode Observations of Horizontal Quiet Sun Magnetic Flux and the “Hidden Turbulent Magnetic Flux”,” *PASJ*, 59, 571
- Lites, B. W., Kubo, M., Socas-Navarro, H., et al., **2008**, “The Horizontal Magnetic Flux of the Quiet-Sun Internetwork as Observed with the Hinode Spectro-Polarimeter,” *ApJ*, 672, 1237–1253
- Lites, B. W., White, O. R., & Packman, D., **1982**, “Photoelectric observations of propagating sunspot oscillations,” *ApJ*, 253, 386–392
- Lynden-Bell, D. & Ostriker, J. P., **1967**, “On the stability of differentially rotating bodies,” *MNRAS*, 136, 293
- Maunder, E. W., **1904**, “Note on the distribution of sun-spots in heliographic latitude, 1874-1902,” *MNRAS*, 64, 747–761
- Miesch, M. S. & Toomre, J., **2009**, “Turbulence, Magnetism, and Shear in Stellar Interiors,” *Annual Review of Fluid Mechanics*, 41, 317–345
- Moradi, H., Baldner, C., Birch, A. C., et al., **2010**, “Modeling the Subsurface Structure of Sunspots,” *Sol. Phys.*, 267, 1–62

- Moreno-Insertis, F. & Solanki, S. K., **2000**, “Distribution of magnetic flux on the solar surface and low-degree p-modes,” *MNRAS*, 313, 411–422
- Ossendrijver, M., **2003**, “The Solar Dynamo: A Challenge for Theory and Observations (Invited review),” in A. A. Pevtsov & H. Uitenbroek, ed., “Current Theoretical Models and Future High Resolution Solar Observations: Preparing for ATST,” volume 286 of *Astronomical Society of the Pacific Conference Series*, 97
- Parker, E., **1993**, “A solar dynamo surface wave at the interface between convection and nonuniform rotation,” *Astrophys. J.*, 408, 707–719
- Patron, J., Gonzalez Hernandez, I., Chou, D.-Y., et al., **1997**, “Comparison of Two Fitting Methods for Ring Diagram Analysis of Very High L Solar Oscillations,” *ApJ*, 485, 869
- Petrie, G. J. D. & Patrikeeva, I., **2009**, “A Comparative Study of Magnetic Fields in the Solar Photosphere and Chromosphere at Equatorial and Polar Latitudes,” *ApJ*, 699, 871–884
- Pijpers, F. P. & Thompson, M. J., **1992**, “Faster formulations of the optimally localized averages method for helioseismic inversions,” *A&A*, 262, L33–L36
- Pijpers, F. P. & Thompson, M. J., **1994**, “The SOLA method for helioseismic inversion,” *A&A*, 281, 231–240
- Rabello-Soares, M. C., Basu, S., & Christensen-Dalsgaard, J., **1999**, “On the choice of parameters in solar-structure inversion,” *MNRAS*, 309, 35–47
- Rabello-Soares, M. C., Bogart, R. S., & Basu, S., **2008**, “Analysis of the char-

- acteristics of solar oscillation modes in active regions,” *Journal of Physics Conference Series*, 118, 1, 012,084
- Rabello-Soares, M. C. & Korzennik, S. G., **2009**, “Search for Structural Variations of the Near-Surface Layers of the Sun during the Solar Cycle,” in M. Dikpati, T. Arentoft, I. González Hernández, C. Lindsey, & F. Hill, ed., “Solar-Stellar Dynamos as Revealed by Helio- and Asteroseismology: GONG 2008/SOHO 21,” volume 416 of *Astronomical Society of the Pacific Conference Series*, 277
- Rabello-Soares, M. C., Korzennik, S. G., & Schou, J., **2001**, “The determination of MDI high-degree mode frequencies,” in A. Wilson & P. L. Pallé, ed., “SOHO 10/GONG 2000 Workshop: Helio- and Asteroseismology at the Dawn of the Millennium,” volume 464 of *ESA Special Publication*, 129–136
- Rajaguru, S. P., Basu, S., & Antia, H. M., **2001**, “Ring Diagram Analysis of the Characteristics of Solar Oscillation Modes in Active Regions,” *ApJ*, 563, 410–418
- Rámirez Vélez, J. C., Semel, M., Stift, M. J., et al., **2006**, “PCA Technique Applied to the Detection of ZDI Circular Polarization in Solar-Type Stars,” in R. Casini & B. W. Lites, ed., “Astronomical Society of the Pacific Conference Series,” volume 358 of *Astronomical Society of the Pacific Conference Series*, 405
- Regulo, C., Jimenez, A., Pallé, P. L., et al., **1994**, “Variation of the frequencies of very low L p-modes,” *ApJ*, 434, 384–388
- Rhodes, E. J., Jr., Reiter, J., Kosovichev, A. G., et al., **1998**, “Initial SOI/MDI High-Degree Frequencies and Frequency Splittings,” in S. Korzennik, ed.,

- “Structure and Dynamics of the Interior of the Sun and Sun-like Stars,”
volume 418 of *ESA Special Publication*, 73
- Rhodes, E. J., Jr., Ulrich, R. K., & Simon, G. W., **1977**, “Observations of nonradial p-mode oscillations on the sun,” *ApJ*, 218, 901–919
- Ritzwoller, M. H. & Lavelly, E. M., **1991**, “A unified approach to the helioseismic forward and inverse problems of differential rotation,” *ApJ*, 369, 557–566
- Robinson, F. J., Demarque, P., Li, L. H., et al., **2003**, “Three-dimensional convection simulations of the outer layers of the Sun using realistic physics,” *MNRAS*, 340, 923–936
- Rosenthal, C. S. & Julien, K. A., **2000**, “Numerical Modeling of the Absorption and Scattering of Acoustic Radiation by Sunspots,” *ApJ*, 532, 1230–1239
- Roxburgh, I. W. & Vorontsov, S. V., **1994**, “Seismology of the Solar Envelope - the Base of the Convective Zone as Seen in the Phase Shift of Acoustic Waves,” *MNRAS*, 268, 880
- Scherrer, P. H., Bogart, R. S., Bush, R. I., et al., **1995**, “The Solar Oscillations Investigation - Michelson Doppler Imager,” *Sol. Phys.*, 162, 129–188
- Schou, J., **1999**, “Migration of Zonal Flows Detected Using Michelson Doppler Imager F-Mode Frequency Splittings,” *ApJ*, 523, L181–L184
- Schou, J., Antia, H. M., Basu, S., et al., **1998**, “Helioseismic Studies of Differential Rotation in the Solar Envelope by the Solar Oscillations Investigation Using the Michelson Doppler Imager,” *ApJ*, 505, 390–417
- Schou, J. & Bogart, R. S., **1998**, “Flow and Horizontal Displacements from Ring Diagrams,” *ApJ*, 504, L131+

- Schrijver, C. J. & Liu, Y., **2008**, “The Global Solar Magnetic Field Through a Full Sunspot Cycle: Observations and Model Results,” *Sol. Phys.*, 252, 19–31
- Schunker, H., Braun, D. C., Cally, P. S., et al., **2005**, “The Local Helioseismology of Inclined Magnetic Fields and the Showerglass Effect,” *ApJ*, 621, L149–L152
- Schunker, H., Braun, D. C., Lindsey, C., et al., **2008**, “Physical Properties of Wave Motion in Inclined Magnetic Fields within Sunspot Penumbrae,” *Sol. Phys.*, 251, 341–359
- Schwabe, M., **1844**, “Sonnenbeobachtungen im Jahre 1843. Von Herrn Hofrath Schwabe in Dessau,” *Astronomische Nachrichten*, 21, 233
- Scuflaire, R., Gabriel, M., Noels, A., et al., **1975**, “Oscillatory periods in the sun and theoretical models with or without mixing,” *A&A*, 45, 15–18
- Sekii, T., **1997**, “Internal Solar rotation,” in J. Provost & F.-X. Schmider, ed., “Sounding Solar and Stellar Interiors,” volume 181 of *IAU Symposium*, 189
- Serebryanskiy, A. & Chou, D.-Y., **2005**, “Comparison of Solar Cycle Variations of Solar p-Mode Frequencies from GONG and MDI,” *ApJ*, 633, 1187–1190
- Severnyi, A. B., Kotov, V. A., & Tsap, T. T., **1979**, “Solar oscillations and the problem of the internal structure of the sun,” *Soviet Ast.*, 23, 641
- Shelyag, S., Zharkov, S., Fedun, V., et al., **2009**, “Acoustic wave propagation in the solar sub-photosphere with localised magnetic field concentration: effect of magnetic tension,” *A&A*, 501, 735–743
- Spiegel, E. A. & Zahn, J.-P., **1992**, “The solar tachocline,” *A&A*, 265, 106–114

- Tapping, K. F., **1987**, “Recent solar radio astronomy at centimeter wavelengths - The temporal variability of the 10.7-cm flux,” *J. Geophys. Res.*, 92, 829–838
- Thompson, M. J., Toomre, J., Anderson, E. R., et al., **1996**, “Differential Rotation and Dynamics of the Solar Interior,” *Science*, 272, 1300–1305
- Title, A. M., Topka, K. P., Tarbell, T. D., et al., **1992**, “On the differences between plage and quiet sun in the solar photosphere,” *ApJ*, 393, 782–794
- Tomczyk, S., Cacciani, A., & Veitzer, S. A., **1993**, “LOWL - an Instrument to Observe Low-Degree Solar Oscillations,” in T. M. Brown, ed., “GONG 1992. Seismic Investigation of the Sun and Stars,” volume 42 of *Astronomical Society of the Pacific Conference Series*, 469
- Tripathy, S. C., Kumar, B., Jain, K., et al., **2000**, “Observation of Hysteresis Between Solar Activity Indicators and p-mode Frequency Shifts for Solar Cycle 22,” *Journal of Astrophysics and Astronomy*, 21, 357
- Tripathy, S. C., Kumar, B., Jain, K., et al., **2001**, “Analysis of hysteresis effect in p-mode frequency shifts and solar activity indices,” *Sol. Phys.*, 200, 3–10
- Ulrich, R. K., **1970**, “The Five-Minute Oscillations on the Solar Surface,” *ApJ*, 162, 993
- Ulrich, R. K. & Boyden, J. E., **2005**, “The Solar Surface Toroidal Magnetic Field,” *ApJ*, 620, L123–L127
- Verner, G. A., Chaplin, W. J., & Elsworth, Y., **2004**, “Search for solar cycle changes in the signature of rapid variation in BiSON data,” *MNRAS*, 351, 311–316

- Verner, G. A., Chaplin, W. J., & Elsworth, Y., **2006**, “BiSON Data Show Change in Solar Structure with Magnetic Activity,” *ApJ*, 640, L95–L98
- Vorontsov, S. V., Christensen-Dalsgaard, J., Schou, J., et al., **2002**, “Helioseismic Measurement of Solar Torsional Oscillations,” *Science*, 296, 101–103
- Woodard, M. F., Libbrecht, K. G., Kuhn, J. R., et al., **1991**, “Short-term changes in solar oscillation frequencies and solar activity,” *ApJ*, 373, L81–L84
- Woodard, M. F. & Noyes, R. W., **1985**, “Change of solar oscillation eigenfrequencies with the solar cycle,” *Nature*, 318, 449–450
- Zhao, J. & Kosovichev, A. G., **2006**, “Surface Magnetism Effects in Time-Distance Helioseismology,” *ApJ*, 643, 1317–1324
- Zweibel, E. G. & Gough, D., **1995**, “Is There a Seismic Signature of the Sun’s Magnetic Field?” in “Helioseismology,” volume 376 of *ESA Special Publication*, 73